

OPTICAL ANALYSIS OF CROSSED COMPOUND
PARABOLIC CONCENTRATOR FOR HIGH
CONCENTRATOR PHOTOVOLTAIC SYSTEM

LEE PEI SHAN

MASTER OF ENGINEERING SCIENCE

LEE KONG CHIAN FACULTY OF ENGINEERING SCIENCE
UNIVERSITY TUNKU ABDUL RAHMAN

JULY 2021

**OPTICAL ANALYSIS OF CROSSED COMPOUND PARABOLIC
CONCENTRATOR FOR HIGH CONCENTRATOR
PHOTOVOLTAIC SYSTEM**

By

LEE PEI SHAN

A dissertation submitted to the Department of Electrical and Electronics Engineering, Lee Kong Chian Faculty of Engineering Science, University Tunku Abdul Rahman, in partial fulfillment of the requirements for the degree of Master of Engineering Science.

JULY 2021

ABSTRACT

OPTICAL ANALYSIS OF CROSSED COMPOUND PARABOLIC CONCENTRATOR FOR HIGH CONCENTRATOR PHOTOVOLTAIC SYSTEM

Lee Pei Shan

A comprehensive optical analysis on assembly of dielectric-filled 3-D crossed compound parabolic concentrator (CCPC) and concentrator photovoltaic (CPV) module is presented by embracing the consideration of spectral irradiance, incident angles and breakdown optical losses. The theoretical modelling supported by experiments has been carried out to evaluate the optical efficiency of the CCPC-CPV assembly module by investigating detailed optical losses at each layer of the components. From our breakdown optical analysis, total Fresnel reflection loss of 11.27%, absorption loss within CCPC lens of 11.59% and other losses of 4.79% are obtained to reach the optical efficiency of 77.3% of equivalent solar concentration ratio (SCR) of 4.65 out of geometrical concentration ratio (GCR) of 5.998 suns. Furthermore, indoor and outdoor measurements have proven the actual SCR of 4.57 and 4.48 respectively, which are also equivalent to optical efficiencies of 76.2% and 74.4% accordingly. The experimental results have strongly verified the simulated result of optical analysis on CCPC-CPV assembly module. The comprehensive theoretical modelling of secondary optics is essential for the performance optimization of CPV system in the future.

ACKNOWLEDGEMENT

This thesis is prepared as a partial requirement for the degree of Master of Engineering Science in University Tunku Abdul Rahman. The successful production of this report involves many valuable contributions from a number of parties and as a token of appreciation I would like to dedicate this page to them.

First, I would like to deliver my sincere gratitude towards my main supervisor, Dr. Tan Ming Hui as well as my former supervisor, Dr. Wong Chee Woon. They always give me a hand if I had any questions regarding my research. Without their patience, kind guidance and motivations, this project would not have been a success. Imparting their invaluable knowledge and experience has led to the success of this project which has increased my knowledge and confidence. I would also like to thank my co-supervisor Prof. Dr. Chong Kok-Keong for all his advice and guidance. He was very supportive, always gave me ideas and advises on my writing.

Secondly, I would also like to express my appreciation to all the research partners, postgraduate and Final Year Project students: Dr. Yew Tiong Keat, Dr. Tan Weoi Chong, Oon Li Voon, Soon Kok Yew, Nneka Onubogu and Khor Chaw Ming who all cooperated and worked with me in conducting the experiments. Besides, I would also like to thank my parents and friends for their unreserved support, inspiration and encouragement given throughout this project.

Lastly, a special thanks to all the staff at UTAR Institute of Postgraduate Studies and Research (IPSR) and Lee Kong Chian Faculty of Engineering & Science (LKC FES) who extended their assistance and providing me with the facilities and expertise.

My heartiest thanks and gratitude.

APPROVAL SHEET

This thesis/dissertation entitled “OPTICAL ANALYSIS OF CROSSED COMPOUND PARABOLIC CONCENTRATOR FOR HIGH CONCENTRATOR PHOTOVOLTAIC SYSTEM” was prepared by LEE PEI SHAN and submitted as partial fulfilment of the requirements for the degree of Master of Engineering Science at Universiti Tunku Abdul Rahman.

Approved by:



(Dr. TAN MING HUI)

Date:.....27/7/2021.....

Main Supervisor

Department of Industrial Engineering

Faculty of Engineering and Green Technology

Universiti Tunku Abdul Rahman

K.K.Chong

(Prof. Dr. CHONG KOK KEONG)

Date:.....28/7/2021.....

Professor / Co-supervisor

Department of Electrical and Electronic Engineering

Lee Kong Chian Faculty of Engineering and Science (LKC FES)

Universiti Tunku Abdul Rahman

FACULTY OF ENGINEERING AND SCIENCE
UNIVERSITI TUNKU ABDUL RAHMAN

Date: 28 July 2021

SUBMISSION OF THESIS

It is hereby certified that **Lee Pei Shan** (ID No: 17UEM06742) has completed this thesis entitled “OPTICAL ANALYSIS OF CROSSED COMPOUND PARABOLIC CONCENTRATOR FOR HIGH CONCENTRATOR PHOTOVOLTAIC SYSTEM” under the supervision of Dr. Tan Ming Hui (Supervisor) from the Department of Industrial Engineering, Faculty of Engineering and Green Technology, and Prof. Dr. Chong Kok Keong (Co-Supervisor) from the Department of Electrical and Electronics Engineering, Lee Kong Chian Faculty of Engineering Science.

I understand that the University will upload a softcopy of my thesis in pdf format into UTAR Institutional Repository, which may be made accessible to UTAR community and the public.

Yours truly,



(LEE PEI SHAN)

DECLARATION

I, LEE PEI SHAN hereby declare that this thesis is based on my original work except for quotations and citations which have been duly acknowledged. I also declare that it has not been previously or concurrently submitted for any other degree at UTAR or other institutions.

Name: LEE PEI SHAN

Date: 28 July 2021

TABLE OF CONTENTS

	Page
ABSTRACT	ii
ACKNOWLEDGEMENT	iii
APPROVAL SHEET	v
SUBMISSION OF THESIS	vi
DECLARATION	vii
TABLE OF CONTENTS	viii
LIST OF TABLES	xi
LIST OF FIGURES	xiii
LIST OF ABBREVIATIONS	xviii
CHAPTER	
1.0 INTRODUCTION	
1.1 Introduction	1
1.2 Research Background	1
1.3 Research Objectives	5
1.4 Outline of Thesis	5
2.0 LITERATURE REVIEW	
2.1 Introduction to CPV system	7
2.2 Types of secondary optical element	8
2.2.1 Reflective light funnel	8
2.2.2 Compound Parabolic Concentrator (CPC)	13
2.2.3 Dome lens	17
2.2.4 Kaleidoscope	21
2.2.5 Diffractive secondary	24
2.3 Evaluation of secondary optical element	28
3.0 METHODOLOGY	
3.1 Overview of UHCPV system	31
3.1.1 Design of primary optical element	32
3.1.2 Overview of CCPC-CPV assembly module	33

3.1.3	Multi-junction solar cell	36
3.2	Performance evaluation of CCPC-CPV assembly module	39
3.2.1	Ray tracing simulation	41
3.2.2	Simulation for different angle of incidence	50
3.2.3	Performance evaluation of the UHCPV system	53
3.3	Numerical analysis	54
3.4	Experimental setup	55
3.4.1	Assembling CCPC-CPV assembly module	56
3.4.2	Indoor measurement	57
3.4.3	Outdoor measurement	61
4.0	RESULT AND DISCUSSION	
4.1	Comparison between full solar spectrum and single wavelength in simulation	64
4.2	The optical behaviour under different angle of incidence	65
4.3	Optical efficiency profile of CCPC-CPV assembly module	72
4.4	Optical losses occur at each component level	75
4.5	Results for indoor and outdoor experiments	78
4.6	Overall performance of UHCPV system	84
5.0	CONCLUSION AND FUTURE WORK	
5.1	Conclusion	87
5.2	Recommended future works	88
	REFERENCES	90
	PUBLICATIONS	98
	APPENDICES	
	A. B270 SCHOTT GLASS	99
	B. AZUR SPACE 3C44	113
	C. REPORT AND CERTIFICATIONS OF ORIEL'S SOL1A CLASS ABB SOLAR SIMULATOR	117
	D. PUBLICATION: OPTICAL AND ELECTRICAL PERFORMANCE EVALUATION OF CROSSED COMPOUND PARABOLIC CONCENTRATOR MODULE FOR THE	

**APPLICATION OF ULTRA-HIGH CONCENTRATOR
PHOTOVOLTAIC SYSTEM 120**

**E. PUBLICATION: COMPREHENSIVE ANALYSIS ON
ASSEMBLY OF DIELECTRIC FILLED CROSSED
COMPOUND PARABOLIC CONCENTRATOR AND
CONCENTRATOR PHOTOVOLTAIC MODULE 127**

LIST OF TABLES

Table		Page
2.1	A summary of the existing secondary optics used in CPV system mentioned in literature review.	25
3.1	Specifications of the NIDC as the primary concentrator of the UHCPV system.	33
3.2	Specification of the secondary optics element used in UHCPV system.	36
3.3	Specification of the multi-junction solar cell (MJSC) used in this work (Azur Space, 2015).	38
3.4	Refractive indices, n of the components used in the CCPC-CPV assembly module.	43
3.5	Index coefficient for B270 Schott glass.	44
3.6	The refractive indices, absorption and extinction coefficient of B270 Schott glass for wavelength 300 nm to 1800 nm.	45
3.7	Light source position (X , Y) for zenith angle equal to 0° , 10° and 20° respectively.	52
3.8	Light source position (X , Y) for zenith angle equal to 30° and 37.77° (acceptance angle of CCPC lens) respectively.	53
3.9	The classification criteria of the three parameters of the Oriol's Sol1A TM Class ABB solar simulator (Newport Corporation, 2011).	58
4.1	The optical efficiency of the CCPC-CPV assembly module for zenith angle ranging from 0° to 37.77° and	67

	azimuth angle ranging from 0° to 360°.	
4.2	The optical losses at each component level of the CCPC module.	78
4.3	Indoor measurement for five MJSC and CCPC-CPV assembly modules respectively.	79
4.4	Outdoor data collection on 19 th February 2019, weather condition: sunny day with mostly clear skies.	80
4.5	Outdoor data collection on 21 st February 2019, weather condition: sunny day with mostly clear skies.	81
4.6	Outdoor data collection on 22 nd February 2019, weather condition: sunny day with mostly clear skies.	82
4.7	The outcome comparison between the simulation, indoor and outdoor experiment.	84

LIST OF FIGURES

Figure		Page
2.1	Illustration of light funnel concentrator concept (Boeing Aerospace Co., 1987)	9
2.2	The different light transmission pattern in a conventional paraboloid (left) and in an imaging concentrator (right) (Kaiyan, Hongfei and Tao, 2011).	10
2.3	The fabrication process of the prototype of V-trough concentrator module using aluminium sheets and strips of PV module. (a) Aluminium sheets (b) aluminium sheets are bent into the desired V-trough shape (c) schematic of PV cells connected to become a strip, (d) PV module strip and V-trough reflector mounted on the aluminium frame, and (e) additional high-reflectance reflector is mounted on the side walls (Solanki <i>et al.</i> , 2008).	12
2.4	Schematic diagram for the combination of light funnel concentrator with a deflector for oriented sunlight transmission (Zheng <i>et al.</i> , 2014).	13
2.5	The illustration of the 3-D CPC module (G. Dai <i>et al.</i> , 2011).	14
2.6	The schematic view of (a) common mirror CPC (b) solid CPC (c) lens-walled CPC (Su, Riffat and Pei, 2012).	16
2.7	The illustrated concept for the concentrating system presented by James and Lawrence in late 80's (a) under normal incidence (b) under incidence approaching	18

	acceptance angle (Hernández <i>et al.</i> , 2008).	
2.8	(a) The CPV system comprises of Fresnel lens and half-egg lens (b) ray-tracing of the half-egg lens with solar angle of $\pm 0.28^\circ$ under normal incidence at the direct normal insolation (DNI) of 850 W/m^2 (c) ray-tracing of the half-egg lens with an incidence angle of 0.5° for both x and y directions horizontally (Fu, Leutz and Annen, 2010).	19
2.9	(a) Modelling of the UHCPV with Cassegrain-based optical design. The labelled elements are (1) paraboloid mirrors (POE), (2) hyperboloid mirrors (SOE), (3) four-fold dome-shaped homogenizer and (4) solar cell (b) ray-tracing at the central receiver.	20
2.10	Side view of the kaleidoscope with the design parameters. The field of view is commensurate with the grid of virtual sources (Ries, Gordon and Lasken, 1997).	22
2.11	Schematic diagram of KOD-type SOE (a) design factors (b) 3-D model (Chen, Chiang and Hsieh, 2015).	23
2.12	Three dimensional illustration for the refractive cone and pyramid lens (El-yahyaoui <i>et al.</i> , 2019)	23
2.13	Diffraction lens is used as the secondary optics in the high concentration photovoltaics system (Sahin and Yilmaz, 2019).	24
3.1	The UHCPV system comprises of (a) POE: non-imaging dish concentrator (b) SOE: crossed compound parabolic	31

	concentrator (Wong <i>et al.</i> , 2017).	
3.2	(a) Cross sectional view of the dielectric-filled CCPC lens (b) 3-D geometry of an assembly CCPC-CPV module with refractive indices, n , of each component.	34
3.3	Azur Space 3C44 consisting of three layers: InGaP/InGaAs/Ge with a bandgap of 1.88 eV, 1.41 eV and 0.67 eV respectively.	37
3.4	External quantum efficiency (EQE) of the MJSC (Azur Space, 2015).	38
3.5	A summary of the evaluation process of the CCPC-CPV assembly module.	40
3.6	3-D modelling of the CCPC-CPV assembly module (1) CCPC lens, (2) optical adhesive, (3) MJSC.	42
3.7	Extinction coefficient, k and refractive index, n of B270 Schott glass throughout the wide range of solar spectrum.	48
3.8	The optical adhesive layer is inserted into the model for theoretical simulation.	49
3.9	(a) Definition of angles of incidences (Zenith angle, Φ_Z and Azimuth angle, Φ_A) of the light source relative to the CCPC lens during the simulation. (b) Light rays hitting on the CCPC lens' inner wall are mostly reflected onto the peripheral region of the CPV cell via total internal reflection.	50
3.10	Spherical coordinate is used to calculate the position of light source under different angle of incidence.	51

3.11	Complete set of CCPC-CPV assembly module (1) CCPC lens, (2) MJSC on DBC, (3) connecting wires.	57
3.12	Indoor experiment was set-up to measure the output current of the CCPC-CPV assembly module and for single MJSC respectively.	59
3.13	Five unit of CCPC-CPV assembly modules used for indoor measurement.	60
3.14	(a) The illustrative 3D model and (b) schematic diagram of the tester case.	62
3.15	Experimental setup for outdoor measurement.	62
4.1	Variation of solar concentration ratio of CCPC-CPV assembly module under full solar spectrum.	65
4.2	Ray tracing simulation of the CCPC-CPV assembly module under light source with azimuth angle, $\Phi_A = 0^\circ$ while zenith angle, Φ_Z equals to (a) 0° (b) 10° (c) 20° (d) 30° , and (e) 37.77°	66
4.3	The simulated flux distribution map on the MJSC receiver under different angles of incidence.	68
4.4	The ray tracing simulation of the CCPC-CPV assembly module from various points of view when (a) $\Phi_A = 90^\circ$ and $\Phi_Z = 37.77^\circ$, (b) $\Phi_A = 45^\circ$ and $\Phi_Z = 37.77^\circ$.	69
4.5	The simulated flux distribution map on the MJSC receiver with $\Phi_A = 0^\circ, 90^\circ, 180^\circ$ and 270° while $\Phi_Z = 37.77^\circ$.	70
4.6	The optical efficiency of the CCPC-CPV assembly	71

	module in 2D-plot for zenith angle from 0° to 37.77° and azimuth angle from 0° to 360° .	
4.7	Distribution of solar concentration ratio at different angles of incidence.	71
4.8	Light rays fall on the edge of side wall is lost for unknown reason.	72
4.9	The optical efficiency profile of CCPC-CPV assembly module indicates severe optical losses are incurred at the edge/corner under direct normal irradiance. (a) Computational result. (b) Top view of actual CCPC-CPV assembly module observed with the naked eye.	73
4.10	Escaping light rays due to adhesive spillage.	74
4.11	The optical efficiency of CCPC-CPV assembly module versus different zenith angle, Φ_Z , while azimuth angle, $\Phi_A = 0$, for different thicknesses of adhesive layer, t_{al} .	75
4.12	Optical losses occur at each of the component level.	77
4.13	SCR of the CCPC-CPV assembly module under different solar irradiance.	83
4.14	Ray-tracing simulation for the UHCPV system.	85
4.15	The simulated flux distribution map on (a) the CCPC lens' entrance apertures (b) the MJSCs.	86

LIST OF ABBREVIATIONS

$2a$	Entrance aperture of the CCPC lens (mm) = 24 mm
$2a'$	Exit aperture of the CCPC lens (mm) = 9.8 mm
2-D	Two dimensional
3-D	Three dimensional
A_{active}	Active area of MJSC (mm^2) = 100 mm^2
AlOx	Aluminium oxide
ARC	Anti-reflective coating
ARC-air	Anti-reflective coating adaptive to air
ARC-glass	Anti-reflective coating adaptive to glass
c	Speed of light in vacuum (ms^{-1}) = $3 \times 10^8 \text{ms}^{-1}$
$C(\lambda)$	Spectral SCR (suns)
CAD	Computer-aided drafting
CCPC	Crossed compound parabolic concentrator
CPC	Compound parabolic concentrator
CPV	Concentrator photovoltaic system
DBC	Direct bonded copper
EQE	External quantum efficiency
GCR	Geometrical concentration ratio (suns)
Ge	Germanium
h	Planck's constant (Js) = 6.63×10^{-34} Js.
H	Height between the receiver's entrance aperture and opening (mm)
$I_{CCPC-CPV}$	Output current of CCPC-CPV module (mA)

I_{CPV}	Output current of CPV cell without CCPC lens (mA)
InGaAs	Indium Gallium Arsenide
InGaP	Indium Gallium Phosphide
I_{SC}	Short circuit current (A)
k	Extinction coefficient
KFTS	Kaleidoscope with flat top surface
KOD	Kaleidoscope with equal optical path design
L	Length of the CCPC lens (mm) = 37.78 mm
$L1$	Half-length of the receiver (mm)
$L2$	Gap between the opening and the edge of receiver (mm)
LCOE	Levelized cost of electricity
LCSE	Levelized cost of solar electricity
MJSC	Multi-junction solar cell
n	Refractive index
NASA	National Aeronautics and Space Administration
NIDC	Non-imaging dish concentrator
POE	Primary optical element
PV	Photovoltaic
q	Electronic charge (C) = 1.6×10^{-19} C
r	Radial distance from the origin (mm)
$R_{Fresnel}$	Fresnel reflection loss
RTV	Room temperature vulcanizing
SCR	Solar concentration ratio (suns)
$S_L(\lambda)$	Spectral irradiance of light source ($W \cdot m^{-2} \cdot nm^{-1}$)
SOE	Secondary optical element

SP	Specular walls
t_{al}	Thickness of adhesive spillage surrounding the bottom edge of the CCPC lens (mm)
T_e	External Transmittance
T_i	Internal Transmittance
TiOx	Titanium oxide
TOE	Tertiary optical element
UHCPV	Ultra-high concentrator photovoltaic system
UTAR	University Tunku Abdul Rahman
V_{oc}	Open circuit voltage (V)
θ'_i	Half acceptance angle ($^\circ$) = 24.1 $^\circ$
θ_i	Angular half acceptance angle ($^\circ$) = 37.77 $^\circ$

Greek symbols:

η_{EQE}	EQE of any p-n junction sub-cell in the MJSC
$\eta_{optical}$	Optical efficiency (%)
α	Absorption coefficient (mm^{-1})
$\angle\alpha$	Tracking error ($^\circ$)
$\angle\beta$	Full view angle ($^\circ$)
Φ_Z	Zenith angle ($^\circ$)
Φ_A	Azimuth angle ($^\circ$)

CHAPTER 1

INTRODUCTION

1.1 Introduction

In this chapter, the research background, the problem statement, the aims of the project as well as the scope of project will be discussed.

1.2 Research Background

The development of sustainable energy for generating electricity is vital for the future of mankind as non-renewable energy resources release pollutants and is exhaustible. Many researchers have been worked on the technologies of renewable energy in order to provide a safe environment and sustainable power production to the future generation.

There are many types of sustainable energy being used all around the world for electricity production, such as wind, solar, geothermal, hydropower and so on. A photovoltaic system is one great alternative to complement and replace conservative resources in the future. According to the U.S. Department of Energy, the amount of solar power that reaches on Earth every one and a half hour is actually more than the worldwide consumes in a year (Tsao, Lewis and Crabtree, 2006). Solar energy should be able fulfil the worldwide energy

demands. However, the current technologies for harvesting this energy from sun are still negligible (Kabir *et al.*, 2017).

Researchers around the world have been working for years to develop a reliable way to capture and convert solar energy into usable electricity. Concentrator photovoltaics system has been a trend towards the research and development of solar technologies since multi-junction solar cells (MJSC) came out (Green *et al.*, 2015). The cell is a combination of three series-connected layers of semiconductor materials with diverse bandgaps to absorb a wider range of solar spectrum. Therefore, it can generate higher power as compared to conventional silicon solar cells. From the datasheet, it is recognized that the MJSC could achieve conversion efficiency up to 46% (Azur Space, 2015).

The integration of optics and MJSC in a solar system is defined as concentrator photovoltaic (CPV) system. It plays an important role in the growth of ultra-high concentrator photovoltaic (UHCPV) system as it can transform highly concentrated sunlight into electrical energy. With the use of optics such as mirrors and lens, the sunlight can be focused onto the receiver that is fitted out with MJSC and generate more than a 1000 suns of ultra-high solar concentration ratio. Some of the most common optics used in a CPV system is parabolic concentrator, Fresnel lens, refractive kaleidoscope etc. These optics can greatly minimize the usage of semi-conductor material and the levelized cost of solar electricity (LCSE). The utilization of optics is also inexpensive compared to the solar cell made of semiconductor materials. However, due to the rapid development in flat PV panel, the optimization of CPV systems is indeed so that it can be more competitive in the market.

An efficient way of solar energy harvesting can be challenging due to the chromatic aberration limits for single material lenses. A number of scholars have been introduced several types of multi-stage concentrator photovoltaic system to achieve ultra-high SCR with excellent optical performances (Fu, Leutz and Annen, 2010; Pérez-Higueras *et al.*, 2015; Ferrer-Rodriguez *et al.*, 2016; Wong *et al.*, 2017; Shanks *et al.*, 2018). A previous investigation advocated that by using homogenizing lenses as secondary stage concentrator, a concentrator photovoltaic system is able to exceed the limitation and capable of achieving SCR above 1000 suns. In addition, the researchers agree that the structure and performance of the optics requires to be investigated further to make the CPV system cost competitive to the flat plate photovoltaic. This especially applies on secondary optics because it hold a huge potential for enhancing the acceptance angle and optical tolerance of a CPV system (Shanks, Senthilarasu and Mallick, 2016).

In a previous work presented by Wong *et al.*, an UHCPV system with the integration of two-stage non-imaging solar concentrator comprises of non-imaging dish concentrator (NIDC) as the primary optical element (POE) and crossed compound parabolic concentrator (CCPC) lens as the secondary optical element (SOE) is introduced (Wong *et al.*, 2017). The presented work is able to produce an ultra-high SCR of 1475 suns and a reasonably uniform solar illumination homogenized onto the MJSCs module. The general features of the CCPC lens have been discussed in their previous work (T. Yew, Chong and Lim, 2015) and an experiment was conducted (Chong *et al.*, 2017) to inspect the performance of the CCPC lens under direct exposure to the sun. However, not much details about the optical performance is revealed in their study. Many

more details such as the effect of solar spectrum, the optical behaviour of the optics under omnidirectional light source etc. are yet to be discovered. The optical characteristics and performance of the SOE need to be studied in order to develop a reliable solution to the main issue.

The detailed of optical losses in the integration of CCPC and CPV cell remains unknown, despite it has been introduced in high CPV system. As the CPV system mainly rely on optical elements, identifying the underlying causes of the optical losses helps to develop the genuine solution for optimizing the overall performance including optical and electrical efficiency. Only through analysing the causes of the problem, we will be able to see which strategies will be most appropriate to tackling it. Taking action without identifying what factors contribute to the problem could result in misdirected efforts. A good understanding of the optical characteristics is the key to optimize the performance of a CPV system. Thus, in this thesis, a detailed study on the optical characteristics of CCPC module, an assembly of a dielectric-filled 3-D CCPC lens and a MJSC has been evaluated. The evaluations were examined through 3 phases – computational simulation, indoor and outdoor experiment. The light source used in the simulation was based on the spectral output of AM1.5 and ranged from 300 – 1800 nm corresponding to MJSC's spectral response.

1.3 Research Objectives

In this study, a comprehensive optical characterization of the Crossed Compound Parabolic Concentrator (CCPC) module as the secondary optics of the ultra-high concentrator photovoltaic (UHCPV) system is presented through computational and laboratory methods. The main objectives are as follows:

- a) To develop a ray-tracing numerical simulation technique to investigate the characteristics of the CCPC module for the application of UHCPV system.
- b) To identify the optical losses of the CCPC module.
- c) To perform indoor and outdoor experiment to validate the ray-tracing numerical simulation technique.
- d) To evaluate the optical performance of the CCPC module.

1.4 Outline of Thesis

In this thesis, the optical characterization and performance of the CCPC will be discussed and the organization of the thesis will be presented in the following sections:

- Chapter 1 introduces the research background and the existing problem under study.
- Chapter 2 gives a literature review on the existing works from other researchers.
- Chapter 3 describes an outline of the methodology used in this research. The design concept of the CCPC lens, assembly of the prototype module, numerical ray-tracing technique with the aid of opto-mechanical software, procedure and experimental setup for indoor and outdoor experiment will be described in detail.

- Chapter 4 presents the result and discussion based on the computational and experimental findings. Both findings will be analyzed and compared to validate the accuracy and reliability of the methodology proposed.
- Chapter 5 will be the wrap for this thesis. A conclusion of the overall research and recommended future work will be provided.

CHAPTER 2

LITERATURE REVIEW

2.1 Introduction to CPV system

In recent years, the development of concentrator photovoltaic (CPV) system has been getting more interest from the researchers as the alternative of the renewable energy sources. The idea of concentration photovoltaic is first introduced in mid-1970s to compete with traditional fossil fuel plants. The researchers in the Sandia National Laboratories of Albuquerque, New Mexico developed the first prototype of linear-trough CPV system with a concentration ratio of 40× suns by using Fresnel lenses and water-cooled solar cell (Burgess and Pritchard, 1978; Swanson, 2000; Luque, Sala and Ignacio Luque-Heredia, 2006).

By making use the principle of optics, optical elements are installed to intensify the solar irradiance power onto the decreased areas of photovoltaic (PV) cell. Thus, the high cost semiconductor materials can be offset by the inexpensive optical devices while efficiency increases as it is able generate higher electric power under highly concentrated solar light (Zubi, Bernal-Agustín and Fracastoro, 2009; Shanks, Senthilarasu and Mallick, 2016).

The solar concentration ratio (SCR) is defined as the ratio of solar irradiance entering the collector to the solar irradiance received by the receiver in which it represents the system's ability to enhance the solar energy

(Hoffschmidt *et al.*, 2012). The configuration of the CPV systems can be classified as follows based on its concentration factor (Algora and Rey-Stolle, 2012):

- Low concentration : Less than 10 suns
- Medium concentration : 10 to 100 suns
- High concentration : 100 to 1000 suns
- Ultra-high concentration : More than 1000 suns

The optical devices that are commonly employed in a CPV system are mirrors, lenses (refractive or reflective) or a combination of both.

2.2 Types of secondary optical element

Many researchers have been proposed different types of secondary optical elements (SOE) in their CPV system to achieve higher SCR with good optical performances. The SOE are either refractive or reflective while some of the conventional concentrators are compound parabolic concentrator (CPC), kaleidoscope, dome-shaped lens and reflective light funnel. The characterizations of different types of SOE are presented in the next section and a summary of all the literature reviewed is listed in Table 2.1.

2.2.1 Reflective light funnel

A light funnel relies on reflective or refractive components to intensify solar reflections onto the solar cell. The common geometry designs for light funnel

concentrator can be paraboloid, cone, pyramid, V-shape and so on. According to a report released by NASA (National Aeronautics and Space Administration), the working principle of a light funnel relies on the phenomenon of total internal reflection that it would be possible to lead solar incidents onto a concentrator solar cell (Boeing Aerospace Co., 1987). Figure 2.1 depicts the cross-sectional schematic diagram of a typical light funnel concentrator. The angle θ and β named by the researchers, must be designed in accordance with the refractive index of the material used so that total internal reflection happens. In effect, the light entering from the top will be trapped by internal reflection and directed to the exit aperture. This results in a hot spot of highly diffuse incident.

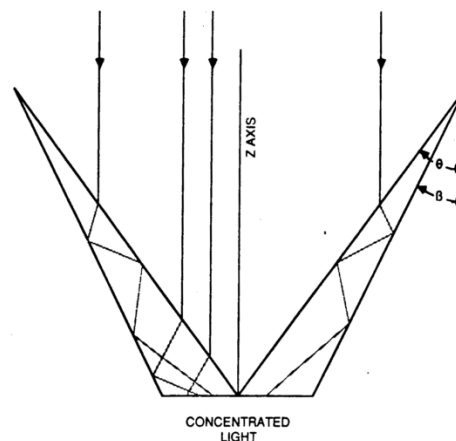


Figure 2.1: Illustration of light funnel concentrator concept (Boeing Aerospace Co., 1987)

The researchers claim that reflection loss is the only losses that might be affecting the performance of a light funnel concentrator. Roughly 4% of reflection losses happen at each interface of glass and air under normally incident light (Boeing Aerospace Co., 1987). This outcome provides an idea for the Fresnel reflection losses to be included in this project. When the light rays travelling through surfaces or materials with different refractive indices, a portion of light will be reflected away from the original pathway, which resulted in partial optical losses (Couny, Benabid and Light, 2007).

Kaiyan et al. developed a compound concentrator made of multiple curved surfaces by combining a parabolic and a flat contour. It was also known as imaging CPC. The concentrator's focus, F is at the backside where the reflected incidents are transmitted in opposite way compared to the traditional paraboloid concentrator as seen in Figure 2.2. Due to the position of the focus, the receiver module and the supporting frame could be easily mounted close to the exit aperture, which helps a lot in dissipating the heat (Kaiyan, Hongfei and Tao, 2011). At the same time, it provides more flexibility and convenience for the researchers to design for various application.

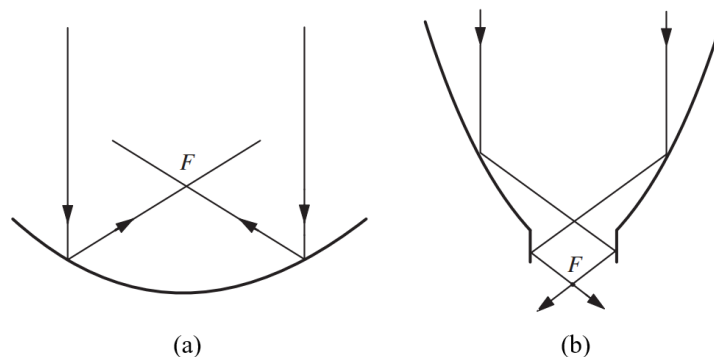


Figure 2.2: The different light transmission pattern, (a) in a conventional paraboloid (b) in an imaging concentrator (Kaiyan, Hongfei and Tao, 2011).

Tang and Liu suggested a V-trough concentrator for the application of photovoltaic system due to the higher uniformity of the light intensity on the exit area. Moreover, the excess heat can be dissipated easier through its side wall (Tang and Liu, 2011). The similar concept has been utilized in an earlier study by Solanki and colleagues in which a prototype of V-trough PV module is designed to overcome the high temperature cumulated in solar cells due to the concentrated solar incidents. The fabrication process is presented in Figure 2.3. A layer of anodized aluminium sheets are mounted on the inner surface of the V-trough as shown in Figure 2.3(e) to improve the reflectivity of the reflective walls (Solanki *et al.*, 2008). This design is really inspiring as the use of anodized aluminium sheets or other similar materials could be useful for the optimization of the CPV system proposed in this project. The light rays leaking from the adhesive spillage is one of the optical losses encountered in this project. The reflective sheets could be a good solution to this issue. On the other side, the cell temperature in this design is controlled as it remains almost the same with the flat PV module despite the highly concentrated light. The increased cell temperature was responsible for the performance drop on solar cell as well as the degradation of its operating life (King *et al.*, 2000).

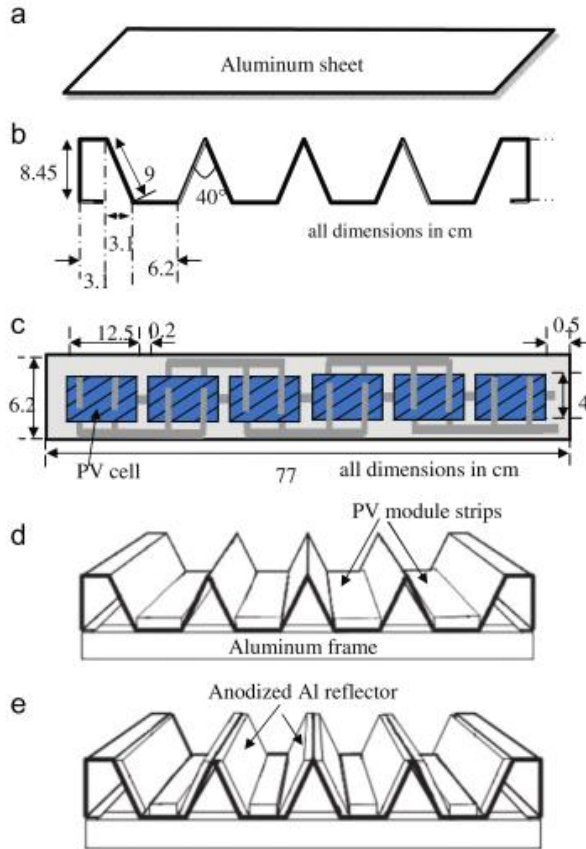


Figure 2.3: The fabrication process of the prototype of V-trough concentrator module using aluminium sheets and strips of PV module. (a) Aluminium sheets (b) aluminium sheets bent into the desired V-trough shape (c) schematic of PV cells connected to become a strip, (d) PV module strip and V-trough reflector mounted on the aluminium frame, and (e) additional high-reflectance reflector is mounted on the side walls (Solanki *et al.*, 2008).

On top of the optical principle of light funnel, Zheng et al. presented a modified version of light funnel concentrator with a deflector. A parabolic reflector is attached to the exit of the light funnel as illustrated in Figure 2.4, and the concentrated incident will be funnelled down to the centralized receiver. The feasibility of the system is verified via ray tracing simulation and

experiment. The outcome shows that with the use of whole parabolic deflector, the focal speckle distributed on the receiver has higher consistency and uniformity compared to half paraboloid deflector (Zheng *et al.*, 2014).

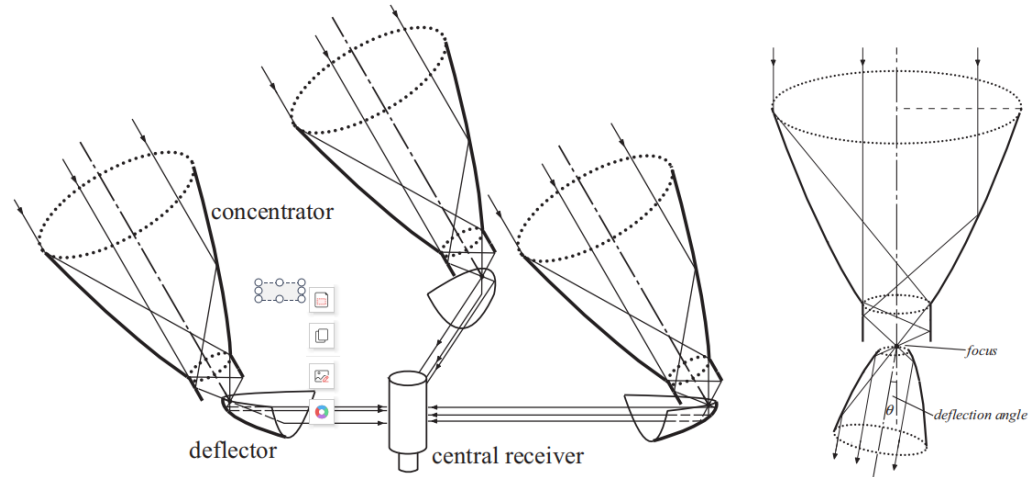


Figure 2.4: Schematic diagram for the combination of light funnel concentrator with a deflector for oriented sunlight transmission (Zheng *et al.*, 2014).

2.2.2 Compound Parabolic Concentrator (CPC)

The history of compound parabolic concentrator (CPC) begins in mid-1960s (Welford and Winston, 1978). The key advantage of CPC is that it allows wider acceptance angle and remains stable at the same time compared to other concentrators (Victoria, Dom and Ant, 2009). Many versions of CPC have been investigated in former studies, such as atypical 3-D CPC, lens-walled CPC, crossed CPC (CCPC).

Dai *et al.* had used a single 3-D CPC as the secondary optics for their two-stage solar concentrator while the primary stage was formed by a dish concentrator. The idea of the 3-D CPC module used as secondary optic is

depicted in Figure 2.5, where $\Delta\theta$ represents the incident angle, L is the length of the 3-D CPC module, r_0 and r_1 represent the radius of the entrance aperture and exit aperture respectively. The solar concentrating performance of the system has been investigated under two scenarios: (i) only dish concentrator is used (ii) the combination of dish concentrator and 3-D CPC are used. In their study, the numerical result shows that the intercept efficiency of using the integrated system is approximately 4.0% higher and concentration ratio for the latter scenario is twice that of using only the dish concentrator (G. Dai *et al.*, 2011). This is evidence that a multi-stage concentrator photovoltaic system is the key to boost the solar concentration ratio.

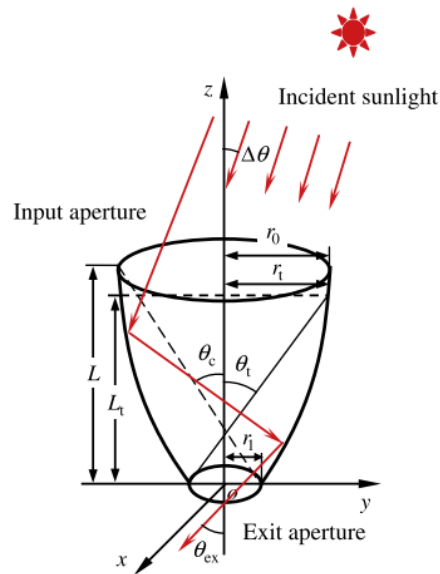


Figure 2.5: The illustration of the 3-D CPC module (G. Dai *et al.*, 2011).

Su and team had proposed a novel lens-walled CPC in their study in which it has a thin CPC-shape lens bonded to the inner side of a mirror CPC. The alternative is to mirror-coat the outside surface of the lens. The researchers claimed that a lens-walled CPC could collect the incoming light at a greater angle of incidence compared to mirror CPC while it has lighter weight

compared to a solid CPC (Su *et al.*, 2012). A comparison between the lens-walled CPC together with the common mirror CPC and a solid CPC was then presented in their later study. The schematic view for the three designs is shown in Figure 2.6. The concentration ratio for all three modules is 2.5. A mirror CPC consists of two parabolic curves (AB and CD) in which the axes of symmetry tilted to form the acceptance angle (AOD). The configuration of a solid CPC is the same as mirror CPC but filled with dielectric material. The back surface of the lens-walled CPC can direct the incident to the outlet of the lens via second refraction. The outcome showed that the lens-walled CPC is indeed providing a greater acceptance angle compared to the other two, but its optical efficiency is the lowest among all three when the incident angle is within the half acceptance angles (Su, Riffat and Pei, 2012). Based on their evaluation in various aspect, solid CPC earned the best score among three as lens-walled CPC only yields approximately 80% of the solid CPC's performance in terms of accumulative solar energy collection even though it provides bigger acceptance angle. This evidence shows that solid CPC is a better option compared to other design of CPC.

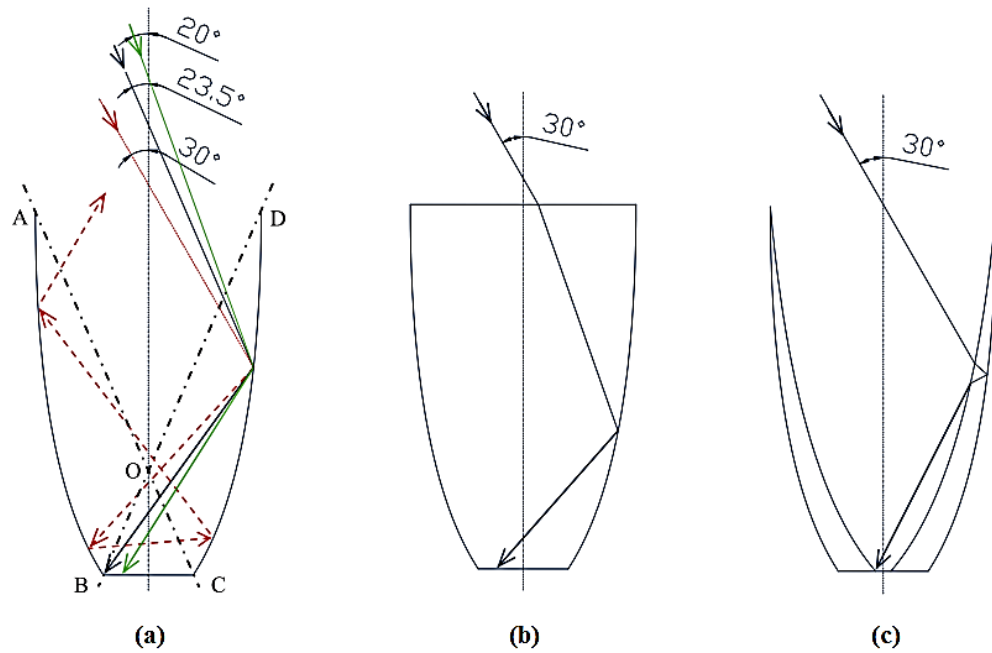


Figure 2.6: The schematic view of (a) common mirror CPC (b) solid CPC (c) lens-walled CPC (Su, Riffat and Pei, 2012).

Cooper et al. presented an analysis on polygonal CPCs to find out the most promising geometry for CPC except from revolved CPC. The tested polygonal CPCs having number of sides, $n = 3, 4, 5, 6, 8$ and 12 . The result showed that when the number of sides increases, the acceptance efficiency increases. Revolved CPC gave out the highest efficiency while polygonal CPC with $n \geq 4$ are within 5% of it. However square CPC ($n = 4$) also showed some strange but notable behaviour. It achieved higher acceptance efficiency than hexagonal and pentagonal CPC for acceptance angle less than 17° even though it has lesser number of sides (Cooper *et al.*, 2013). Consequently, a square CPC is more suitable to use as secondary concentrator as too many sides might increase the complexity of fabricating process. Besides, if we want to use a CPC as the homogenizer for PV cell receiver, the shape of the receiver must be included into consideration (Sellami, Mallick and Mcneil, 2010; Mammo,

Sellami and Mallick, 2012; Baig *et al.*, 2014). Apparently, a square exit aperture can match better with the CPV receiver as most of the commercial solar cell are fabricated in square or rectangular shape.

2.2.3 Dome lens

A dome lens is a semi-sphere lens that well known for its wide acceptance angle. Several studies stated that a dome lens typically requires lesser material compared to a dielectric-filled CPC, and it is easier to manufacture due to its shape (Victoria, Dom and Ant, 2009; Shanks, Senthilarasu and Mallick, 2016). Apart from acceptance angle, it is also proven that the dome lens produced better irradiance distribution than other lens (Hernández *et al.*, 2008; Victoria, Dom and Ant, 2009). Acceptance angle is an important factor to consider in choosing a secondary optics as wider acceptance angle can provide more tolerance to other system components as well as the alignment requirements. In overall, it is possible to reduce the manufacturing and installing cost using homogenizer with greater acceptance angle (Victoria, Dom and Ant, 2009).

According to Hernández *et al.*, Sandia Labs introduced the first photovoltaic integrating concentrator in late 80's, and the concept is demonstrated in Figure 2.7 (Hernández *et al.*, 2008). The concentrating system presented by James and Lawrence is formed by integrating the primary Fresnel lens onto dome-shaped secondary optic, which can be either a half-ellipsoidal glass or a single surface lens (SILO). The SILO lens is a cylinder or cone lens moulded with half-egg top surface. It seems more convenient as it allows direct bonding to the solar cell. Through their study, it is verified that the solar image

could be uniformly penetrated on the solar cell regardless of the incident angle of incoming lights (James and W, 1989).

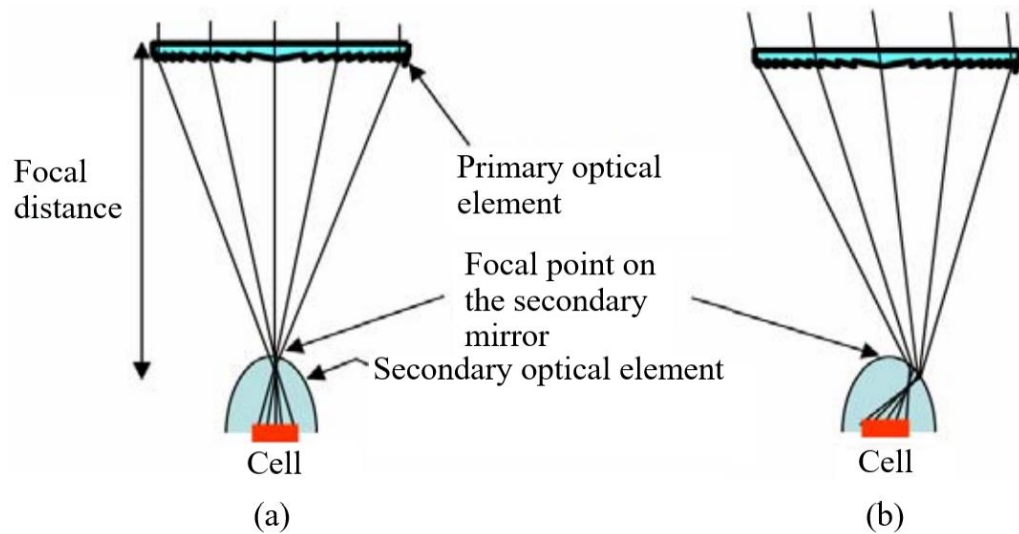


Figure 2.7: The illustrated concept for the concentrating system presented by James and Lawrence in late 80's (a) under normal incidence (b) under incidence approaching acceptance angle (Hernández *et al.*, 2008).

Fu, Leutz and Annen discussed the optical performance of the “half-egg” as the secondary for Fresnel lens in 2010. The proposed two-stage CPV system consists of Fresnel lens as POE while a half-egg homogenizer as SOE (as depicted in Figure 2.8) has geometrical concentration ratio of 800× suns. It is found that the “half-egg” secondary is exceptionally sensitive to the focal point’s position of primary optics. Although the irradiance distribution produced on top of the solar cell is relatively uniform under normal incidence, when the angle of incidence increases, it becomes progressively worse. Thus, it is concluded that a precise manufacturing of “half-egg” SOE is needed so that it can cooperate well with POE (Fu, Leutz and Annen, 2010).

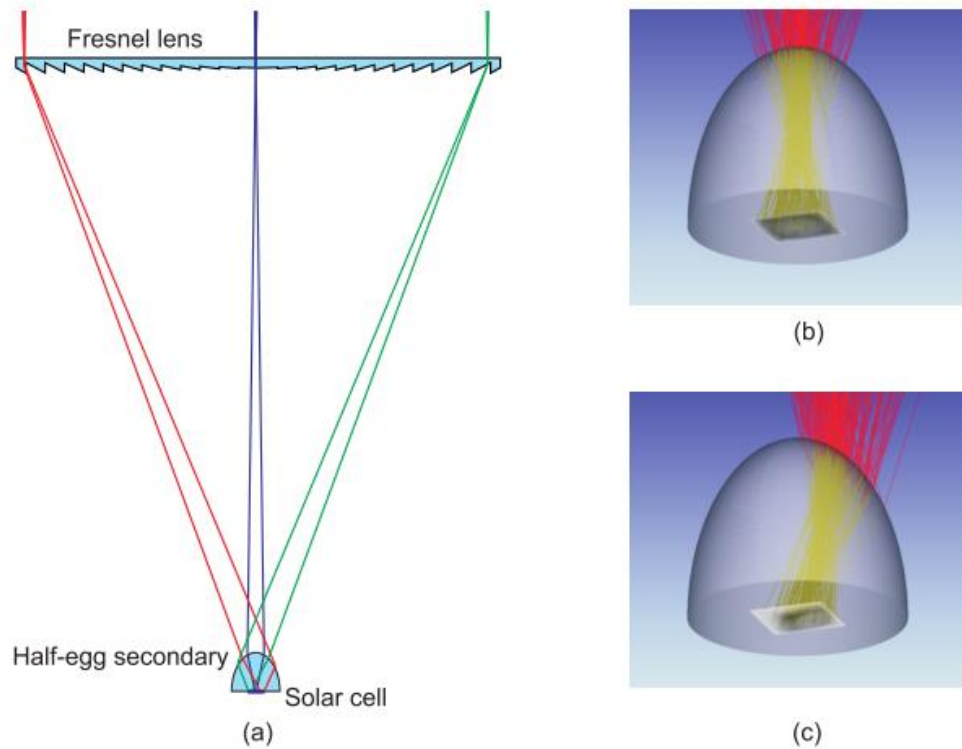


Figure 2.8: (a) The CPV system comprises of Fresnel lens and half-egg lens (b) ray-tracing of the half-egg lens with solar angle of $\pm 0.28^\circ$ under normal incidence at the direct normal insolation (DNI) of 850 W/m^2 (c) ray-tracing of the half-egg lens with an incidence angle of 0.5° for both x and y directions horizontally (Fu, Leutz and Annen, 2010).

Ferrer-Rodriguez and team presented a 4-off-axis-unit UHCPV based on Cassegrain optical design. The three-stage optical system as shown in Figure 2.9 used independent paraboloid (POE) and hyperboloid mirrors (SOE), four pieces each, and a glass cover as tertiary optical element (TOE) to concentrate and transmit the sunlight onto a MJSC receiver to attain effective SCR of 1682 suns. Nonetheless, the optical efficiency is capped at 73%

because of the shadowing and transmission losses (Ferrer-Rodriguez *et al.*, 2016).

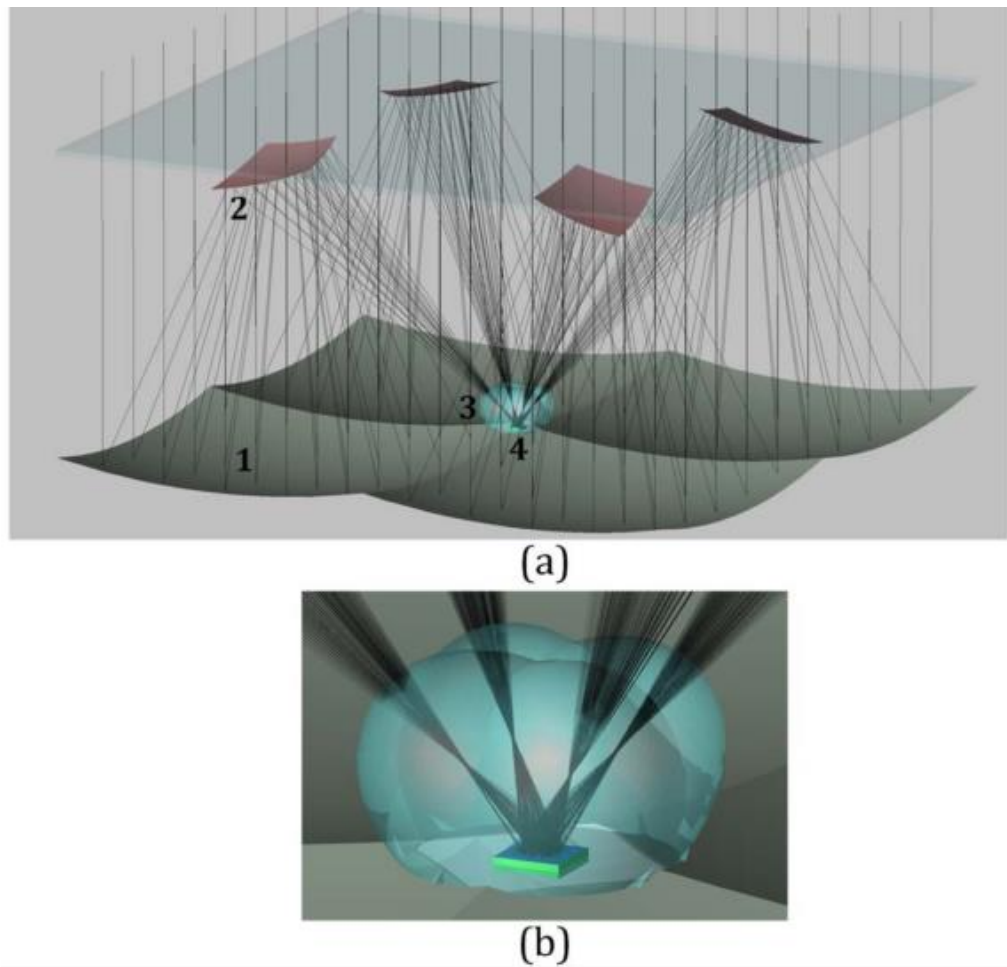


Figure 2.9: (a) Modelling of the UHCPV with Cassegrain-based optical design. The labelled elements are (1) paraboloid mirrors (POE), (2) hyperboloid mirrors (SOE), (3) four-fold dome-shaped homogenizer and (4) solar cell (b) ray-tracing at the central receiver.

2.2.4 Kaleidoscope

The idea of kaleidoscope was first patented at two centuries ago by Brewster and David (Brewster and Sir David, 1817). A kaleidoscope is similar to CPC but equips with rectangular reflective or refractive sidewalls.

Ries, Gordon and Lasken used a hexagonal reflective paraboloid dish as POE while used a hexagonal kaleidoscope as SOE in their high-flux photovoltaic concentrator system as presented in Figure 2.10. The parameters presented as D = dish diameter, f = dish focal length, H = distance from focal spot to absorber plane, W = kaleidoscope width, L = kaleidoscope depth and n = ratio of the linear dimension of the window to that of the unit cell of the grid. The image formed by the polygonal kaleidoscope is based on its geometry, one with square-based will produce a square grid. In terms of irradiance distribution, the utilisation of kaleidoscope secondary generated better minimum-to-maximum irradiance ratio than using POE only. In addition, the relative standard deviation is lower (Ries, Gordon and Lasken, 1997).

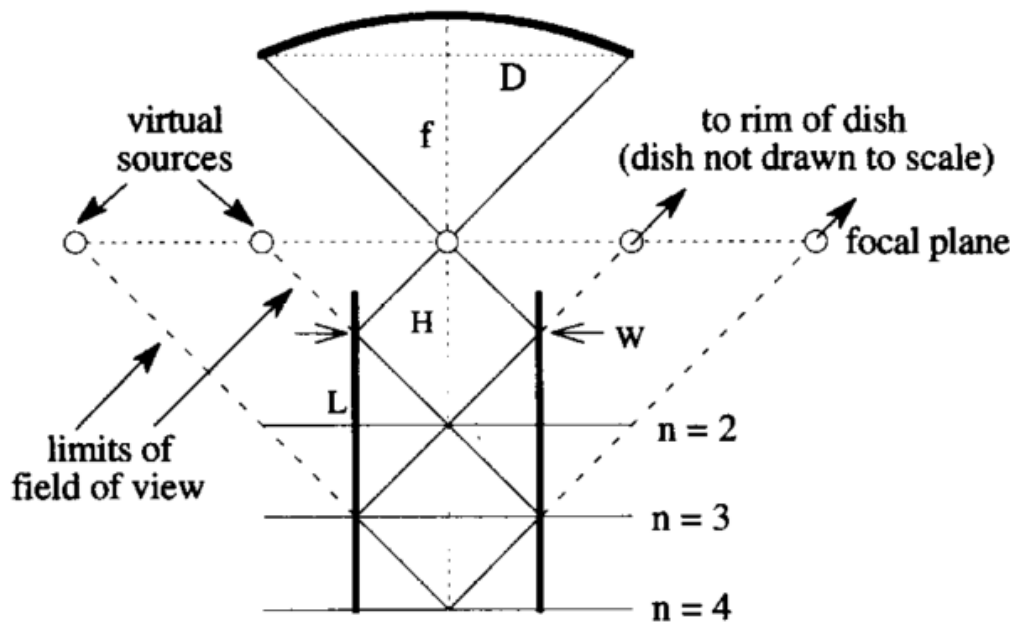


Figure 2.10: Side view of the kaleidoscope with the design parameters. The field of view is commensurate with the grid of virtual sources (Ries, Gordon and Lasken, 1997).

The similar idea was then discussed in Kreske's work in which a square or rectangular kaleidoscope is preferred to use as the receiver box. However, the shading of the receiver box causes more losses than expectation. A precise design is required for the supports used to hold the receiver box (Kreske, 2002).

Chen et al. evaluated three types of SOE with flat Fresnel lens which are kaleidoscope with equal optical path design (KOD), kaleidoscope with flat top surface (KFTS) and open-truncated tetrahedral pyramid with specular walls (SP). An optimized KOD lens is found to be the best in exhibiting irradiance distribution on the solar cell among the three SOEs. Nevertheless, the optical efficiency of KOD-type SOE drops significantly at an incidence angle of 2° , which indicates that the manufacturing for KOD-type SOE is difficult as it requires high tracking accuracy (Chen, Chiang and Hsieh, 2015).

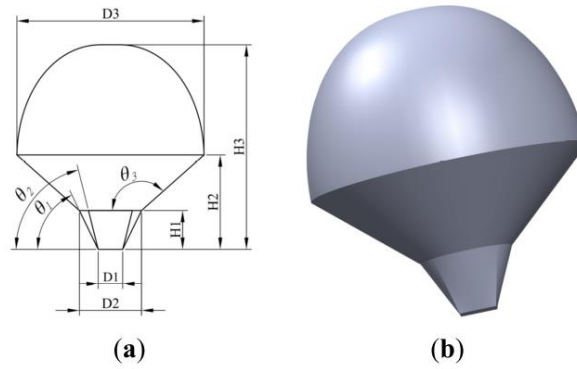


Figure 2.11: Schematic diagram of KOD-type SOE (a) design factors (b) 3-D model (Chen, Chiang and Hsieh, 2015).

Similarly, EL-yahyaoui et al. (El-yahyaoui *et al.*, 2019) investigated the performance of the two-stages optical concentrators consisted of PMMA Fresnel lens as the primary optical element (POE) with two types of SOEs: a pyramid lens and a cone lens made of fused silica (refer to Figure 2.12). In comparison, pyramid lens achieved higher optical efficiency of 73.7% as SOE in indoor experiment. The difference between simulation and experiment result is approximately 29% but no justification is given (El-yahyaoui *et al.*, 2019).

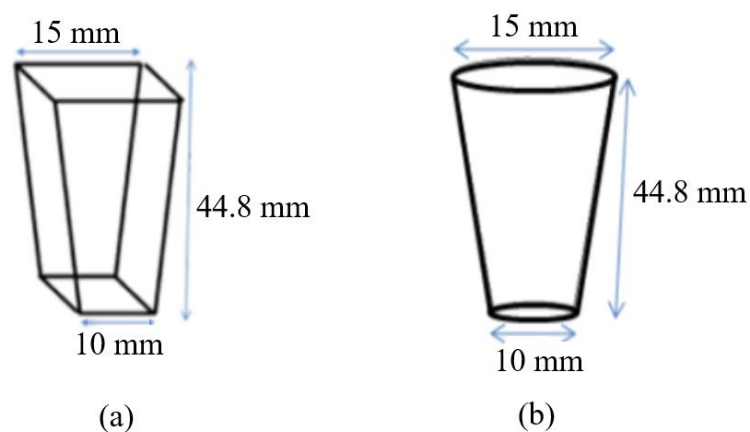


Figure 2.12: Three dimensional illustration for the (a) refractive cone and (b) pyramid lens (El-yahyaoui *et al.*, 2019)

2.2.5 Diffractive secondary

Sahin and Yilmaz (Sahin and Yilmaz, 2019) proposed a circular diffractive SOE instead of reflective or refractive optics as shown in Figure 2.13. The manufacturing process for large-area diffractive lens such as Fresnel lens can be challenging. However, if diffractive lens is used as secondary optics, it is easier to manufacture as the size reduces. In spite of the addition of diffractive SOE increases the optical efficiency of the CPV system by 6%, the real manufactured diffractive elements will come with discrete steps and cause deviation from the ideal model proposed in the paper (Sahin and Yilmaz, 2019).

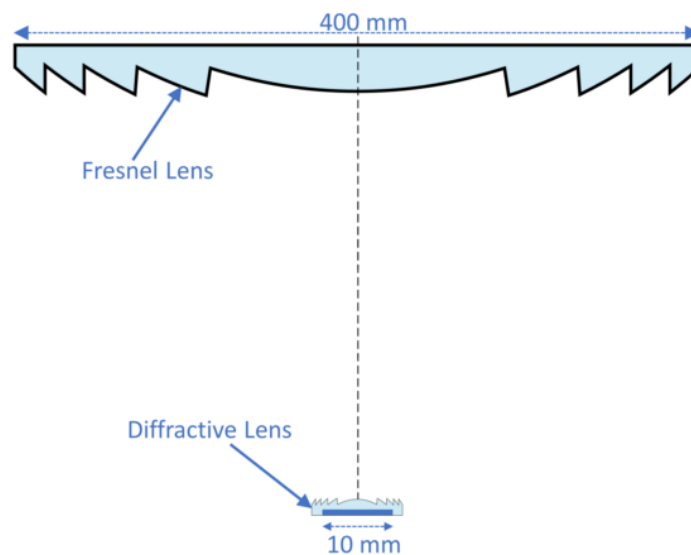


Figure 2.13: Diffractive lens is used as the secondary optics in the high concentration photovoltaics system (Sahin and Yilmaz, 2019).

Table 2.1: A summary of the existing secondary optics used in CPV system mentioned in literature review.

Authors	Title	Secondary optics used	Findings and discussion
Reflective light funnel			
Boeing Aerospace Co. (1987)	Light Funnel Concentrator Panel for Solar Power	Light funnel concentrator	<ul style="list-style-type: none"> • The geometrical parameters must be designed based on the refractive index of the material used to manufacture the light funnel so that total internal reflection occurs. • Reflection loss is the only loss that might be affecting the performance, Roughly 4% of reflection losses occur at each interface of glass and air under normally incident light.
Kaiyan et al. (2011)	A novel multiple curved surfaces compound concentrator	Imaging CPC	<ul style="list-style-type: none"> • The concentrator's focus is at the back side. • Light rays are transmitted forward instead of backwards compared to the conventional parabolic concentrators. • This design is extremely useful for some application.
Tang and Liu (2011)	Optical performance and design optimization of V-trough concentrators for photovoltaic applications	V-trough concentrator	<ul style="list-style-type: none"> • Able to produce light intensity with high uniformity. • Better dissipation of excess heat.
Solanki et al. (2008)	Enhanced heat dissipation of V-trough PV modules for better performance	V-trough reflector	<ul style="list-style-type: none"> • Solution for the high temperature cumulated in CPV cells.
Zheng et al. (2014)	Combination of a light funnel concentrator with a deflector for orientated sunlight transmission	Light funnel concentrator with a deflector	<ul style="list-style-type: none"> • Deflector is attached at the outlet of light funnel to direct the light beams to the central receiver. • Utilization of whole parabolic deflector creates focal speckle with higher consistency and uniformity than half paraboloid deflector.
Compound parabolic concentrator (CPC)			
Dai et al. (2011)	Numerical investigation of the solar	Single 3-D CPC	<ul style="list-style-type: none"> • The use of secondary optics doubled the concentration ratio of the CPV system.

	concentrating characteristics of 3D CPC and CPC-DC		
Su, Pei, et al. (2012)	Radiance/Pmap simulation of a novel lens-walled compound parabolic concentrator (lens-walled CPC)	Lens-walled CPC	<ul style="list-style-type: none"> • A thin CPC-shape lens attached to the inner wall of a mirror CPC. • Able to collect light rays from greater angle of incidence. • Lighter weight than solid CPC.
Su, Riffat, et al.	Comparative study on annual solar energy collection of a novel lens-walled compound parabolic concentrator (lens-walled CPC)	Lens-walled CPC	<ul style="list-style-type: none"> • Comparison is made with other types of CPC. • Lens-walled CPC has greatest angle of incidence but lowest optical efficiency when the incident angle is within the half acceptance angle.
Cooper et al. (2013)	Performance of compound parabolic concentrators with polygonal apertures	Polygonal CPCs	<ul style="list-style-type: none"> • When number of side increases, the acceptance efficiency increases. • Revolved CPC produces highest efficiency whereas CPC with four sides within 5% of it. • Square CPC showed some strange but notable behavior as it achieved higher acceptance efficiency than hexagonal and pentagonal CPC. • Square CPC is more suitable for the application of secondary optics as too many sides increase the complexity of the fabrication process. • Square CPC matches better with solar cells.
Dome lens			
Victoria et al. (2009)	Comparative analysis of different secondary optical elements for aspheric primary lenses	Several types of SOE are studied (Dome lens is mainly discussed in this section.)	<ul style="list-style-type: none"> • Lesser materials required than dielectric-filled CPC. • Dome shaper is easier to manufacture. • Better irradiance distribution. • Possible to reduce cost by using homogenizer with greater acceptance angle.
James and W (1989)	Use of imaging refractive secondaries in	Half-ellipsoidal glass or a single surface	<ul style="list-style-type: none"> • Solar image could be uniformly penetrated on the solar cell

	photovoltaic concentrators	lens (SILO)	regardless the angle of incidence of incoming lights.
Hernández et al. (2008)	High-performance Köhler concentrators with uniform irradiance on solar cell		
Fu, Leutz and Annen (2010)	Secondary optics for Fresnel lens solar concentrators	Half-egg homogenizer	<ul style="list-style-type: none"> • Half-egg secondary is extremely sensitive to the focal point's position of primary optics. • The irradiance distribution becomes progressively worse when the angle of incidence increases. • A precise manufacturing is required to cooperate with primary optics.
Ferrer-Rodriguez et al. (2016)	Optical Design of a 4-Off-Axis-Unit Cassegrain Ultra- High CPV Module with Central Receiver	Four-fold dome-shaped homogenizer	<ul style="list-style-type: none"> • The optical efficiency of the multi-stage solar system is studied. • No particular discussion on the dome-shaped homogenizer. • An effective SCR of 1682 suns is achieved.
Kaleidoscope			
Ries, Gordon and Lasken (1997)	High-flux photovoltaic solar concentrators kaleidoscope-based optical designs	Hexagonal kaleidoscope	<ul style="list-style-type: none"> • The solar image formed is based on its geometry. • Kaleidoscope secondary generates better minimum-t-maximum irradiance ratio than using single stage optics only. • Lower relative standard deviation.
Kreske (2002)	Optical design of a solar flux homogenizer for concentrator photovoltaics	Square or rectangular kaleidoscope	<ul style="list-style-type: none"> • The shading of the receiver box causes more losses than expectation. • A precise design is needed for the supports to hold the receiver box.
Chen et al. (2015)	Design of the Secondary Optical Elements for Concentrated Photovoltaic Units with Fresnel Lenses	<ul style="list-style-type: none"> • Kaleidoscope with equal optical path design (KOD) • Kaleidoscope with flat top surface (KFTS) • Open-truncated tetrahedral 	<ul style="list-style-type: none"> • An optimized KOD is the best in exhibiting irradiance distribution on the solar cell. • The manufacturing for KOD-type secondary optics is difficult as it required high tracking accuracy.

		pyramid with specular walls (SP)	
EL-yahyaoui et al/ (2019)	Indoor characterization of pyramid- and cone-type secondary optics	Pyramid lens and cone lens	<ul style="list-style-type: none"> • Pyramid lens achieved higher optical efficiency than cone lens. • The difference between simulated and experimental result is approximately 29% but no justification is given.
Diffraction secondary			
Sahin and Yilmaz (2019)	High Concentration Photovoltaics (HCPV) with Diffractive Secondary Optical Elements Furkan	Circular diffractive SOE	<ul style="list-style-type: none"> • Large area diffractive lens is hard to fabricate but smaller diffractive lens used as secondary optics is easier. • Diffractive SOE increases the optical efficiency of CPV system by 6%. • Actual manufactured diffractive lens will come with discrete step and cause bigger deviation from the ideal model proposed in the paper.

2.3 Evaluation of secondary optical element

From the past studies, it is known that although SOE can help to boost up the performance of the solar system, adding a secondary optics will also incur additional optical losses. Multiple optical devices in a system can lead to increasing optical losses as well as reducing the optical precision due to manufacturing and alignment errors (Languy and Habraken, 2013). However, all the studies above only provide a brief description about the optical efficiency but not much detail about the optical losses is revealed. More details such as the type of possible losses, the reason that causes those losses and how can it affect the overall performance should be revealed as we should know the optical losses before the overall efficiency in order to optimize the system more effectively. For instances, if reflective SOE is used in a project, the reflectivity

of the materials should be included in the discussion as no material can guarantee zero reflection loss.

Even though there are many types of homogenizing optics can be used as secondary concentrator, prior researches substantiate the belief that a 3-dimensional crossed compound parabolic concentrator (3-D CCPC) is the most ideal as it works perfectly for all light incidences within the desired acceptance angle (Winston, Miñano and Benitez, 2005; Sellami and Mallick, 2013). Thus, many efforts had been done by some researchers to study the optical characterization of the crossed compound parabolic concentrator as the secondary optics of a CPV system (Sellami, Mallick and Mcneil, 2010; Sellami and Mallick, 2013; Baig, Sellami and Mallick, 2015). For instances, a work studied by Sellami et al. presented a MATLAB code to test the optical efficiency and flux distribution on the solar cell of an improved atypical 3-D CCPC with different angles of incidences (Sellami, Mallick and Mcneil, 2010). However, the angular performance was only studied in one direction by moving the light source unidirectional. The result shows a non-uniformity illumination distribution at the exit aperture. Another study conducted by Baig et al. (Baig, Sellami and Mallick, 2015) has presented the losses incur in a 3D Cross Compound Parabolic Concentrator (3DCCPC). An optical analysis is conducted by quantifying the losses due to the encapsulant spillage of different thickness. However in their work, it is more focused on the losses caused by the optical adhesive and the concept of trapping the light escaping from the module. Other than the edge/ corner light leakage, the optical performance of a CCPC lens can be also affected by many other factors, such as Fresnel reflection losses caused by refractive-index difference as well as the absorption

of the materials, which in this work, a detailed analysis for all kind of possible optical losses will be computed. Through the breakdown analysis, it allows future researchers to understand what the possible optical losses are and how much it can affect the overall efficiencies of the CCPC lens. Understanding the optical losses of the optics is essential for the researchers to optimize their CPV system.

To validate the ray-tracing numerical simulation technique used, both indoor and outdoor experiments is conducted in this work. An indoor experiment is carried out with the aid of solar simulator to validate the simulated result. Gao and Chen used laser instrument to verify the light path generated through the ray tracing, and the difference between the theoretical and experimental result is analysed through the abscissa of a point. Similarly, their ray tracing method is also based on Monte Carlo Ray Trace (Gao and Chen, 2020). However, laser instrument can only emit single light ray at one time. It is effective to track the direction of the light ray but not able to observe the ray's convergence characteristics of the whole system. For this reason, solar simulator is used in this work as it can generate solar light rays with full range of solar spectrum, with the projection area that is able to cover the whole CCPC-CPV assembly module. In this case, the ray's convergence characteristics of the module can be studied thoroughly as the light rays will distribute onto every part of the module's entrance.

CHAPTER 3

METHODOLOGY

3.1 Overview of UHCPV system

Wong et al. introduced an UHCPV system with the integration of two non-imaging optics as solar concentrators. The proposed solar concentrator system is a combination of non-imaging dish concentrator (NIDC) and dielectric-filled crossed compound parabolic concentrator (CCPC). The 3-dimensional schematic diagram of the UHCPV system is shown in Figure 3.1 (Wong *et al.*, 2017).

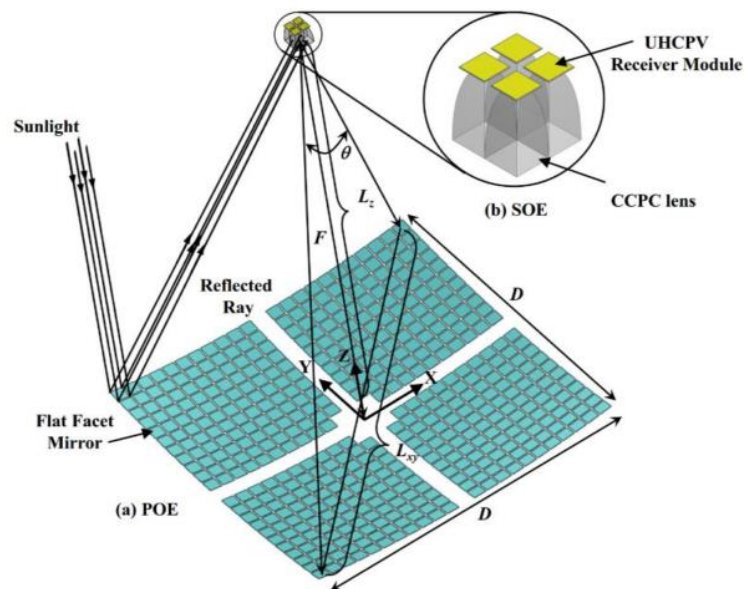


Figure 3.1: The UHCPV system comprises of (a) POE: non-imaging dish concentrator (b) SOE: crossed compound parabolic concentrator (Wong *et al.*, 2017).

The incoming solar irradiance from the sun will be collected by the POE and reflected towards the SOE. Next, the irradiance will be homogenized and further concentrated by the SOE before entering the solar cell.

3.1.1 Design of primary optical element

The primary optical element used in this UHCPV system is non-imaging dish concentrator. This design is aimed to generate uniform flux distribution across the receiver. The design criteria and details of the non-imaging dish concentrator are patented by Chong et al. (Chong *et al.*, 2012, 2013; Chong, Yew and Tan, 2015). A parabolic dish made of single piece of mirror requires high manufacturing cost because distinct technology is needed to fabricate the mirror with thickness from 0.7 mm to 1.0 mm to shape it in parabolic mirror (Kussul *et al.*, 2008). Therefore, the cost for a combination of small facet mirrors can be really low and the manufacturing process is easier compared to a whole piece of parabolic mirror.

As shown in Figure 3.1(a), the NIDC is formed by 480 pieces identical facet mirrors arranged in an array of 22 rows \times 22 columns. To avoid the shading of the central receiver, four mirrors around the origin is removed. The dimension of each flat facet mirrors is 4 cm \times 4 cm. The position of the facet mirrors is gradually lifted from central to peripheral regions to form a parabolic dish. In addition, the facet mirrors is drawn 0.5 cm adjacent to each other to enable more tolerance for installation. The position of each facet mirrors is arranged through a computational algorithm so that it won't block and causes

shadowing effect among the adjacent mirrors. The specification of the NIDC is listed in Table 3.1.

Table 3.1 Specifications of the NIDC as the primary concentrator of the UHCPV system.

<i>Primary optical element (POE) : Non-imaging dish concentrator (NIDC)</i>	
Type of reflector	Flat facet mirrors
Dimension of facet mirrors	4 cm × 4 cm
Total reflective area	7680 cm ²
Total projection area of reflector	7590 cm ²
Assumed reflectivity in simulation	0.95
Array arrangement	11 rows × 11 column per quarters 22 rows × 22 columns in total, with 4 facet mirrors in central region removed

3.1.2 Overview of CCPC-CPV assembly module

Crossed compound parabolic concentrator is utilized as secondary concentrator in the UHCPV system. Figure 3.2(a)-(b) depict the cross-sectional view of the CCPC lens and 3-D geometry of assembly CCPC-CPV module being studied in this paper. A CCPC-CPV assembly module means the integration of a CCPC lens with a MJSC. The optical adhesive is used as the bonding material between the CCPC lens and a MJSC module equipped with a bypass diode. Most of the solar cells in the market including Azur Space 3C44 MJSC (used in this study) are fabricated in a square or rectangular shape. To match the interface of MJSC, the lens aperture must be designed in square with the size

slightly smaller than that of solar cell to avoid the concentrated sunlight fallen onto the peripheral region of the solar cell which is non-active due to the built-in bus bars (T. Yew, Chong and Lim, 2015). The specification of the CCPC lens is listed in Table 3.2 and the detailed design rule of the CCPC lens used in this work has been described in a previous work done by Yew et al. (T. Yew, Chong and Lim, 2015). The geometrical concentration ratio (GCR) of a concentrating optic can vary. For instances, when the irradiances that falls on 10 cm^2 is concentrated onto a surface of 1 cm^2 , the GCR is said to be 10 suns; if the light of 100 cm^2 is concentrated on 1 cm^2 , then the GCR is 100 suns. The GCR of CCPC lens is 5.998 as the entrance aperture is 576 mm^2 while the exit aperture is 96.04 mm^2 . In this study, B270 Schott glass is chosen as the dielectric material for the CCPC lens due to its high transmissivity and affordable cost.

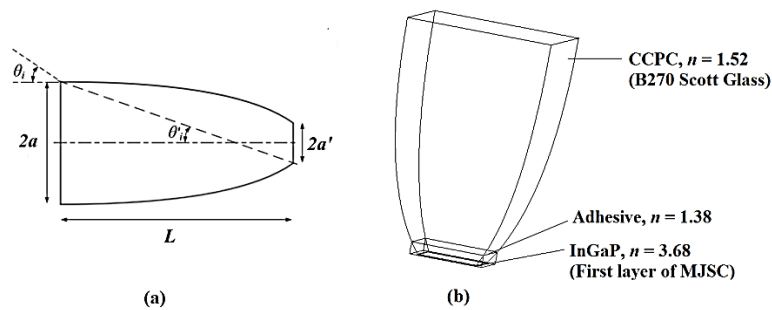


Figure 3.2: (a) Cross sectional view of the dielectric-filled CCPC lens (b) 3-D geometry of an assembly CCPC-CPV module with refractive indices, n , of each component.

By referring to Figure 3.2(a), the geometrical design of the CCPC lens can be calculated through the following equations derived from Snell's Law (Winston, Miñano and Benitez, 2005).

$$2a = \frac{2a'}{\sin \theta'_i} \quad (3.1)$$

$$L = \frac{a'(1 + \sin \theta'_i) \cos \theta'_i}{\sin^2 \theta'_i} \quad (3.2)$$

$$\theta_i = \sin^{-1}(n \sin \theta'_i) \quad (3.3)$$

$$GCR = \left(\frac{a}{a'}\right)^2 = \left(\frac{1}{\sin \theta'_i}\right)^2 = \left(\frac{n}{\sin \theta_i}\right)^2 \quad (3.4)$$

where $2a$ and $2a'$ represent the entrance and exit aperture size respectively while L is the length of the CCPC lens. The half acceptance angle, θ'_i and the angular half acceptance angle, θ_i of the CCPC lens can be computed through Eqns. 3.3 and 3.4 as 24.1° and 37.77° respectively.

Table 3.2 Specification of the secondary optics element used in UHCPV system.

Secondary optical element (SOE): Crossed compound parabolic concentrator (CCPC) lens

Dielectric material	B270 Schott glass
Array arrangement	2 rows \times 2 columns
Dimension of the entrance aperture, $2a$	24 mm \times 24 mm
Dimension of the exit aperture, $2a'$	9.8 mm \times 9.8 mm
Length, L	37.78 mm
Geometrical concentration ratio (GCR)	5.998
Half acceptance angle, $\theta'i$	24.1°
Angular half acceptance angle, θi	37.77°

Optical constant of B270 Schott Glass @ 300-1800nm

Refractive index, n	1.50 – 1.56
Absorption coefficient, α	$2.81 \times 10^{-04} \text{ mm}^{-1} - 0.14 \text{ mm}^{-1}$
Extinction coefficient, k	$1.23 \times 10^{-08} - 3.59 \times 10^{-06}$
Internal transmittance, Ti	0 – 0.989
External transmittance, Te	0 – 0.906

3.1.3 Multi-junction solar cell

The internal structure of a MJSC studied in this work is divided into three layers, Indium Gallium Phosphide (InGaP) on top, followed by Indium Gallium Arsenide (InGaAs) and lastly Germanium (Ge) as shown in Figure 3.3 while the external quantum efficiency (EQE) of the three p-n junctions is shown in Figure 3.4 (Azur Space, 2015) which provides energy conversion efficiency as the ratio of the output electrical energy to incident photonic energy for each wavelength.

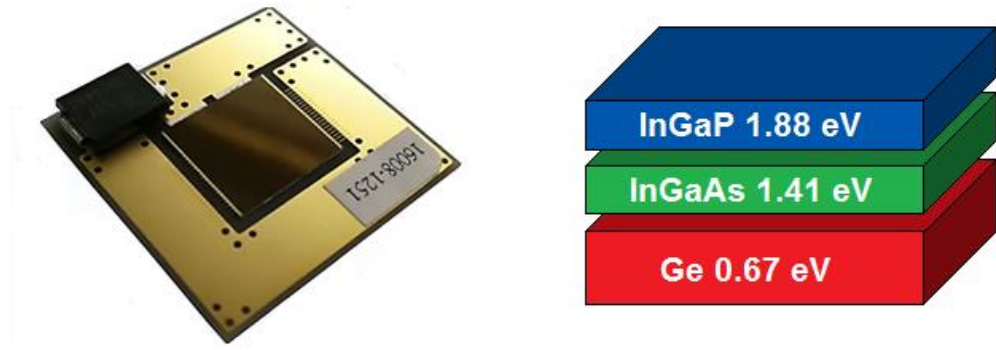


Figure 3.3: Azur Space 3C44 consisting of three layers: InGaP/InGaAs/Ge with a bandgap of 1.88 eV, 1.41 eV and 0.67 eV respectively.

Each MJSC equipped with a bypass diode for protecting purpose. As a matter of facts, there are two options of ARCs for the MJSC depending on user's need, which is ARC-air and ARC-glass. ARC-air indicates that the antireflective coating applied on the surface of MJSC is adjusted for the interface to air. Under this circumstance, the light rays enter the MJSC directly from air. On the other hand, the ARC-glass is adapted for the interface to glass or other similar materials with refractive index, $n \approx 1.43$. It is suitable for the application where the light will enter the MJSC through secondary glass components or homogenizer. With regards to this, ARC-glass is applied in this work since the CCPC lens is bonded onto MJSC. The specification of the MJSC is listed in Table 3.3. The detailed electrical and mechanical data of the MJSC can be found in Appendix B.

Table 3.3 Specification of the multi-junction solar cell (MJSC) used in this work (Azur Space, 2015).

Multi junction solar cell: Azur Space 3C44

Base materials	First layer – Indium Gallium Phosphide Second layer – Indium Gallium Arsenide Third layer – Germanium
Dimension of active cell	10 mm × 10 mm
Thickness	190 μm (± 20 μm)
Antireflective coating material	TiO _x /AlO _x
Typical efficiency at 1000 suns	40.5%
Maximum operating temperature	110 °C

Measurement condition:

1000 W/m² irradiance (ASTM G 173-03), Temperature = 25 °C

Open circuit voltage, V_{OC} @ 1000 suns	3.14 V
Short circuit current, I_{SC} @ 1000 suns	14.97 A

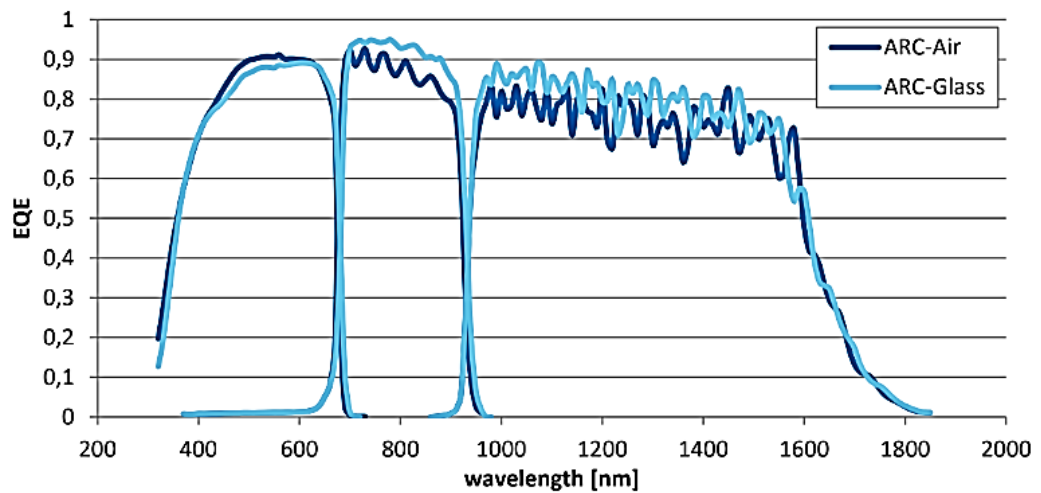


Figure 3.4: External quantum efficiency (EQE) of the MJSC (Azur Space, 2015).

Since each p-n junction material responds to a different range of the solar spectral irradiance in such a way that the three different III-V semiconductor materials can complement each other to cover almost the full solar spectrum. Moreover, the MJSC is designed to generate high density of electrical power capable of accommodating high current and high operating temperature under highly concentrated sunlight as compared to that of the conventional silicon solar cells.

3.2 Performance evaluation of CCPC-CPV assembly module

The evaluation of CCPC-CPV assembly module in both optical and electrical performance has been carried out through computational and experimental methods. The research methodology of theoretical modelling on CCPC-CPV assembly module with practical validation is presented systematically in a flow chart as depicted in Figure 3.5.

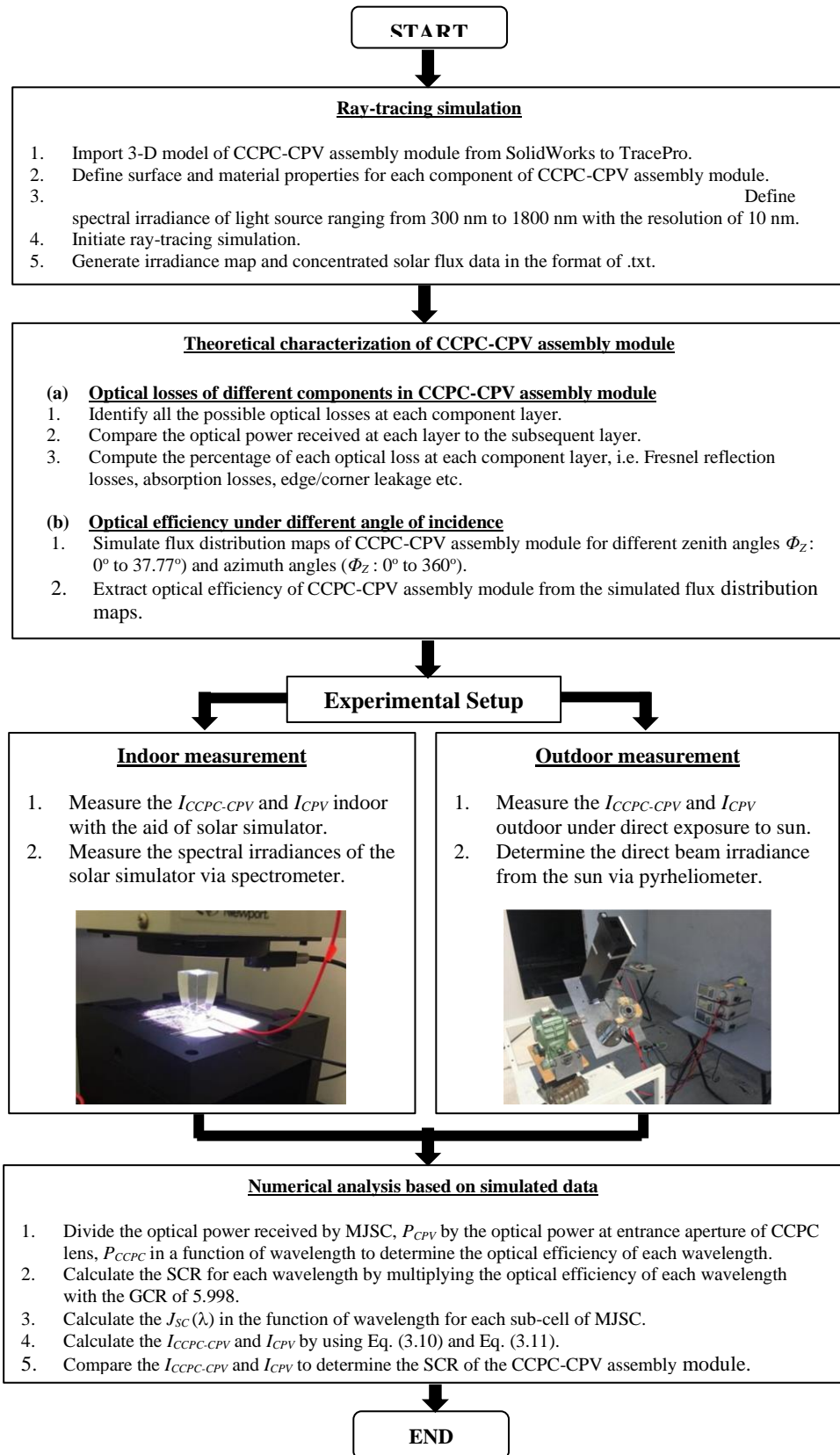


Figure 3.5: A summary of the evaluation process of the CCPC-CPV assembly module.

3.2.1 Ray tracing simulation

Ray tracing is a simulation technique that is extensively used in optical science and engineering. It has long been used for studying the realistic lightning and application's performance as it can simulate the physical behaviour of the light through various mediums. An optical system can be optimized with the help of ray tracing as researchers are able to diagnostic and analyse the performance through illustrating the distribution of lights. Many researchers rely on ray tracing simulation to evaluate the solar and optical system in their studies (G. L. Dai *et al.*, 2011; Zheng *et al.*, 2014; Baig, Sellami and Mallick, 2015; T. K. Yew, Chong and Lim, 2015). Aiming to develop a ray tracing numerical technique to investigate the characteristics of the CCPC module, the optical engineering software – TracePro is used in this work. TracePro comes with a user-friendly, CAD-like interface that uses Monte Carlo ray tracing to accurately predict the performance of the prototype.

Firstly, a 3-D model was created using 3-D CAD software called SolidWorks as shown in Figure 3.6. The modelling of the CCPC-CPV assembly module comprises of CCPC lens, a layer of optical adhesive as well as the MJSC. The adhesive is extruded up to the body of the CCPC lens to create a lap of spillage surrounding the bottom of the lens as in actual assembly.

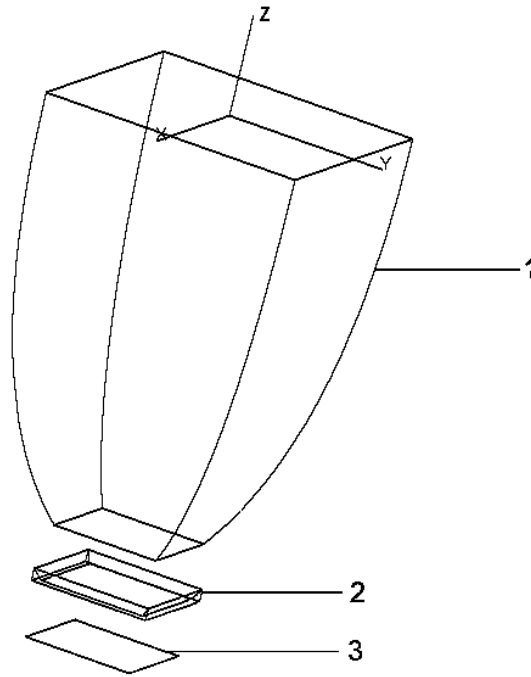


Figure 3.6: 3-D modelling of the CCPC-CPV assembly module (1) CCPC lens, (2) optical adhesive, (3) MJSC.

The assembly drawing is exported as .stp file and imported into TracePro as .oml file for 3-D ray trace. The surface and material properties data for each part of the assembly are defined accordingly. A bilayer of anti-reflective coating comprised of TiO_2 and SiO_2 is applied on top of the MJSC as stated in the datasheet. Lastly, the light source's spectrums were added from 300 nm to 1800 nm (with 10 nm wavelength interval).

The objective for this work is to identify the optical losses of the CCPC module. For a comprehensive assessment on the optical system, all the possible optical losses occurred at each stage of the light transmission in the CCPC-CPV assembly module during the operation are listed out in the theoretical analyses, which include Fresnel reflection loss, absorption loss, edge/corner

leakage and losses caused by the adhesive spillage. The refractive indices, n , of all the elements in the CCPC-CPV assembly module are shown in Table 3.4. Any discontinuity of refractive index happened at the interface of two materials can result in Fresnel reflection loss in which there are several elements with significant variations in reflective indices (Sankawa *et al.*, 1986).

Table 3.4 Refractive indices, n of the components used in the CCPC-CPV assembly module.

Components	Refractive index, n @ 300-1800 nm
CCPC lens	1.50 – 1.56
Optical adhesive	1.39 – 1.37
MJSC (InGaP)	3.11 – 3.70

In addition, a bilayer of anti-reflective coating (ARC) is applied on top of the surface of MJSC to minimize the effect of refractive index gap in order to reduce Fresnel reflection loss. During the ray-tracing simulation, defining appropriate values for the properties of all the elements of the CCPC-CPV assembly module are critical to ensure the accuracy of simulated results. The properties data that is required in the ray tracing simulation including the refractive index, absorption as well as extinction coefficient of all the components. Although most of the material properties are available in the built-in library database of TracePro, but some of the information such as absorption coefficient, α and extinction coefficient, k are incomplete. As a result, the properties data of Schott B270 Glass was extracted directly from the datasheet provided by the manufacturer and inserted the data into the TracePro

property database (Schott Corp., 1993). The following equation is the index dispersion formula for B270 Schott glass:

$$n_{B270}^2(\lambda) = a_1 + a_2\lambda^2 + \frac{a_3}{\lambda^2} + \frac{a_4}{\lambda^4} + \frac{a_5}{\lambda^6} + \frac{a_6}{\lambda^8} \quad (3.5)$$

where n_{B270} represents the refractive indices of B270 Schott Glass with respect to the wavelength of light source. The value for the index coefficient, a are listed below in Table 3.5 whereas the complete properties data for B270 Schott glass are stated in Table 3.6.

Table 3.5: Index coefficient for the dispersion formula of B270 Schott glass.

Index Coefficient	Index
a ₁	2.286575
a ₂	-0.0087334582
a ₃	0.011742884
a ₄	0.00029041756
a ₅	$-1.2506695 \times 10^{-5}$
a ₆	9.2646253×10^{-7}

Figure 3.7 shows the variation of extinction coefficient, k and refractive index, n of B270 Schott Glass throughout the broadband of solar spectrum.

Table 3.6: The refractive indices, absorption and extinction coefficient of B270

Schott glass for wavelength 300 nm to 1800 nm.

Wavelength (nm)	Refractive index, n	Absorption (/mm)	Extinction Coefficient, k ($\mu\text{m}/\mu\text{m}$)
300	1.57	1	2.38732 E-05
310	1.56	1	2.46690 E-05
320	1.56	1.41341 E-01	3.59924 E-06
330	1.55	6.43357 E-02	1.68949 E-06
340	1.55	2.80822 E-02	7.59804 E-07
350	1.55	1.28110 E-02	3.56816 E-07
360	1.55	6.14309 E-03	1.75987 E-07
370	1.54	4.08677 E-03	1.20330 E-07
380	1.54	4.38241 E-03	1.32522 E-07
390	1.54	1.93003 E-03	5.98989E-08
400	1.54	1.25624 E-03	3.99876 E-08
410	1.54	1.10743 E-03	3.61321 E-08
420	1.54	1.18179 E-03	3.94988 E-08
430	1.54	1.33077 E-03	4.55369 E-08
440	1.53	1.39578 E-03	4.88723 E-08
450	1.53	1.24697 E-03	4.46542 E-08
460	1.53	1.02438 E-03	3.74983 E-08
470	1.53	8.02533 E-04	3.00159 E-08
480	1.53	6.55040 E-04	2.50207 E-08
490	1.53	4.34411 E-04	1.69390 E-08
500	1.53	3.61030 E-04	1.43649 E-08
510	1.53	5.00427 E-04	2.03096 E-08
520	1.53	3.53907 E-04	1.46448 E-08
530	1.53	2.80768 E-04	1.18417 E-08
540	1.53	2.80768 E-04	1.20651 E-08
550	1.53	2.80768 E-04	1.22885 E-08
560	1.52	2.80768 E-04	1.25120 E-08
570	1.52	2.80768 E-04	1.27354 E-08
580	1.52	3.53907 E-04	1.63346 E-08
590	1.52	4.27127 E-04	2.00539 E-08
600	1.52	5.00427 E-04	2.38937 E-08
610	1.52	5.00427 E-04	2.42919 E-08
620	1.52	5.73808 E-04	2.83106 E-08
630	1.52	6.47270 E-04	3.24501 E-08
640	1.52	7.20813 E-04	3.67107 E-08
650	1.52	7.20813 E-04	3.72844 E-08
660	1.52	6.47270 E-04	3.39954 E-08
670	1.52	6.47270 E-04	3.45105 E-08
680	1.52	6.47270 E-04	3.50256 E-08
690	1.52	7.13060 E-04	3.91531 E-08
700	1.52	7.13060E-04	3.97205 E-08
710	1.52	7.13060 E-04	4.02879 E-08
720	1.52	7.13060 E-04	4.08554 E-08

730	1.52	7.13060 E-04	4.14228 E-08
740	1.52	7.13060 E-04	4.19902 E-08
750	1.52	7.13060 E-04	4.25577 E-08
760	1.52	7.13060 E-04	4.31251 E-08
770	1.52	7.13060 E-04	4.36925 E-08
780	1.52	7.86522 E-04	4.88198 E-08
790	1.52	7.86522 E-04	4.94457 E-08
800	1.52	8.60065 E-04	5.47535 E-08
810	1.52	8.60065 E-04	5.54379 E-08
820	1.52	8.60065 E-04	5.61223 E-08
830	1.52	8.60065 E-04	5.68067 E-08
840	1.52	8.60065 E-04	5.74911 E-08
850	1.52	8.60065 E-04	5.81756 E-08
860	1.52	7.86522 E-04	5.38269 E-08
870	1.52	7.86522 E-04	5.44528 E-08
880	1.52	7.86522 E-04	5.50787 E-08
890	1.52	7.86522 E-04	5.57046 E-08
900	1.52	7.86522 E-04	5.63305 E-08
910	1.52	7.86522 E-04	5.69564 E-08
920	1.51	7.86522 E-04	5.75823 E-08
930	1.51	7.86522 E-04	5.82082 E-08
940	1.51	8.60065 E-04	6.43353 E-08
950	1.51	8.60065 E-04	6.50197 E-08
960	1.51	8.60065 E-04	6.57042 E-08
970	1.51	8.60065 E-04	6.63886 E-08
980	1.51	8.60065 E-04	6.70730 E-08
990	1.51	8.60065 E-04	6.77574 E-08
1000	1.51	8.60065 E-04	6.84418 E-08
1010	1.51	9.33689 E-04	7.50437 E-08
1020	1.51	8.60065 E-04	6.98107 E-08
1030	1.51	9.33689 E-04	7.65297 E-08
1040	1.51	9.33689 E-04	7.72727 E-08
1050	1.51	9.33689 E-04	7.80157 E-08
1060	1.51	9.33689 E-04	7.87587 E-08
1070	1.51	9.33689 E-04	7.95017 E-08
1080	1.51	9.33689 E-04	8.02447 E-08
1090	1.51	9.33689 E-04	8.09877 E-08
1100	1.51	1.00739 E-03	8.81826 E-08
1110	1.51	9.33689 E-04	8.24737 E-08
1120	1.51	9.33689 E-04	8.32167 E-08
1130	1.51	9.33689 E-04	8.39597 E-08
1140	1.51	1.07280 E-03	9.73223 E-08
1150	1.51	1.07280 E-03	9.81760 E-08
1160	1.51	1.07280 E-03	9.90297 E-08
1170	1.51	1.07280 E-03	9.98834 E-08
1180	1.51	1.07280 E-03	1.00737 E-07
1190	1.51	1.07280 E-03	1.01591 E-07
1200	1.51	9.99171 E-04	9.54139 E-08
1210	1.51	9.99171 E-04	9.62090 E-08
1220	1.51	9.99171 E-04	9.70041 E-08

1230	1.51	9.99171 E-04	9.77992 E-08
1240	1.51	9.99171 E-04	9.85943 E-08
1250	1.51	9.99171 E-04	9.93895 E-08
1260	1.51	9.99171 E-04	1.00185 E-07
1270	1.51	9.99171 E-04	1.00980 E-07
1280	1.51	9.99171 E-04	1.01775 E-07
1290	1.51	9.99171 E-04	1.02570 E-07
1300	1.51	9.99171 E-04	1.03365 E-07
1310	1.51	9.99171 E-04	1.04160 E-07
1320	1.51	9.25628 E-04	9.72301 E-08
1330	1.51	9.25628 E-04	9.79667 E-08
1340	1.51	9.25628 E-04	9.87033 E-08
1350	1.51	9.25628 E-04	9.94399 E-08
1360	1.51	9.25628 E-04	1.00177 E-07
1370	1.51	9.25628 E-04	1.00913 E-07
1380	1.51	9.99171 E-04	1.09726 E-07
1390	1.51	1.14650 E-03	1.26818 E-07
1400	1.51	1.51626 E-03	1.68924 E-07
1410	1.51	1.59045 E-03	1.78456 E-07
1420	1.51	1.59045 E-03	1.79721 E-07
1430	1.51	1.51626 E-03	1.72544 E-07
1440	1.51	1.29416 E-03	1.48300 E-07
1450	1.51	1.22029 E-03	1.40806 E-07
1460	1.51	1.07280 E-03	1.24641 E-07
1470	1.51	1.07280 E-03	1.25494 E-07
1480	1.51	9.99171 E-04	1.17677 E-07
1490	1.51	9.99171 E-04	1.18472 E-07
1500	1.51	1.07280 E-03	1.28056 E-07
1510	1.51	1.07280 E-03	1.28909 E-07
1520	1.51	1.07280 E-03	1.29763 E-07
1530	1.51	1.07280 E-03	1.30617 E-07
1540	1.51	1.07280 E-03	1.31470 E-07
1550	1.51	1.07280 E-03	1.32324 E-07
1560	1.51	1.07280 E-03	1.33178 E-07
1570	1.51	1.07280 E-03	1.34032 E-07
1580	1.51	1.07280 E-03	1.34885 E-07
1590	1.51	1.22029 E-03	1.54401 E-07
1600	1.51	1.29416 E-03	1.64777 E-07
1610	1.51	1.29416 E-03	1.65807 E-07
1620	1.51	1.36811 E-03	1.76370 E-07
1630	1.51	1.36811 E-03	1.77459 E-07
1640	1.51	1.51626 E-03	1.97882 E-07
1650	1.51	1.59045 E-03	2.08831 E-07
1660	1.51	1.59045 E-03	2.10097 E-07
1670	1.51	1.81354 E-03	2.41010 E-07
1680	1.51	1.81354 E-03	2.42453 E-07
1690	1.51	1.88807 E-03	2.53919 E-07
1700	1.51	2.11216 E-03	2.85737 E-07
1710	1.51	2.26198 E-03	3.07804 E-07
1720	1.51	2.26198 E-03	3.09604 E-07

1730	1.51	2.41213 E-03	3.32075 E-07
1740	1.51	2.56262 E-03	3.54832 E-07
1750	1.51	2.78899 E-03	3.88396 E-07
1760	1.50	3.01613 E-03	4.22429 E-07
1770	1.50	3.09202 E-03	4.35518 E-07
1780	1.50	3.39643 E-03	4.81098 E-07
1790	1.50	3.54916 E-03	5.05556 E-07
1800	1.50	3.70224 E-03	5.30308 E-07

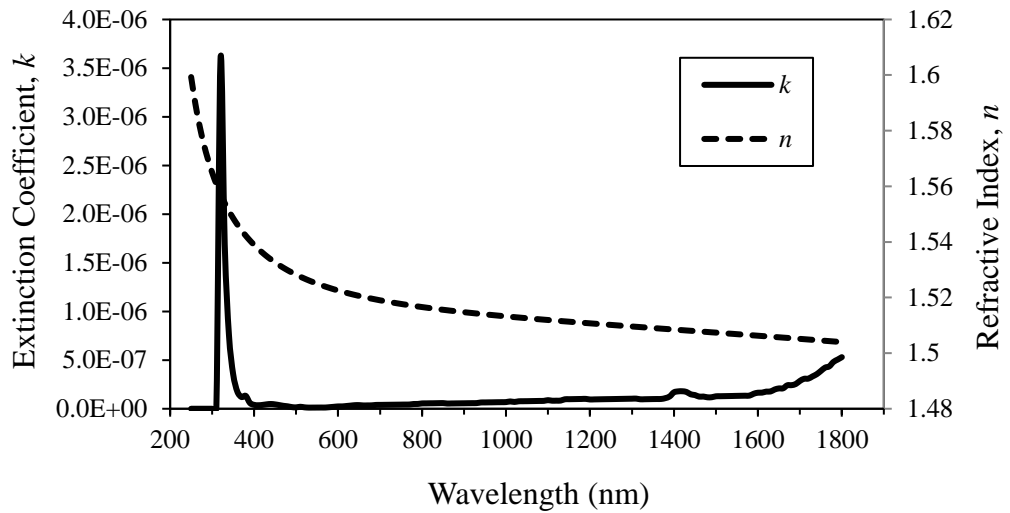


Figure 3.7: Extinction coefficient, k and refractive index, n of B270 Schott glass throughout the wide range of solar spectrum.

For the theoretical analyses of CCPC-CPV assembly module under real climate condition by taking into the consideration of the actual solar spectrum, the simulated light source is set from 300 nm to 1800 nm in TracePro, where fits well with the spectral response of MJSC. The use of full range of wavelengths for the solar spectrum is absolutely necessary in the ray-tracing simulation as each wavelength reacts differently to different materials in which refractive index varies with wavelength. To highlight the importance of setting a full wavelength of solar spectrum in the theoretical analysis, a ray-tracing

simulation using single wavelength of 550 nm has also been conducted for a comparison.

To bond the CCPC lens onto the MJSC, optical adhesive with high transmittance is employed. Baig et al. (Baig, Sellami and Mallick, 2015) posited that the encapsulated spillage surrounding the bottom side of the lens can lead to light leakage from the edge of the optical element in which the thickness of adhesive spillage plays a vital role in justifying the losses. In the current stage of this research, it is impossible to eliminate the spillage of optical adhesive completely. Hence, a layer of optical adhesive is needed to be included in the simulation as shown in Figure 3.8. The thickness of the adhesive spillage surrounding the bottom edge of CCPC lens, t_{al} is the key parameter to affect the optical losses. In this simulation, the performance of the CCPC-CPV assembly module has been tested with the thickness of the optical adhesive adjusted to 1 mm, 2 mm, 3 mm and 4 mm. With the light source placed normal to the entrance aperture of the CCPC lens, tens of thousands of light rays are traced through the total internal reflection, refraction and scattering phenomena inside the lens during the simulation.

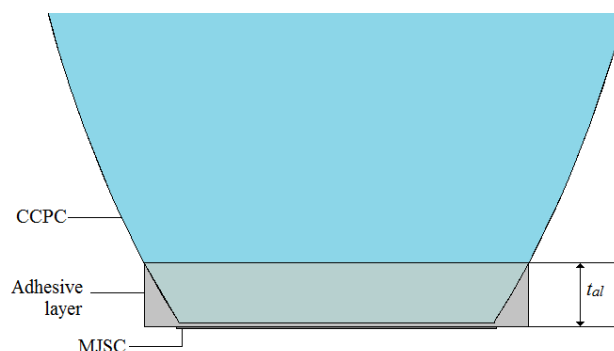


Figure 3.8: The optical adhesive layer is inserted into the model for theoretical simulation.

3.2.2 Simulation for different angle of incidence.

The optical characteristic of the CCPC-CPV module is also studied in omnidirectional. The angle of incidence is an important input to model CPV systems and the parameters used to describe the sun position relative to the CPV system usually divided into two parts: zenith angle and azimuth angle. The light source has been placed in different angles of incidence angle relative the entrance aperture of the CCPC-CPV module. From Figure 3.9, the Zenith angle, Φ_Z is the angle between the Z-axis and the incident ray while Azimuth angle, Φ_A is the angle between Y-axis and projection of incident ray with positive direction starting from the front view of the module in counter clockwise. As the half acceptance angle of the CCPC lens is 37.77° , the range of the zenith angle used in the ray-tracing simulation is from 0° to 37.77° while the range of azimuth angle used in the ray-trace simulation is from 0° to 360° .

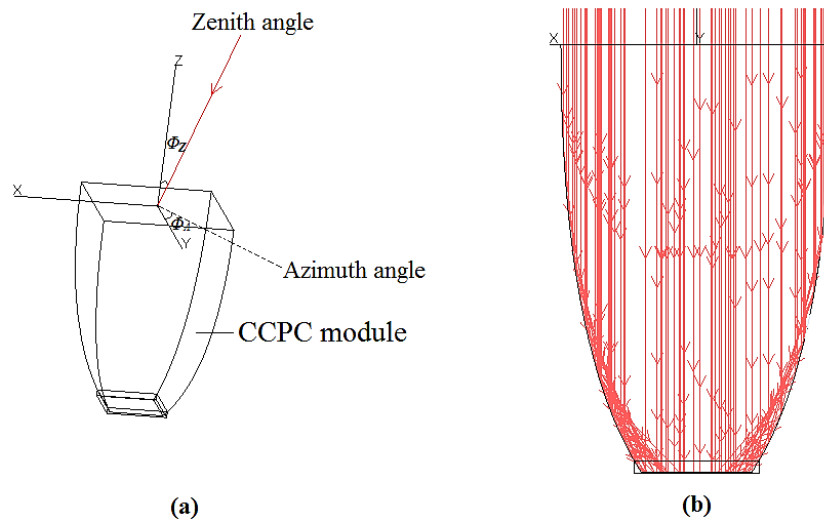


Figure 3.9: (a) Definition of angles of incidences (Zenith angle, Φ_Z and Azimuth angle, Φ_A) of the light source relative to the CCPC lens during the simulation. (b) Light rays hitting on the CCPC lens' inner wall are mostly reflected onto the peripheral region of the CPV cell via total internal reflection.

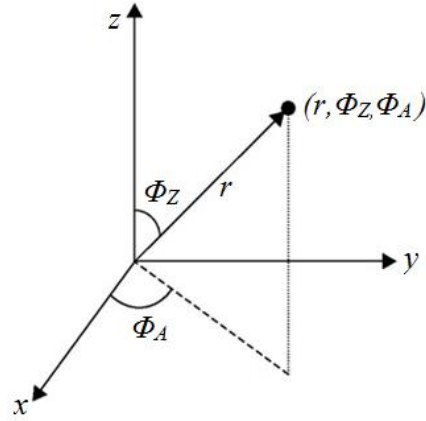


Figure 3.10: Spherical coordinate is used to calculate the position of light source under different angle of incidence.

From Figure 3.10, the position of light source for different angle of incidence can be calculated through the following equation:

$$X = r \sin \Phi_Z \cos \Phi_A \quad (3.6)$$

$$Y = r \sin \Phi_Z \sin \Phi_A \quad (3.7)$$

$$Z = r \cos \Phi_Z \quad (3.8)$$

where r represents the radial distance from the origin (central of CCPC lens' entrance aperture) to the central of the light source. In this work, r is set as 120 mm. The position of the light source varies with the angle of incidence are listed in Table 3.7 and Table 3.8.

Table 3.7: Light source position (X, Y) for zenith angle equal to 0° , 10° and 20° respectively.

Φ_A	Φ_Z		
	$0^\circ, Z = 120 \text{ mm}$	$10^\circ, Z = 118.17 \text{ mm}$	$20^\circ, Z = 112.76 \text{ mm}$
0°	(0 , 0)	(20.8374 , 0)	(41.0423 , 0)
15°	(0 , 0)	(20.1274 , 5.3931)	(39.6439 , 10.6225)
30°	(0 , 0)	(18.0457 , 10.4187)	(35.5437 , 20.5211)
45°	(0 , 0)	(14.7342 , 14.7343)	(29.0213 , 29.0213)
60°	(0 , 0)	(10.4187 , 18.0457)	(20.5212 , 35.5437)
75°	(0 , 0)	(5.3931 , 20.1274)	(10.6226 , 39.6439)
90°	(0 , 0)	(0 , 20.8374)	(0 , 41.0423)
105°	(0 , 0)	(-5.3931 , 20.1274)	(-10.6226 , 39.6439)
120°	(0 , 0)	(-10.4187 , 18.0457)	(-20.5212 , 35.5437)
135°	(0 , 0)	(-14.7342 , 14.7343)	(-29.0213 , 29.0213)
150°	(0 , 0)	(-18.0457 , 10.4187)	(-35.5437 , 20.5211)
165°	(0 , 0)	(-20.1274 , 5.3931)	(-39.6439 , 10.6225)
180°	(0 , 0)	(-20.8374 , 0)	(-41.0423 , 0)
195°	(0 , 0)	(-20.1274 , -5.3931)	(-39.6439 , -10.6225)
210°	(0 , 0)	(-18.0457 , -10.4187)	(-35.5437 , -20.5211)
225°	(0 , 0)	(-14.7342 , -14.7343)	(-29.0213 , -29.0213)
240°	(0 , 0)	(-10.4186 , -18.0457)	(-20.5212 , -35.5437)
255°	(0 , 0)	(-5.3931 , -20.1274)	(-10.6226 , -39.6439)
270°	(0 , 0)	(0 , -20.8374)	(0 , -41.0423)
285°	(0 , 0)	(5.3931 , -20.1274)	(10.6226 , -39.6439)
300°	(0 , 0)	(10.4186 , -18.0457)	(20.5212 , -35.5437)
315°	(0 , 0)	(14.7342 , -14.7343)	(29.0213 , -29.0213)
330°	(0 , 0)	(18.0457 , -10.4187)	(35.5437 , -20.5211)
345°	(0 , 0)	(20.1274 , -5.3931)	(39.6439 , -10.6225)

Table 3.8: Light source position (X, Y) for zenith angle equal to 30° and 37.77° (acceptance angle of CCPC lens) respectively.

Φ_A	Φ_Z	
	$30^\circ, Z = 103.92 \text{ mm}$	$37.77^\circ, Z = 94.85 \text{ mm}$
0°	(60 , 0)	(73.4991 , 0)
15°	(57.9556 , 15.5292)	(70.9947 , 19.023)
30°	(51.9615 , 30)	(63.6521 , 36.7495)
45°	(42.4264 , 42.4263)	(51.9718 , 51.9717)
60°	(30 , 51.9614)	(36.7496 , 63.652)
75°	(15.5292 , 57.9554)	(19.0231 , 70.9947)
90°	(0 , 60)	(0 , 73.4991)
105°	(-15.5290 , 57.9555)	(-19.0229 , 70.9947)
120°	(-30 , 51.9615)	(-36.7496 , 63.652)
135°	(-42.4263 , 42.4264)	(-51.9718 , 51.9717)
150°	(-51.9615 , 30)	(-63.6521 , 36.7495)
165°	(-57.9555 , 15.5293)	(-70.9947 , 19.023)
180°	(-60 , 0)	(-73.4991 , 0)
195°	(-57.9555 , -15.5293)	(-70.9947 , -19.023)
210°	(-51.9615 , -30)	(-63.6521 , -36.7495)
225°	(-42.4263 , -42.4264)	(-51.9718 , -51.9717)
240°	(-30 , -51.9615)	(-36.7496 , -63.652)
255°	(-15.5290 , -57.9555)	(-19.0229 , -70.9947)
270°	(0 , -60)	(0 , -73.4991)
285°	(15.5290 , -57.9555)	(19.0229 , -70.9947)
300°	(30 , -51.9615)	(36.7496 , -63.652)
315°	(42.4263 , -42.4264)	(51.9718 , -51.9717)
330°	(51.9615 , -30)	(63.6521 , -36.7495)
345°	(57.9555 , -15.5293)	(70.9947 , -19.023)

3.2.3 Performance evaluation of the UHCPV System

This research establishes a detailed study on the characteristics and performance of the CCPC lens for solar application in real working condition.

Apart from the performance of the lens, a simulation of the whole UHCPV system is also carried out by integrating the CCPC module with the POE

(NIDC) where 480 pieces of facet mirrors formed a reflective area in the primary stage. A minor gap of 50 mm is adjusted between the facets mirrors to provide tolerance for the installation in actual assembly (Wong *et al.*, 2017). Incoming light rays are collected and reflected from NIDC onto the 2×2 array CCPC modules for further concentration before entering the MJCS. The surface properties of the facet mirrors are set as standard mirror with reflectivity of 0.95. The overall SCR for the whole UHCPV system is obtained through the simulation, and it will be discussed in the Chapter 4.

3.3 Numerical analysis

For the verification of theoretical result, the spectral irradiance of the solar simulator is measured via AVANTES spectrometer during indoor measurement. The measured spectral irradiance is then applied in the following numerical analysis. Firstly, the optical efficiency of each wavelength is computed by comparing between the optical power received by CPV cell (P_{CPV}) and the optical power arrived at entrance aperture of CCPC lens (P_{CCPC}) as shown in the following equation:

$$\eta_{optical}(\lambda) = \frac{P_{CPV}}{P_{CCPC}} \times 100\% \quad (3.9)$$

The optical efficiency in the function of wavelength, $\eta_{optical}(\lambda)$, are then multiplied with the GCR of CCPC lens (5.998 suns) and divided by 100% to obtain the spectral SCR, $C(\lambda)$, for each wavelength. The equation of the output current of CPV cell without CCPC lens, I_{CPV} was derived in the work presented by Lee *et al.* (Lee *et al.*, 2019) and can be simplified to

$$I_{CPV} = A_{active} \times \frac{q\lambda}{hc} \int \eta_{EQE}(\lambda) \cdot S_L(\lambda) d\lambda \quad (3.10)$$

where A_{active} is the active area of MJSC; q represents the electronic charge; c stands for the speed of light in vacuum; h is the Planck's constant; $\eta_{EQE}(\lambda)$ is the EQE of any p-n junction sub-cell in the MJSC, which is in a function of wavelength; $S_L(\lambda)$ is the spectral irradiance of light source (solar simulator or the sun).

Based on Eq. (3.11), we calculate the output current for all the three p-n junctions of sub-cells in the MJSC. Since three sub-cells are serial connected in the MJSC, the net output current of MJSC is capped by the lowest output current among the three sub-cells. The following is the equation for the output current of CCPC-CPV module:

$$I_{CCPC-CPV} = A_{active} \times \frac{q\lambda}{hc} \int C(\lambda) \cdot \eta_{EQE}(\lambda) \cdot S_L(\lambda) d\lambda \quad (3.11)$$

The SCR of the CCPC-CPV assembly module can be estimated through the following equations:

$$SCR = \frac{I_{CCPC-CPV}}{I_{CPV}} \quad (3.12)$$

3.4 Experimental setup

The simulation result has been validated with a series of indoor and outdoor experiments. The configurations of the experiments are discussed in the following section.

3.4.1 Assembling CCPC-CPV assembly module

A complete set of CCPC-CPV assembly module consists of MJSC and CCPC lens, one unit each. These two components must be bonded together so that it is easier for experiment setup as well as installation on the CPV system. To bond the components, Dow Corning SE 9120 RTV silicon is applied as the optical adhesive in between two components. This one-part RTV (Room temperature vulcanizing) based clear sealant makes the bonding process easier as it cures at room temperature of 25°C. Even though the Dow Corning SE 9120 RTV silicon is not tested for optical performance, its transparent and low viscosity nature makes it a suitable substance for optical bonding. Other than that, the robustness of this RTV silicon under concentrated sunlight has been tested in a previous work. As a result, no obvious degradation that could affect the output of the CPV cell negatively is observed (Yew, 2016).

After an adequate amount of optical adhesive is applied, the CCPC lens is placed on top of the MJSC with exit aperture facing downwards. As the optical adhesive takes time to cure, a jig is used to hold the CCPC lens in the same position throughout the curing process to maintain a 0.1 mm gap between two components, at the same time making sure that it will not force too much pressure on the adhesive to prevent excessive spillage. One crucial part about the assembling process is to ensure the bonding area is clear from air bubble as it will affect the refraction of light rays at the interface.

Next, to make it convenient for measurement, two external wires with low resistance and high current capacity were soldered to each terminal of the MJSC. Higher temperature around 400°C is required to solder on the DBC

substrate due to its high thermal conductivity and excellent heat dissipation. The CCPC lens is wrapped by a small piece of fabric to prevent the glass stained by the soldering fumes. Lastly, isopropyl alcohol is used to clean the modules. It is to remove the flux residues and fingerprints remained on the modules after soldering. The complete set of the CCPC-CPV assembly module is shown in Figure 3.11.

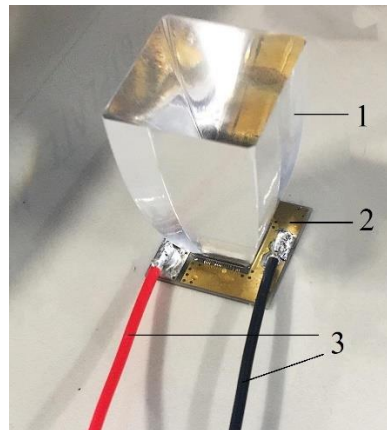


Figure 3.11: Complete set of CCPC-CPV assembly module (1) CCPC lens, (2) MJSC on DBC, (3) connecting wires.

3.4.2 Indoor measurement

An indoor experiment was conducted with the aid of the Oriel's Sol1A™ Class ABB solar simulator as shown in Figure 3.12. The solar simulator (model 94021A) is equipped with an 150W ozone-free xenon short arc lamp to illuminate the typical output power for 1 sun (1000 W/m^2). The three-alphabet code of the Class ABB solar simulator indicates the classification of spectral match, irradiance uniformity and temporal stability respectively. The criteria

for each of the parameter is explained in Table 3.9. The report and certifications for the criteria classification can be found in Appendix C.

Table 3.9: The classification criteria of the three parameters of the Oriel's Sol1A™ Class ABB solar simulator (Newport Corporation, 2011).

Parameters	Class Rating	Criteria
Spectral match	A	The spectral match of a solar simulator is determined according to the percentage of the integrated light intensity across six spectral ranges. The Class A rating in spectral match indicates that the solar simulator may not deviate more than 0.75 to 1.25 times the ideal percentage in each wavelength range.
Irradiance uniformity	B	The second alphabet indicates the irradiance uniformity of the light source over the working area. Hot spots can lead to significant deviation in measured cell efficiency and can cause inaccurate binning of cells. The Class B spatial uniformity performance standard is intended to minimize the impact of hot spots and meets the Class B requirements for the standards.
Temporal stability	B	To prevent the measured cell efficiency from interfered by the lamp fluctuations, the light source must be stable over time. This parameter meets Class B stability standards for all three standards without the need for a feedback-based controller.

To achieve the desired results in measuring stability, non-uniformity and spectral match, the lamp is turned on and allowed to warm up for 10

minutes before taking measurements. During the measurement, all lights is switched off except from the solar simulator.

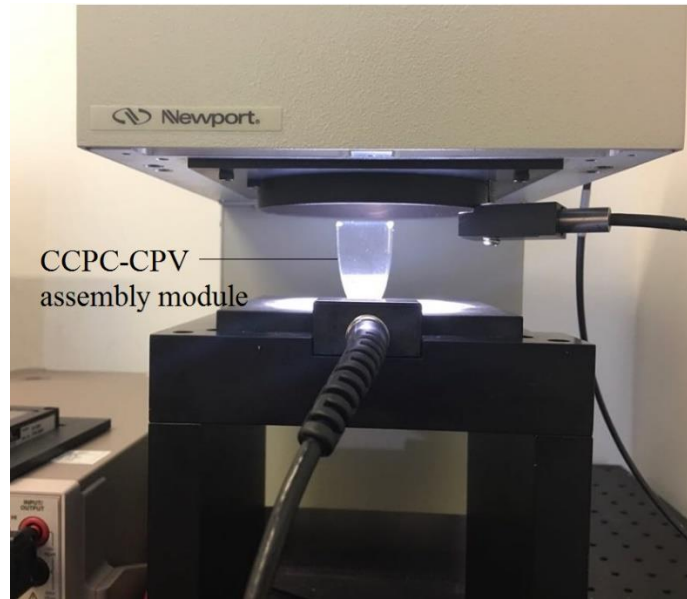


Figure 3.12: Indoor experiment was set-up to measure the output current of the CCPC-CPV assembly module and for single MJSC respectively.

The spectrum data of the light source generated by the solar simulator was measured using a AVANTES spectrometer, and a real-time data is collected through the software AvaSoft. From the actual data collected by the spectrometer, a wide range of wavelengths from 180nm to 1800nm is captured. The measured spectral irradiance was then substituted as $S_L(\lambda)$ in Eqns. (3.10) and (3.11) to calculate the output current of the CCPC-CPV assembly modules. In this case, it can be safely assumed that both the indoor experiment and ray-tracing simulation were referred to the light source with the same spectral for irradiance.



Figure 3.13: Five unit of CCPC-CPV assembly modules used for indoor measurement.

Next, five unit of CCPC-CPV assembly modules are used to collect data for $I_{CCPC-CPV}$ as shown in Figure 3.13. The effective SCR of the CCPC-CPV assembly module can be obtained by comparing $I_{CCPC-CPV}$ (module with CCPC lens) and I_{CPV} (module without CCPC lens). Hence, five units of MJSC are used to measure I_{CPV} , too. The entrance aperture of both CPV modules (with and without CCPC lens) are fixed at the same height and placed in a fixed position to assure both receive the same amount of incident light within the same acceptance angle. Both reading for $I_{CCPC-CPV}$ and I_{CPV} is taken directly by pointing the digital multimeter's probes onto the MJSC terminal to maintain the lowest possible resistance on the connection. The measurement is repeated for five times for each module. The empirical result is tabulated and will be discussed in the next chapter.

3.4.3 Outdoor measurement

The outdoor performance of the CCPC lens has been established under actual working environment. The experiment is carried out on the rooftop of Universiti Tunku Abdul Rahman in Bandar Sungai Long, Selangor. In contrast to the laboratory test, the situation becomes more complicated for outdoor experiment due to the variation of ambient conditions and direct exposure to the sun. For that reason, a tester box is designed for outdoor measurement purpose. The design was inspired by the concept of pyrheliometer in which the tracking error angle, $\angle \alpha$, of 0.1° and opening angle, $\angle \beta$, of 2.5° were considered as depicted in Figure 3.14. It allows both modules being exposed to the same amount of incident light within the same view angle. The dimension is calculated through the following equations,

$$H = \frac{L1}{\tan \angle \beta - \tan \angle \alpha} \quad (3.13)$$

$$L2 = H \tan \angle \alpha \quad (3.14)$$

where H represents the height between the receiver's entrance aperture and the opening, $\angle \alpha$ represents the tracking error angle, $\angle \beta$ represents the full view angle, $L1$ is the half-length of the receiver and $L2$ is the gap distance between the opening and the edge of receiver. The outer surface was sprayed in black coating to isolate the inner part from the diffused light.

For outdoor measurement, the $I_{CCPC-CPV}$ and I_{CPV} is measured through connecting the soldered external connecting wires to the digital multimeter. This is because the tester box needs to be fully covered to isolate the diffuse light. This might cause some deviation between indoor and outdoor

measurement due to the wire's resistance but won't be significant enough to affect the overall outcome.

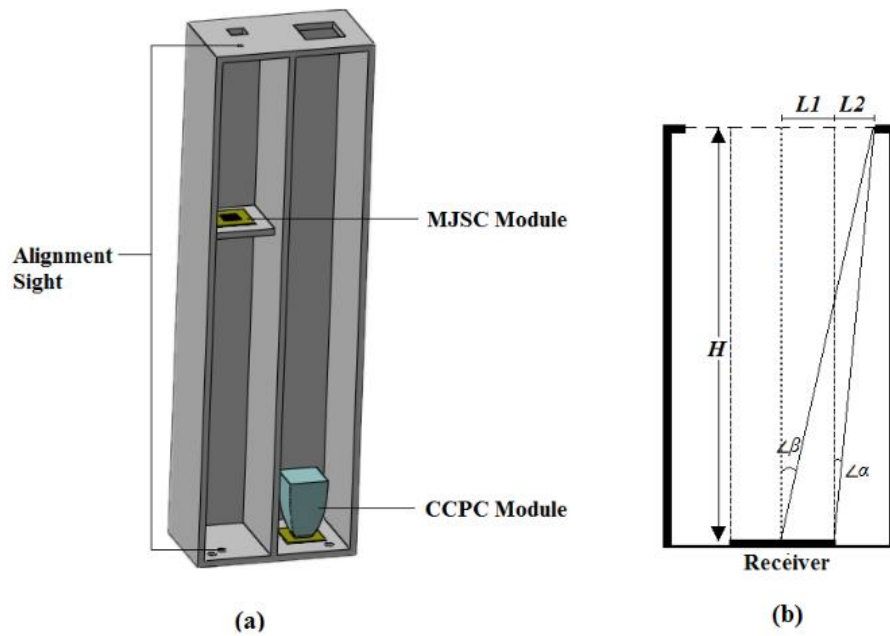


Figure 3.14: (a) The illustrative 3D model and (b) schematic diagram of the tester case.

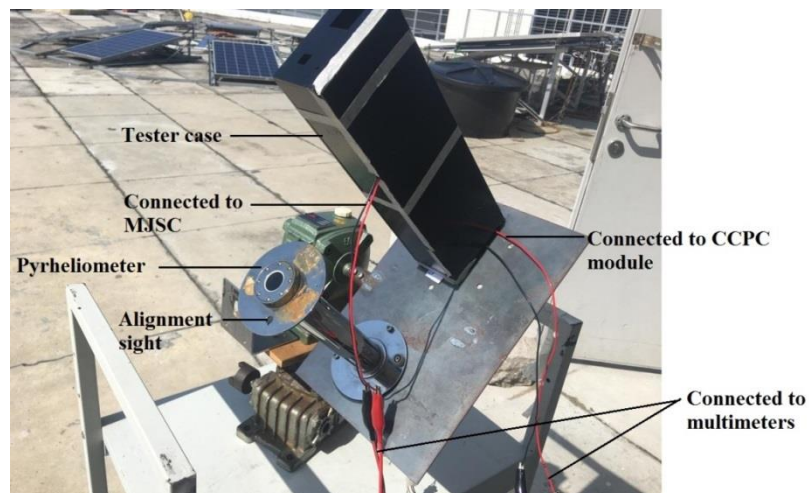


Figure 3.15: Experimental setup for outdoor measurement.

The facing direction of the instrument can be adjusted manually. The alignment sight holes were used as reference for easy and precise optical alignment to ensure the instruments always facing towards the sun. A pyrheliometer was installed and aligned with the tester box to measure the direct beam irradiance from the sun. With the outdoor experimental setup as shown in Figure 3.15, the measurements were done and repeated on different days and period of time so that more variations of data can be acquired for detailed analysis. The collected data is presented and will be further discussed in next chapter.

CHAPTER 4

RESULT AND DISCUSSION

4.1 Comparison between full solar spectrum and single wavelength in simulation

In this project, it is advocated that full solar spectrum should be utilized in the simulation with wavelengths ranging from 300 nm to 1800 nm at the resolution of 10 nm to emulate actual condition of the solar spectral irradiance. Based on the simulation result, the solar concentration ratio versus wavelength of light source has been plotted throughout the whole solar spectrum as shown in Figure 4.1. Starting from 300 nm, the solar concentration ratio of CCPC-CPV assembly module increases steeply upward and then remains at high solar concentration ratio in the range of visible light (400 nm to 650 nm). However, the solar concentration ratio drops slightly when the wavelength of the solar spectrum further increases in the range of infrared region (650 nm – 1800 nm). In addition, the properties of all the materials also behave differently at different wavelengths of the solar spectrum. From the simulation, the peak of the graph is located at the wavelength of 550 nm, where it yields a SCR of 4.85. However, the average SCR of the full solar spectrum is 4.65, which means an overestimation of output power will happen by using single wavelength without considering the full solar spectrum.

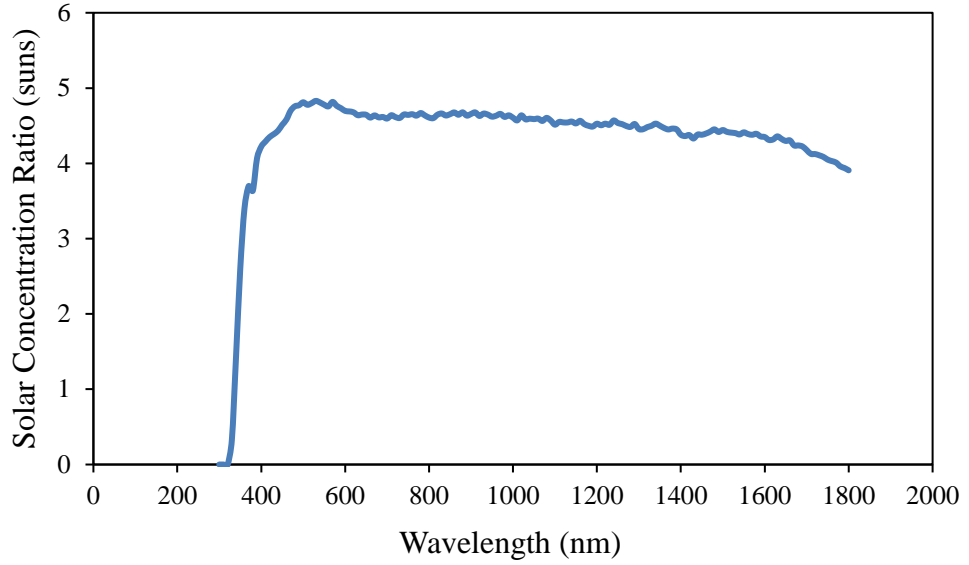


Figure 4.1: Variation of solar concentration ratio of CCPC-CPV assembly module under full solar spectrum.

4.2 The optical behaviour under different angle of incidence

The optical characteristic of the CCPC-CPV module is studied in omnidirectional. Figure 4.2 illustrated the ray tracing simulation of the CCPC-CPV assembly module under different angle of incidences where Figure 4.2(a) is the simulation under perpendicular light source while the zenith angle, Φ_Z for Figure 4.2(b) and (c) are 10° and 20° respectively (azimuth angle, Φ_A remains at 0°).

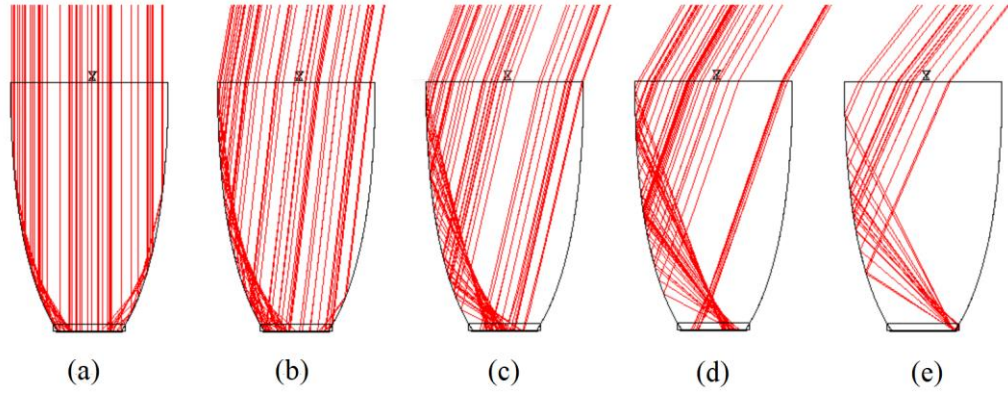


Figure 4.2: Ray tracing simulation of the CCPC-CPV assembly module under light source with azimuth angle, $\Phi_A = 0^\circ$ while zenith angle, Φ_Z equals to (a) 0° (b) 10° , (c) 20° , (d) 30° , and (e) 37.77° .

On the other hand, Figure 4.3 shows the concentrated flux distribution of the focused solar image on the active region of MJSC for different incident angles relative to CCPC aperture. The solar flux shifted aside when the zenith angle, Φ_Z , increases, whilst it shifted towards to the corner edge of the receiver when azimuth angle, Φ_A , increases. It can be observed that when the light source is perpendicular to the module, the central region of the CPV cell received lesser flux as compared to the peripheral region. It is because the light rays hitting on the CCPC inner wall are mostly total internal reflected to the peripheral regions especially the four corner regions as shown in Figure 4.2 (b). Table 4.1 depicts the optical efficiency of the CCPC-CPV assembly module for zenith angle ranging from 0° to 37.77° and azimuth angle ranging from 0° to 360° . The data was then plotted in Figure 4.4.

Table 4.1: The optical efficiency of the CCPC-CPV assembly module for zenith angle ranging from 0° to 37.77° and azimuth angle ranging from 0° to 360° .

Azimuth Angle, Φ_A	Zenith angle, Φ_Z				
	0	10	20	30	37.7
0	72.34	70.83	66.23	57.64	26.36
15	72.36	70.99	66.34	57.25	35.09
30	72.21	71.09	66.40	57.91	44.63
45	72.32	71.38	66.29	57.52	46.59
60	72.21	71.14	66.43	57.85	44.56
75	72.39	70.91	66.52	57.27	35.12
90	72.34	70.85	66.24	57.67	26.36
105	72.36	70.99	66.34	57.23	35.09
120	72.21	71.09	66.40	57.94	44.63
135	72.32	71.38	66.29	57.52	46.59
150	72.21	71.14	66.43	57.85	44.56
165	72.39	70.91	66.52	57.27	35.12
180	72.34	70.84	66.24	57.67	26.36
195	72.36	70.99	66.34	57.23	35.09
210	72.21	71.09	66.40	57.94	44.63
225	72.32	71.38	66.29	57.52	46.59
240	72.21	71.14	66.43	57.85	44.56
255	72.39	70.91	66.52	57.27	35.12
270	72.34	70.85	66.24	57.67	26.36
285	72.36	70.99	66.34	57.23	35.09
300	72.21	71.09	66.40	57.94	44.63
315	72.32	71.38	66.29	57.52	46.59
330	72.21	71.14	66.43	57.85	44.56
345	72.39	70.91	66.52	57.27	35.12

The highest optical efficiency of approximately 72.34% can be obtained at the normal incidence with the angle ($\Phi_Z = 0$, $\Phi_A = 0$). Theoretically, all the light rays with incident angles less than half of the acceptance angle should be concentrated to the active area of MJSC. However, the amount of concentrated solar flux on the MJSC receiver decreases when the incident angle increases even though the incident angle is still less than half of the acceptance angle.

The optical losses become more severe especially when the incident angle more than 30° as it approaches half of the acceptance angle. The optical efficiency drops significantly and reduces to below 50% after incident angle has reached 35° even though it is still less than the half acceptance angle of 37.77° .

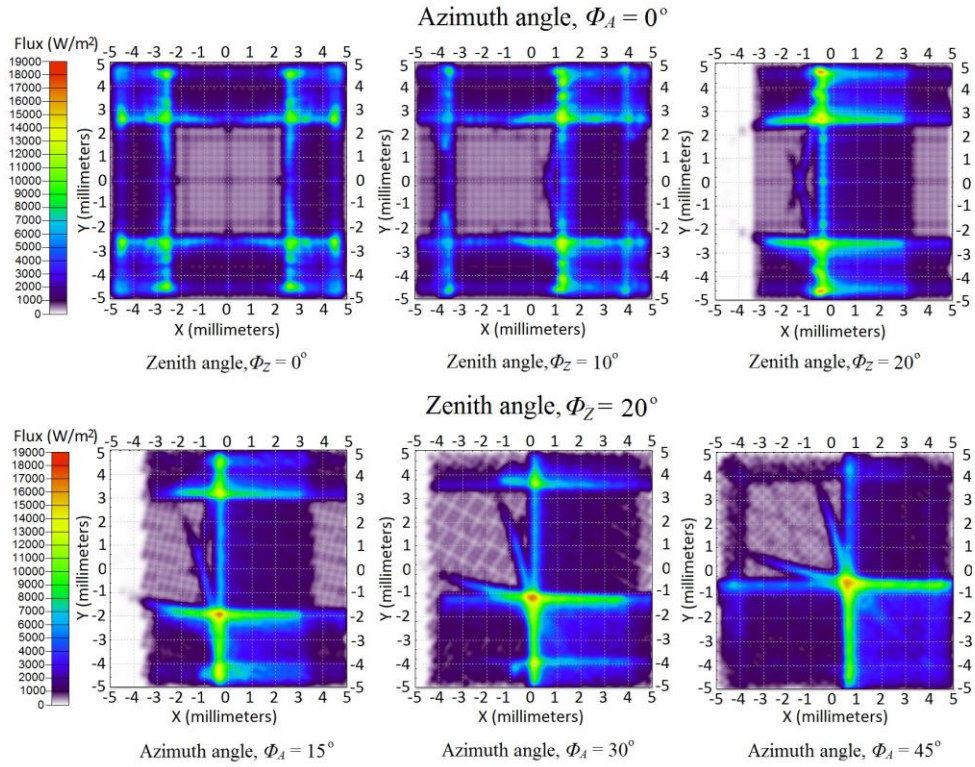


Figure 4.3: The simulated flux distribution map on the MJSC receiver under different angles of incidence.

On the other hand, when the light source is directed diagonally ($\Phi_A = 45^\circ, 135^\circ, 225^\circ, 315^\circ$) toward the CCPC-CPV module, the CCPC lens will receive more solar flux because the light can hit on two side walls simultaneously as shown in Figure 4.4. It can be clearly seen that when $\Phi_A = 90^\circ$ as depicted in Figure 4.4(a), the incoming rays incident mainly on one side

wall only. The simulated flux distributed on the receiver module when $\Phi_A = 0^\circ$, 90° , 180° and 270° is presented in Figure 4.5, where it can be observed that only a minimal amount of flux is received on one side of the receiver module. On the other side, when $\Phi_A = 45^\circ$ as shown in Figure 4.4(b), the incoming light rays strike two walls at the same time which permit more chances for the incoming light rays to refract towards the receiver module, thus resulted in higher flux received. The same phenomenon applies on the other diagonal angle.

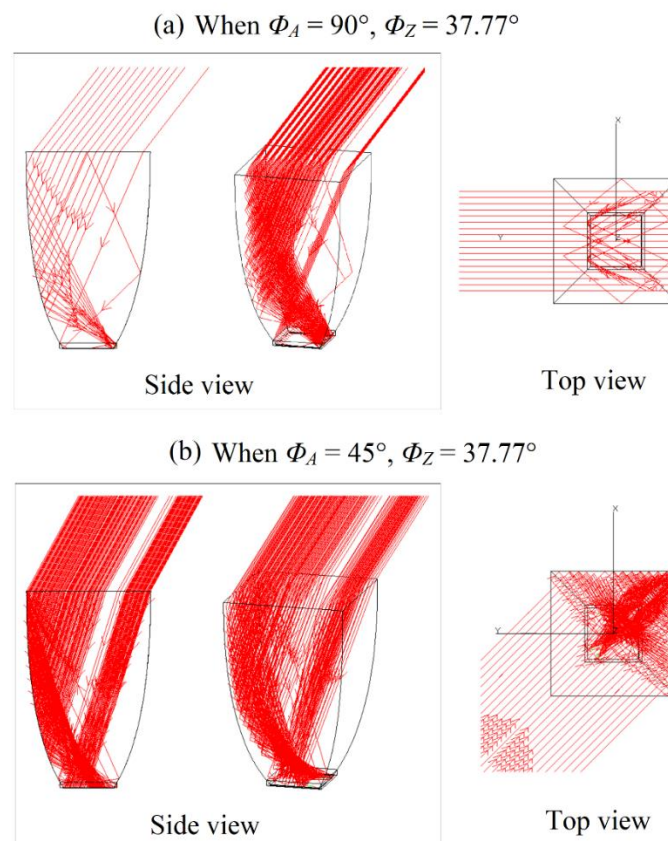


Figure 4.4: The ray tracing simulation of the CCPC-CPV assembly module from various points of view when (a) $\Phi_A = 90^\circ$ and $\Phi_Z = 37.77^\circ$, (b) $\Phi_A = 45^\circ$ and $\Phi_Z = 37.77^\circ$.

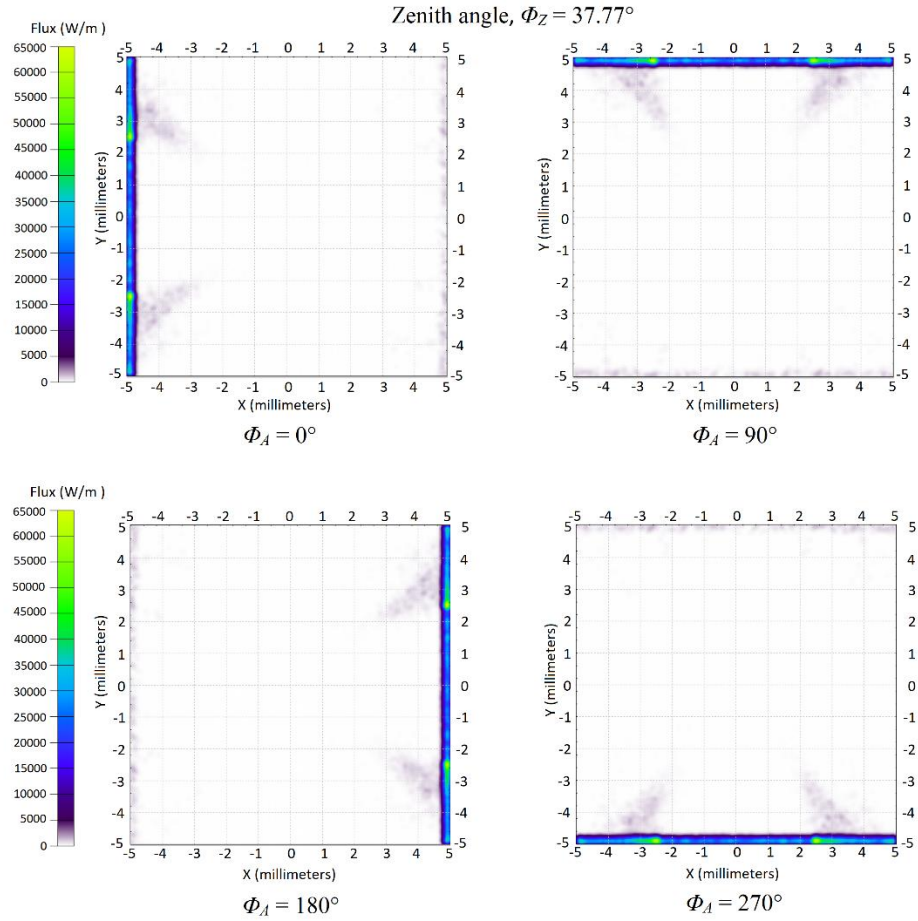


Figure 4.5: The simulated flux distribution map on the MJSC receiver with $\Phi_A = 0^\circ, 90^\circ, 180^\circ$ and 270° while $\Phi_Z = 37.77^\circ$.

It can also be proven through the simulation result as depicted in Figure 4.6; the optical efficiency for the Φ_A of $45^\circ, 135^\circ, 225^\circ$ and 315° is higher as compared to that of other azimuth angles. Figure 4.7 shows the overall simulated results of the distribution of SCRs for various angles of incidence. The highest SCR is obtained at zenith angle, Φ_Z below 10° and the then SCR gradually decreases as the zenith angle, Φ_Z increases. Based on Figure 4.6, optical efficiency is not affected by the azimuth angle unless the incident angle is close to the half angular acceptance angle of the CCPC lens, which is 37.77° .

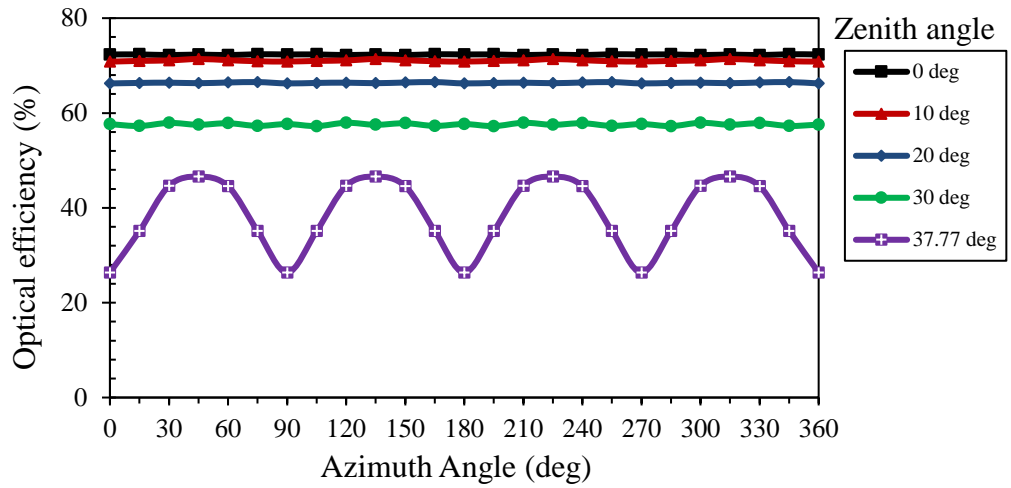


Figure 4.6: The optical efficiency of the CCPC-CPV assembly module in 2D-plot for zenith angle from 0° to 37.77° and azimuth angle from 0° to 360° .

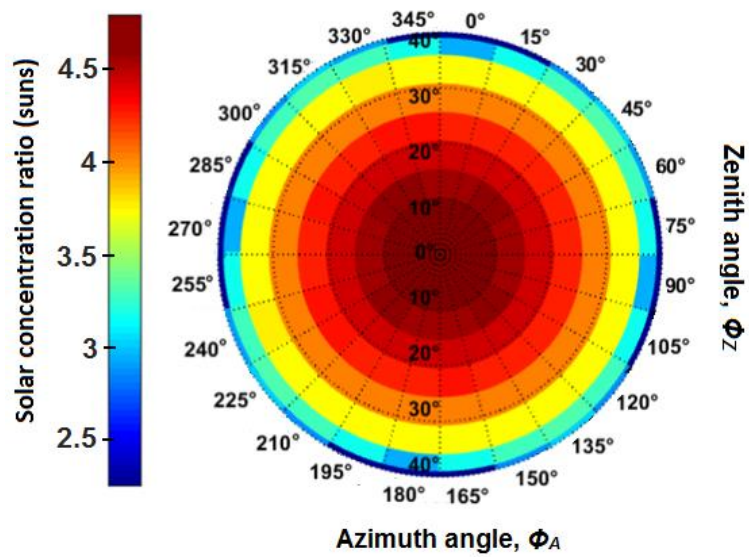


Figure 4.7: Distribution of solar concentration ratio at different angles of incidence.

4.3 Optical efficiency profile of CCPC-CPV assembly module

Through the study, it is found that when light rays strike on the edge of the CCPC's side wall, it will be lost for unknown reason. This optical loss is demonstrated in Figure 4.8 and it is known as edge/corner leakage in this study.

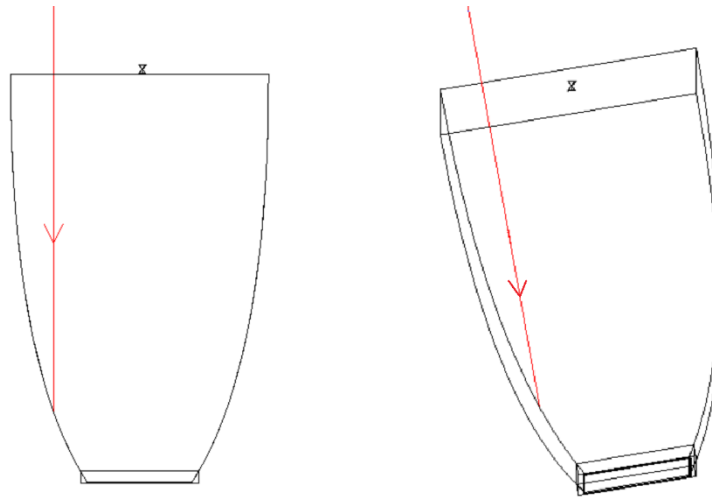


Figure 4.8: Light rays fall on the edge of side wall is lost for unknown reason.

In order to identify positions that may lead to the losses, the optical efficiency at each particular point via the entrance aperture is retrieved through computational method and presented in Figure 4.9(a). As a comparison, the real optical losses under direct normal irradiance can be observed with naked eyes (referring to Figure 4.9(b)). Blue region represents area with least optical power received, in other words, the highest losses. Severe optical losses can be seen at each edge/corner of the exit aperture due to the optical adhesive spillage as an obvious light is depicted from each edge/corner of the lens.

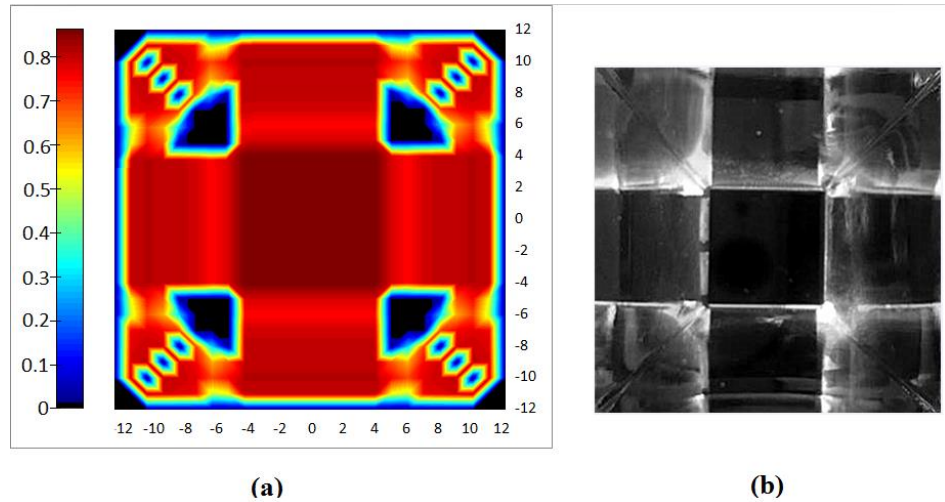


Figure 4.9: The optical efficiency profile of CCPC-CPV assembly module indicates severe optical losses are incurred at the edge/corner under direct normal irradiance. (a) Computational result. (b) Top view of actual CCPC-CPV assembly module observed with the naked eye.

As mentioned in the previous section, the use of optical adhesive will cause some losses. The losses due to adhesive spillage is demonstrated in Figure 4.10. Some light rays are refracted away from the MJSC due to the change of refractive index caused by the optical adhesive. However, the use of bonding adhesive is unavoidable, therefore four different thicknesses of adhesive layer are tested in the simulation to see how it will affect the performance.

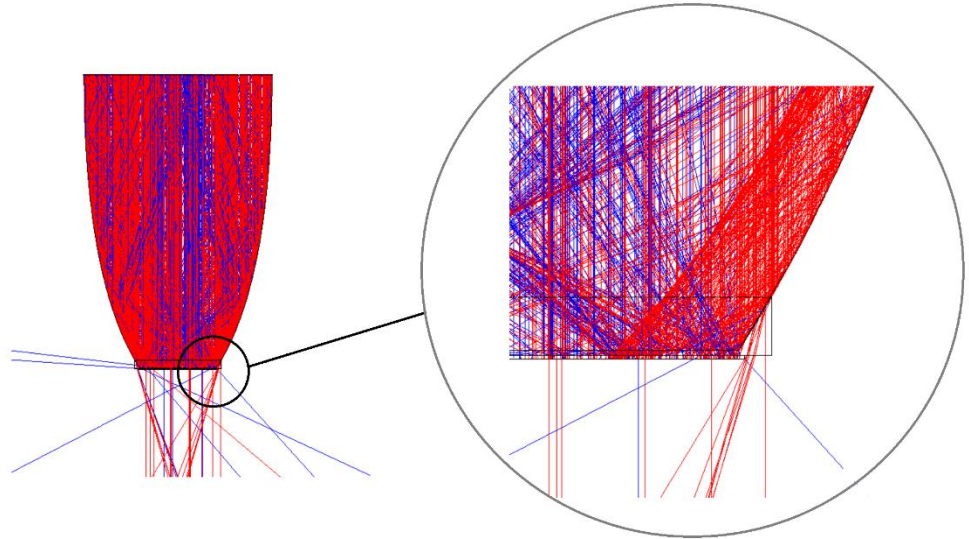


Figure 4.10: Escaping light rays due to adhesive spillage.

Figure 4.11 shows how the thickness of adhesive can affect the optical efficiency under different incident angle in which the greater the thickness of the adhesive spillage, the lower the optical efficiency. For the rest of the simulation, the thickness of the adhesive layer, t_{al} is set as 1 mm and thickness of the spillage surrounding the lens, t_{as} is 0.9 mm because it is the closest value to the actual adhesive thickness in the CCPC-CPV assembly module.

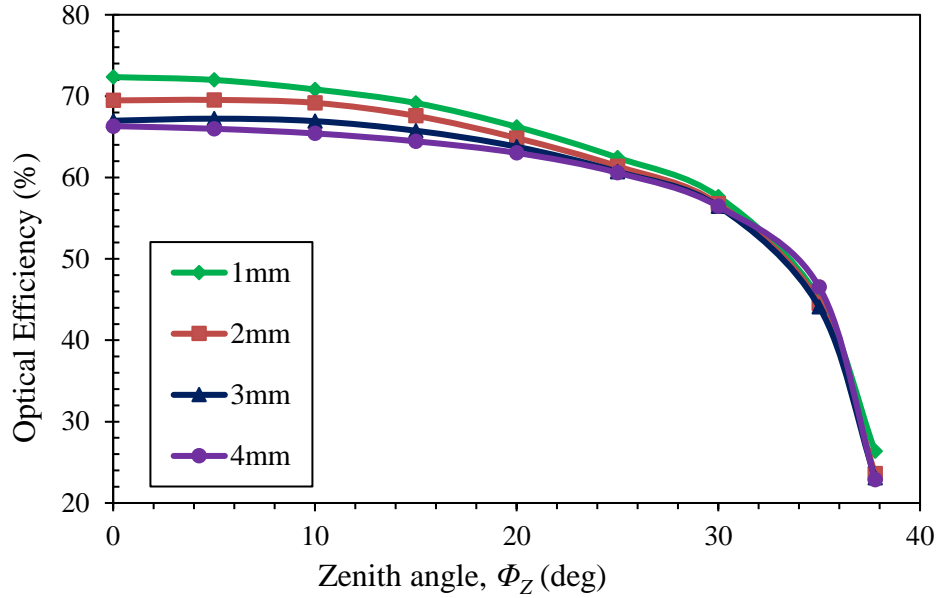


Figure 4.11: The optical efficiency of CCPC-CPV assembly module versus different zenith angle, Φ_Z , while azimuth angle, $\Phi_A = 0$, for different thicknesses of adhesive layer, t_{al} .

4.4 Optical losses occur at each component level

There are three parts involved in the CCPC-CPV assembly module, which mean there will be different kinds of optical losses in the module. These optical losses are verified with more evidence based on a detailed study. The percentage of the optical losses occur in each component have been analysed and presented in Table 4.2. The optical losses have been studied by comparing the optical power received at each layer with the subsequent layer. The visualized result is shown in Figure 4.12. In overall, the optical losses can be divided into three phases depending on the location of the light rays:

- Before entering the CCPC lens
- Within the CCPC lens
- After exit from the CCPC lens

The Fresnel reflection losses can be predicted by TracePro accurately by defining the absorption coefficient, α extinction coefficient, k and refractive index, n corresponding to different wavelengths. Apart from that, the Fresnel reflection losses can also be validated through calculation using the equation as follows,

$$R_{Fresnel} = \frac{(n_1 - n_2)^2}{(n_1 + n_2)^2} \quad (4.1)$$

where n_1 and n_2 are the refractive indices of the two mediums. For instances, the predicted Fresnel Loss I that occur in the first phase is 4.21% while the outcome of calculation is 4.22%. It is proven that the outcome predicted by the software is reliable and accurate. However, the predicted value is selected to use in all the analysis to ensure the consistency. As expected, Fresnel reflection losses have been occurred thrice throughout the three phases as the incident rays travelled through four different mediums (air \rightarrow B270 Schott glass \rightarrow optical adhesive \rightarrow MJSC). The Fresnel reflection loss II (from CCPC lens to optical adhesive) is small as the refractive indices gap is small. For Fresnel loss III, the difference between refractive indices of the two mediums is relatively high, which causes a higher optical loss when light travelling between optical adhesive and MJSC.

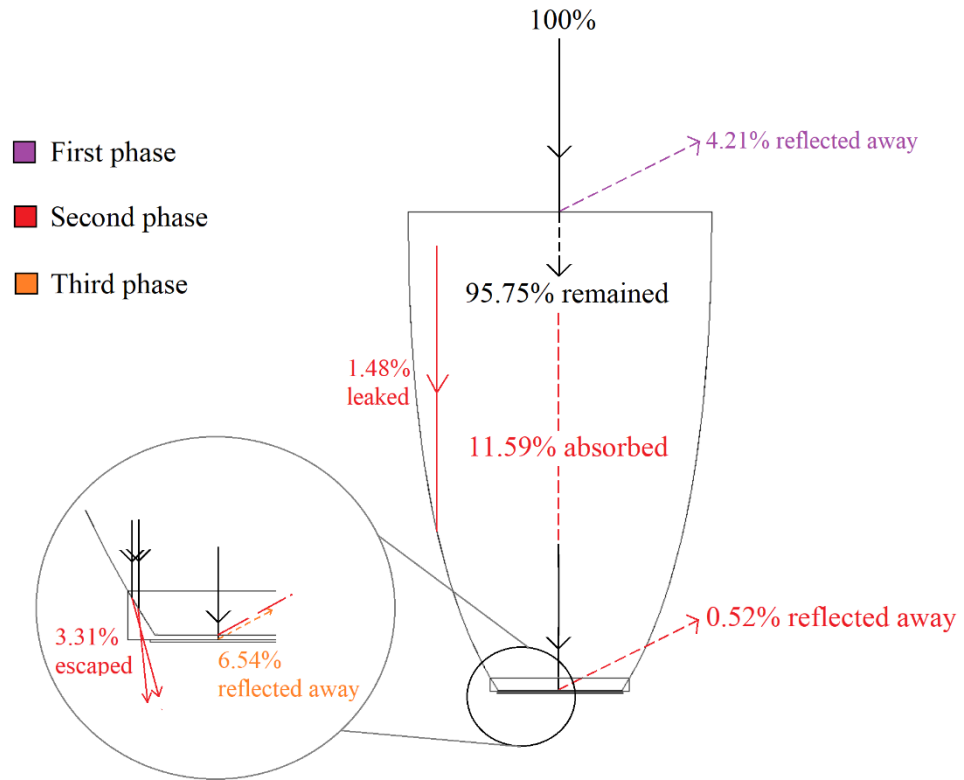


Figure 4.12: Optical losses occur at each of the component level.

The absorption loss of CCPC lens has been simulated using ray-tracing method on the CCPC lens only with the amount as high as 11.59%. However, the absorption loss is unavoidable as the geometry of the CCPC lens is designed to match with the dimension and of the MJSC as well as the rim angle of the POE proposed in previous work. The purpose of this study is to develop a simulation technique that is suitable to investigate the characteristics of the CCPC module for the application of UHCPV system proposed in previous work. So, it is impossible to modify the geometry of the CCPC lens in this study and this became a shortcoming of the design in current stage. Further adjustment can be made to the geometry of the CCPC lens in future to achieve

a balance between the two. Next, the absorption of optical adhesive can be neglected as the thickness is too small to affect the outcome.

The percentage of each loss is calculated with respect to the input power entering the entrance aperture of CCPC lens. The optical efficiency of the CCPC-CPV assembly module is 72.35% after considering the total optical losses as listed in Table 4.2. In order to determine the efficiency of CCPC lens, the optical efficiency of CPV module is retrieved as 93.62% by simulating only MJSC. It is reasonable as only Fresnel loss will occur when light rays entered MJSC from air. As a result, the effective optical efficiency of CCPC lens can be obtained as 77.30% via dividing the optical efficiency of CCPC-CPV assembly module by the optical efficiency of CPV module alone.

Table 4.2 The optical losses at each component level of the CCPC module.

Type of losses	Percentage (in term of input)
Fresnel Loss I – From air to CCPC	4.21%
Absorption Loss – CCPC lens (B270 Schott Glass)	11.59%
Edge/Corner Leakage	1.48%
Optical losses caused by light escaping from adhesive	3.31%
Fresnel Loss II – From CCPC to optical adhesive	0.52%
Fresnel Loss III – From optical adhesive to MJSC	6.54%
Total losses	27.65%

4.4 Results for indoor and outdoor experiments

A simulated SCR of 4.65 is calculated by comparing the output current of the CCPC-CPV assembly module with the output current of the CPV module alone as shown in equation (3.12). The resulted optical efficiency of the CCPC lens

is 77.4% (4.65 out of GCR of 5.998) which is supported by the optical efficiency of 77.3% computed from the breakdown analyses as in Table 4.2. Next, an indoor experiment is conducted. Spectral irradiance emitted from the solar simulator has been measured with a spectrometer and the data is compiled with the simulated data for further analysis and SCR calculation.

The data collected during indoor experiment is recorded in Table 4.3. The measurement of each module is calculated based on the average of five readings. Consequently, the average I_{CPV} is 9.46 mA while the average $I_{CCPC-CPV}$ is 43.26 mA, which results in the SCR of 4.57. A minor difference of 1.8% is shown between the simulated and indoor measured SCRs. In overall, the effective optical efficiency of the CCPC-CPV assembly module under direct light source with full solar spectrum is 76.2% (4.57 out of GCR of 5.998).

Table 4.3: Indoor measurement for five MJSC and CCPC-CPV assembly modules respectively.

MJSC	I_{CPV} (mA)	CCPC-CPV assembly module	$I_{CCPC-CPV}$ (mA)
Cell 01	9.22	Module 01	42.9
Cell 02	9.43	Module 02	43.7
Cell 03	9.60	Module 03	43.8
Cell 04	9.45	Module 04	42.6
Cell 05	9.60	Module 05	43.3
Average	9.46		43.26

Furthermore, the evaluation of CCPC-CPV assembly module has been carried forward with an outdoor measurement. In this work, the outdoor experiment has been set-up with the consideration of the same amount of input

incidence and acceptance angle received by the MJSC and CCPC–CPV assembly module. The data collected during outdoor measurement is tabulated in Table 4.4, 4.5 and 4.6 over three days of experiment. For all three days, the data were measured on sunny day with mostly clear skies at particular local time.

Table 4.4: Outdoor data collection on 19th February 2019, weather condition: sunny day with mostly clear skies.

Local Time, GMT +8 (h)	DNI (W/m²)	<i>I</i>_{CPV} (mA)	<i>I</i>_{CCPC-CPV} (mA)	SCR (suns)
12:10	750.0	8.04	36.8	4.58
12:15	612.5	7.76	35.9	4.63
12:20	762.5	9.86	45.5	4.61
12:25	775.0	9.92	45.6	4.60
12:30	512.5	6.32	29.0	4.59
12:35	712.5	8.87	41.3	4.66
12:40	775.0	9.67	44.5	4.60
12:45	762.5	9.36	43.8	4.68
12:50	775.0	9.88	46.7	4.73
12:55	787.5	9.83	46.4	4.72
13:00	787.5	9.49	44.4	4.68
13:05	625.0	7.88	35.5	4.51
13:10	775.0	9.88	41.8	4.23
13:15	700.0	9.13	42.8	4.69
13:20	700.0	9.12	42.4	4.65
13:25	25.0	0.57	2.5	4.39
13:30	687.5	8.88	40.0	4.50
13:35	625.0	8.2	37.6	4.59
13:40	712.5	8.77	39.8	4.54
13:45	537.5	6.79	30.9	4.55
13:50	737.5	8.78	40.9	4.66
13:55	625.0	7.98	36.5	4.57
14:00	600.0	7.55	34.4	4.56
Average		8.37	38.5	4.60

Table 4.5: Outdoor data collection on 21st February 2019, weather condition: sunny day with mostly clear skies.

Local Time, GMT +8 (h)	DNI (W/m²)	<i>I</i>_{CPV} (mA)	<i>I</i>_{CCPC-CPV} (mA)	SCR (suns)
10:40	762.5	9.65	44.3	4.59
10:45	750.0	9.18	42.9	4.67
10:50	775.0	9.77	44.8	4.59
10:55	787.5	9.56	44.0	4.60
11:00	775.0	9.92	45.3	4.57
11:05	812.5	10.36	46.7	4.51
11:20	825.0	10.25	46.5	4.54
11:25	825.0	10.46	47.4	4.53
11:30	837.5	10.66	48.0	4.50
11:35	825.0	10.51	47.9	4.56
11:40	812.5	10.53	48.4	4.60
11:45	850.0	10.95	50.1	4.58
11:50	825.0	10.65	48.9	4.59
11:55	850.0	10.95	49.6	4.53
12:00	862.5	11.06	48.4	4.42
12:05	850.0	11.05	49.8	4.50
12:10	850.0	11.11	50.0	4.52
12:20	887.5	11.31	50.8	4.49
12:25	850.0	10.87	48.1	4.43
12:30	812.5	10.34	46.7	4.52
12:35	825.0	10.38	47.4	4.57
12:40	837.5	10.73	47.1	4.39
12:45	737.5	9.35	40.8	4.36
12:50	612.5	7.68	33.5	4.36
12:55	662.5	8.57	38.7	4.52
13:20	850.0	10.95	48.5	4.43
13:25	850.0	10.95	48.9	4.47
13:30	812.5	8.8	42.5	4.83
13:35	850.0	10.79	46.4	4.30
13:40	862.5	11.59	49.6	4.28
13:50	850.0	11.53	48.5	4.21
13:55	862.5	11.53	48.8	4.23
14:00	350.0	4.46	20.0	4.48
14:05	912.5	11.61	49.8	4.29
14:15	562.5	6.91	29.8	4.31
14:30	825.0	10.15	42.5	4.19
14:35	900.0	11.47	49.3	4.30
14:40	900.0	11.38	48.4	4.25
Average		10.21	45.5	4.46

Table 4.6: Outdoor data collection on 22nd February 2019, weather condition: sunny day with mostly clear skies.

Local Time, GMT +8 (h)	DNI (W/m²)	<i>I</i>_{CPV} (mA)	<i>I</i>_{CCPC-CPV} (mA)	SCR (suns)
12:40	900.0	11.37	50.6	4.45
12:45	850.0	10.76	47.6	4.42
12:50	812.5	10.15	45.3	4.46
12:55	850.0	10.89	48.5	4.45
13:05	900.0	11.56	51.1	4.42
13:10	937.5	11.81	52.0	4.40
13:15	925.0	11.57	50.5	4.36
13:20	925.0	11.59	51.0	4.40
13:25	912.5	11.52	50.5	4.38
13:30	912.5	11.46	52.4	4.57
13:35	875.0	11.28	49.4	4.38
13:40	900.0	11.52	50.6	4.39
13:50	900.0	11.49	50.8	4.42
13:55	912.5	11.50	50.7	4.41
14:00	925.0	11.60	51.2	4.41
14:15	912.5	11.69	52.4	4.48
14:30	87.5	0.52	2.3	4.42
14:40	887.5	10.92	45.7	4.18
14:45	900.0	11.29	48.3	4.28
14:50	850.0	11.11	51.2	4.61
15:10	662.5	8.52	36.1	4.24
15:15	37.5	0.41	1.7	4.15
15:20	37.5	0.41	1.7	4.15
15:25	862.5	11.20	50.4	4.50
15:30	862.5	10.80	49.4	4.57
15:35	875.0	11.25	48.6	4.32
15:40	225.0	2.54	11.0	4.33
Average		9.61	42.4	4.41

The SCR of the CCPC-CPV assembly module under different solar irradiance is plotted in Figure 4.13. It can be seen from the graph that the SCR is less likely to be affected by the energy density of solar irradiance. By taking the average of all the outdoor measurements, a SCR of 4.48 is obtained with relative standard deviation of 3.25%, which indicates an effective efficiency of 74.7% (4.48 out of GCR of 5.998) under real working condition. This outcome

is acceptable as the outdoor measurement including the consideration of solar disc effect as well as the weather changes on the experiment days.

A summary of the simulated and experimental results is tabulated in Table 4.7. It can be seen that the simulated result is in a good agreement with the experimental result as the differences between the computational and outdoor experiment is only 3.8%. On the other side, when the indoor measurement is compared with the single wavelength simulated result, the difference between laboratory and simulated result increases from 1.8% to 4.8%. Once again, it is proven that utilizing full solar spectrum is way more reliable and accurate compared to single wavelength simulation.

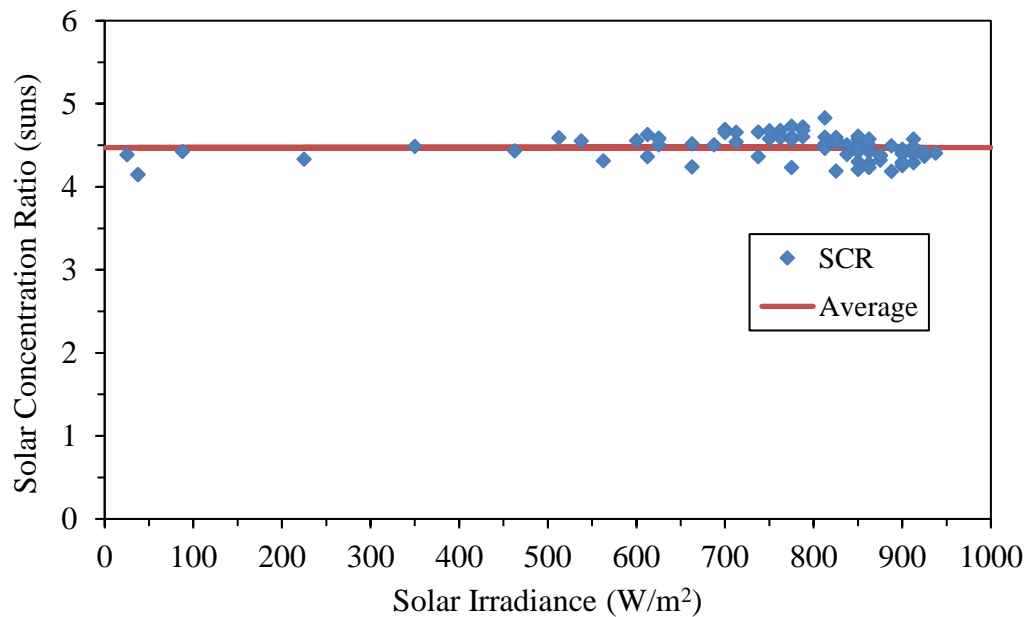


Figure 4.13: SCR of the CCPC-CPV assembly module under different solar irradiance.

Table 4.7: The outcome comparison between the simulation, indoor and outdoor experiment.

	Simulated result		Indoor measured result	Outdoor Measured result
	Single wavelength 550nm	Full solar spectrum		
$I_{CCPC-CPV}$	67.32 mA	45.29 mA	43.26 mA	42.13 mA
I_{CPV}	14.04 mA	9.75 mA	9.46 mA	9.40 mA
Solar Concentration Ratio (SCR)	4.79 suns	4.65 suns	4.57 suns	4.48 suns
Optical Efficiency	79.9%	77.40%	76.2%	74.7%
Percentage difference between simulated and indoor experimental SCR	4.8%	1.8%		
Percentage difference between simulated and outdoor experimental SCR	6.9%	3.8%		

4.5 Overall performance of UHCPV system

For the last phase of this research, a ray-tracing simulation for the whole UHCPV system (integration of POE and SOE) is conducted. The model for ray-tracing simulation consists of 480 pieces of facet mirrors as the POE whereas the SOE is consists of four CCPC modules (2×2 array). Figure 4.14 illustrates the ray-tracing simulation of the UHCPV system where the irradiance rays is injected on NIDC, then reflected towards the entrance aperture of CCPC lens for further concentration before entering to solar cell.

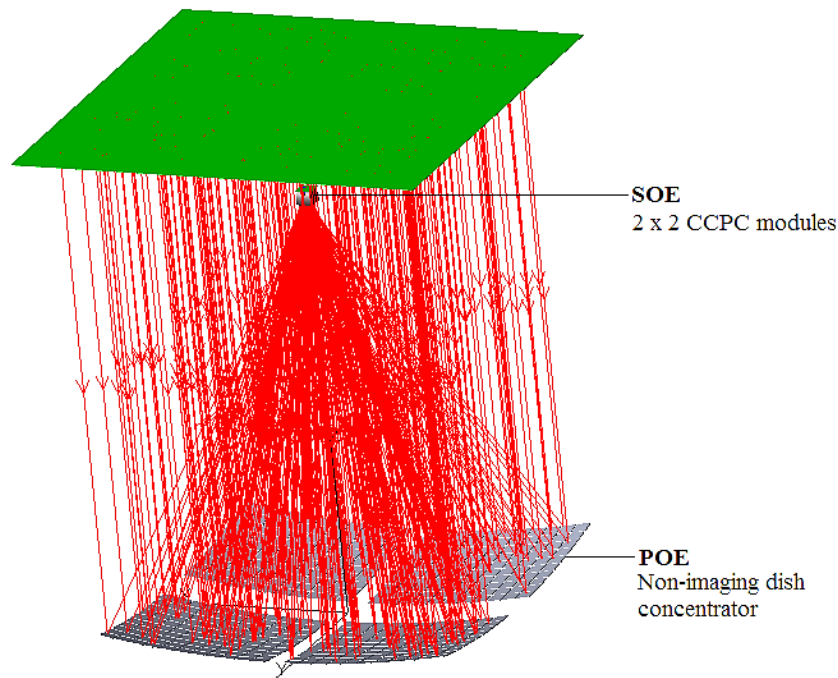


Figure 4.14: Ray-tracing simulation for the UHCPV system.

The dimension of each square facet mirror is $4 \text{ cm} \times 4 \text{ cm}$ with an area of 16 cm^2 . It is assigned into 22 rows and 22 columns while four mirrors at the centre are taken off to avoid losses caused by the shadow of the receiver module. The total reflective area of NIDC is 7680 cm^2 . On the contrary, the 2×2 array CCPC modules form a total entrance aperture of $48.5 \text{ cm} \times 48.5 \text{ cm}$ (with a minor gap spacing of 0.5 mm between adjacent lenses). The simulated flux distribution map on the SOE's entrance aperture and the MJSC receiver is shown in Figure 4.15. As a result, the reflected rays from POE forms a focused image of $20 \text{ mm} \times 20 \text{ mm}$. This once again proven the significance of implementing the CCPC lens onto the MJSC. The active area of the MJSC is only $9.8 \text{ mm} \times 9.8 \text{ mm}$, which mean the solar irradiance fall onto the DBC will be wasted if there is no CCPC lens to direct the sunlight towards the solar cell.

The reflection formed at the entrance aperture of SOE is shown in Figure 4.15(a).

The overall SCR for the whole UHCPV system is calculated by comparing the power intensity onto the MJSC receiver with the standard irradiance of 1000 W/m^2 . An overall SCR of 1144.3 suns is obtained through the simulation. This can prove that the integration of CCPC as a SOE into the NIDC able to achieve ultra-high solar concentration ratio which is more than 1000 suns. Nevertheless, further study and analysis is required to investigate the losses incurs in the simulation for whole UHCPV system as it may incur different losses as compare to the study of single CCPC module. It involves more uncertainty and losses that is yet to be justified.

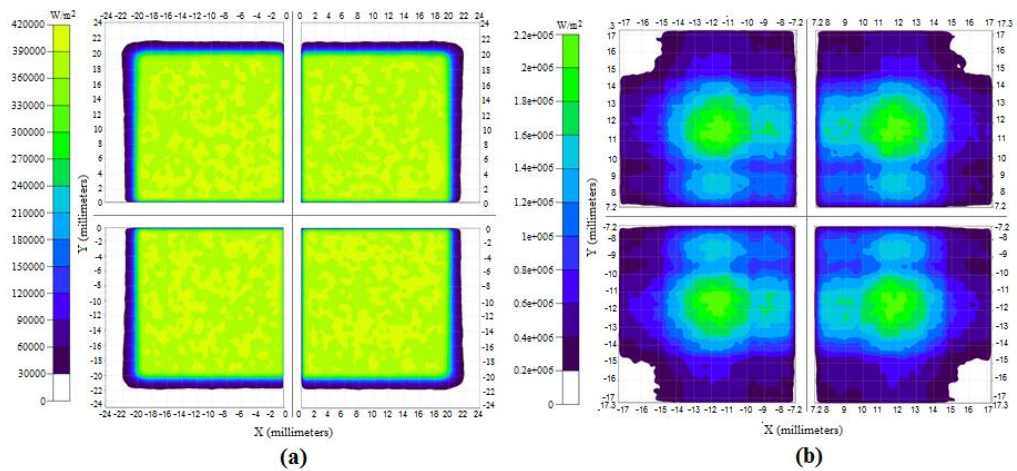


Figure 4.15: The simulated flux distribution map on (a) the CCPC lens' entrance apertures (b) the MJSCs.

CHAPTER 5

CONCLUSION AND FUTURE WORK

5.1 Conclusion

A comprehensive optical analysis on assembly of dielectric filled crossed compound parabolic concentrator (CCPC) and concentrator photovoltaic module (CPV) is carried out in this thesis. A full range of solar spectrum is recommended to use for all the simulation of CPV system as not only MJSC, but each material also has different properties as the wavelength varies. It is found that if only single wavelength is utilized in ray tracing simulation, it leads to overestimation of output power. The optical losses at each layer of the module are studied through computational breakdown analysis and the absorption of the CCPC lens made of dielectric material is found to be the most significant loss, which is 11.59%, following by the Fresnel reflection losses that occurs multiple times throughout the ray-tracing process. Besides, the performance of the CCPC lens is limited by the acceptance angle of the lens itself in which the optical efficiency drastically worsens even though it has not reached the acceptance angle of 37.77° . The optical efficiency of the CCPC-CPV assembly module is 77.3% after considered all the predicted losses. On the other side, a SCR of 4.65 is obtained through the combination of ray-tracing simulation and numerical analysis. The simulated optical efficiency is 77.4% (4.65 out of GCR of 5.998) in which it is tally to the optical efficiency of 77.3% computed through the breakdown

analysis. This shows that the algorithm and ray-tracing technique used in this work is presenting a highly reliable and promising accuracy.

Next, the performance of the CCPC-CPV assembly module under various practical scenarios is studied through experiments. For indoor measurement, it yields an optical efficiency of 76.2% (4.57 out of GCR of 5.998). Meanwhile, the outdoor measurement indicates that the CCPC-CPV assembly module can achieve an effective efficiency of 74.7% (4.48 out of GCR of 5.998) under real working condition.

Last but not least, the ray-tracing simulation for the whole UHCPV system shows that with the aid of secondary optics, the CPV system is able achieve SCR of 1144.3 suns.

5.2 Recommended future work

The geometry of the CCPC lens used in this work is designed to match the dimension of the CPV cell used as receiver, other sizes and different types of materials can be studied in future to minimize the absorption loss as it contributes to the greatest part of the losses. Currently, the ARCs applied on top of MJSC are optimized for the interface of air and glass, however based on the study in which the MJSC is bonded to the optical adhesive; future research might be needed on ARC that is optimized for the interface of optical adhesive.

The purpose of this thesis is to study the optical characteristics of CCPC lens as the SOE in a CPV system. The next step of this study should be

expanded to the integration of POE and SOE to determine the overall performance of the whole UHCPV system in detailed.

REFERENCES

- Algora, C. and Rey-Stolle (2012) *Next Generation of Photovoltaics*. Edited by A. B. C. L. A. M. V. A. L. López. Berlin: Springer.
- Azur Space (2015) *Concentrator Triple Junction Solar Cell Cell Datasheet*.
- Baig, H. *et al.* (2014) ‘Performance analysis of a dielectric based 3D building integrated concentrating photovoltaic system’, *Solar Energy*, 103, pp. 525–540. doi: 10.1016/j.solener.2014.03.002.
- Baig, H., Sellami, N. and Mallick, T. K. (2015) ‘Trapping light escaping from the edges of the optical element in a Concentrating Photovoltaic system’, *Energy Conversion and Management*, 90, pp. 238–246. doi: 10.1016/j.enconman.2014.11.026.
- Boeing Aerospace Co. (1987) *Light Funnel Concentrator Panel for Solar Power*.
- Brewster and Sir David (1817) ‘British Patent Specification No. 4136’.
- Burgess, E. L. and Pritchard, D. A. (1978) ‘Performance of a one kilowatt concentrator photovoltaic array utilizing active cooling’, *Photovoltaic Specialists Conference, 13th*, pp. 1121–1124.
- Chen, Y.-C., Chiang, H.-W. and Hsieh, W.-H. (2015) ‘Design of the Secondary Optical Elements for Concentrated Photovoltaic Units with Fresnel Lenses’, *Appl. Sci*, 5, pp. 770–786. doi: 10.3390/app5040770.
- Chong, K. *et al.* (2017) ‘Dense-array concentrator photovoltaic prototype using non-imaging dish concentrator and an array of cross compound parabolic

concentrators'. doi: 10.1016/j.apenergy.2017.03.108.

Chong, K. K. *et al.* (2012) 'Solar concentrator assembly'. Malaysian Patent No. PI 2012002439.

Chong, K. K. *et al.* (2013) 'Solar concentrator assembly'. US Patent Application Publication US2013/0319506.

Chong, K. K., Yew, T. K. and Tan, M. H. (2015) 'Dense-array concentrator photovoltaic system utilising non-imaging dish concentrator and array-of crossed compound parabolic concentrators'. US Patent Application Publication US2015/0207455.

Cooper, T. *et al.* (2013) 'Performance of compound parabolic concentrators with polygonal apertures', *SOLAR ENERGY*, 95, pp. 308–318. doi: 10.1016/j.solener.2013.06.023.

Couny, F., Benabid, F. and Light, P. S. (2007) 'Reduction of Fresnel back-reflection at splice interface between hollow core PCF and single-mode fiber', *IEEE Photonics Technology Letters*, 19(13), pp. 1020–1022. doi: 10.1109/LPT.2007.898770.

Dai, G. *et al.* (2011) 'Numerical investigation of the solar concentrating characteristics of 3D CPC and CPC-DC', *Solar Energy*, 85(11), pp. 2833–2842. doi: 10.1016/j.solener.2011.08.022.

Dai, G. L. *et al.* (2011) 'Numerical investigation of the solar concentrating characteristics of 3D CPC and CPC-DC', *Solar Energy*, 85(11), pp. 2833–2842. doi: 10.1016/j.solener.2011.08.022.

El-yahyaoui, S. *et al.* (2019) ‘Indoor characterization of pyramid- and cone-type secondary optics’, *AIP Conference Proceedings*, 070003(August).

Ferrer-Rodriguez, J. P. *et al.* (2016) ‘Optical Design of a 4-Off-Axis-Unit Cassegrain Ultra- High CPV Module with Central Receiver’, *Optics Letters*, 41, pp. 3–6.

Fu, L., Leutz, R. and Annen, H. P. (2010) ‘Secondary optics for Fresnel lens solar concentrators’, *Nonimaging Optics: Efficient Design for Illumination and Solar Concentration VII*, 7785, p. 778509. doi: 10.1117/12.860438.

Gao, C. and Chen, F. (2020) ‘Model building and optical performance analysis on a novel designed compound parabolic concentrator’, *Energy Conversion and Management*, 209(February), p. 112619. doi: 10.1016/j.enconman.2020.112619.

Green, M. A. *et al.* (2015) ‘Solar cell efficiency tables (version 46)’, *Progress in Photovoltaics: Research and Applications*, (version 46), pp. 805–812. doi: 10.1002/pip.

Hernández, M. *et al.* (2008) ‘High-performance Köhler concentrators with uniform irradiance on solar cell’, *Nonimaging Optics and Efficient Illumination Systems V*, 7059, pp. 1–9. doi: 10.1117/12.794927.

Hoffschmidt, B. *et al.* (2012) ‘3.06 - High Concentration Solar Collectors’, *Comprehensive Renewable Energy*, 3, pp. 165–209.

James and W, L. (1989) ‘Use of imaging refractive secondaries in photovoltaic concentrators’, in *NASA STI/Recon Technical Report N*, p. 29833.

- Kabir, E. *et al.* (2017) ‘Solar energy : Potential and future prospects’, *Renewable and Sustainable Energy Reviews*, 82, pp. 894–900. doi: 10.1016/j.rser.2017.09.094.
- Kaiyan, H., Hongfei, Z. and Tao, T. (2011) ‘A novel multiple curved surfaces compound concentrator’, *Solar Energy*, 85(3), pp. 523–529. doi: 10.1016/j.solener.2010.12.019.
- King, D. L. *et al.* (2000) ‘Photovoltaic module performance and durability following long-term field exposure’, *Progress in Photovoltaics: Research and Applications*, 8(2), pp. 241–256.
- Kreske, K. (2002) ‘Optical design of a solar flux homogenizer for concentrator photovoltaics’, *Optical Society of American (OSA)*, 41(10), pp. 2053–2058.
- Kussul, E. *et al.* (2008) ‘Micro-facet solar concentrator’, *International Journal of Sustainable Energy*, 27(June), pp. 61–71. doi: 10.1080/14786450802264851.
- Languy, F. and Habraken, S. (2013) ‘Nonimaging achromatic shaped Fresnel lenses for ultrahigh solar concentration’, *Optical Society of America*, 38(10), pp. 1730–1732.
- Lee, P. S. *et al.* (2019) ‘Optical and Electrical Performance Evaluation of the Crossed Compound Parabolic Concentrator Module for the Application of Ultra- High Concentrator Photovoltaic System Optical and Electrical Performance Evaluation of the Crossed Compound Parabolic Concentrator’, in *International Conference on Sustainable Energy and Green Technology 2018*. doi: 10.1088/1755-1315/268/1/012031.
- Luque, A., Sala, G. and Ignacio Luque-Heredia (2006) ‘Photovoltaic

Concentration at the Onset of its Commercial Deployment’, *Progress in Photovoltaics Research and Applications*, 14(5), pp. 413–428.

Mammo, E. D., Sellami, N. and Mallick, T. K. (2012) ‘Performance analysis of a reflective 3D crossed compound parabolic concentrating photovoltaic system for building façade integration’, *Progress in Photovoltaics: Research and Applications*, 21, pp. 1095–1103. doi: 10.1002/pip.

Newport Corporation (2011) *Technical Notes: Solar Simulator Standards – Definitions & Comparisons*. CA.

Pérez-Higueras, P. *et al.* (2015) ‘Thin photovoltaic modules at ultra high concentration’, *AIP -11th International Conference on Concentrator Photovoltaic Systems*, 130004(1679), p. 130004. doi: 10.1063/1.4931564.

Ries, H., Gordon, J. M. and Lasken, M. (1997) ‘High-flux photovoltaic solar concentrators with kaleidoscope-based optical designs’, *Solar Energy*, 60(1), pp. 11–16. doi: 10.1016/S0038-092X(96)00159-4.

Sahin, F. E. and Yilmaz, M. (2019) ‘High Concentration Photovoltaics (HCPV) with Diffractive Secondary Optical Elements’, *Photonics*, 6(2). doi: 10.3390/photonics6020068.

Sankawa, I. *et al.* (1986) ‘Methods for reducing the fresnel reflection in an optical-fiber connector with index matching material’, *Electronics and Communications in Japan (Part I: Communications)*, 69(1), pp. 94–102. doi: 10.1002/ecja.4410690111.

Schott Corp. (1993) *Specification Part A: Physical and chemical properties of B270 Superwhite*.

Sellami, N. and Mallick, T. K. (2013) ‘Optical efficiency study of PV Crossed Compound Parabolic Concentrator’, *Applied Energy*, 102, pp. 868–876. doi: 10.1016/j.apenergy.2012.08.052.

Sellami, N., Mallick, T. K. and Mcneil, D. (2010) ‘Optical performance modelling of an atypical 3-D Cross Compound Parabolic Photovoltaic Concentrator using ray trace technique’, *Research Gate*, (May 2016). doi: 10.13140/2.1.3960.1927.

Shanks, K. *et al.* (2018) ‘A >3000 suns high concentrator photovoltaic design based on multiple Fresnel lens primaries focusing to one central solar cell’, *Solar Energy*, 169(November 2017), pp. 457–467. doi: 10.1016/j.solener.2018.05.016.

Shanks, K., Senthilarasu, S. and Mallick, T. K. (2016) ‘Optics for concentrating photovoltaics : Trends , limits and opportunities for materials and design’, *Renewable and Sustainable Energy Reviews*, 60, pp. 394–407. doi: 10.1016/j.rser.2016.01.089.

Solanki, C. S. *et al.* (2008) ‘Enhanced heat dissipation of V-trough PV modules for better performance’, *Solar Energy Materials and Solar Cells*, 92(12), pp. 1634–1638. doi: 10.1016/j.solmat.2008.07.022.

Su, Y. *et al.* (2012) ‘Radiance / Pmap simulation of a novel lens-walled compound parabolic concentrator (lens-walled CPC)’, *Energy Procedia*, 14, pp. 572–577. doi: 10.1016/j.egypro.2011.12.977.

Su, Y., Riffat, S. B. and Pei, G. (2012) ‘Comparative study on annual solar energy collection of a novel lens-walled compound parabolic concentrator

(lens-walled CPC)’, *Sustainable Cities and Society*, 4, pp. 35–40. doi: 10.1016/j.scs.2012.05.001.

Swanson, R. M. (2000) ‘The promise of concentrators’, *Progress in Photovoltaics: Research and Applications*, 8(1), pp. 93–111.

Tang, R. and Liu, X. (2011) ‘Optical performance and design optimization of V-trough concentrators for photovoltaic applications’, *Solar Energy*, 85(9), pp. 2154–2166. doi: 10.1016/j.solener.2011.06.001.

Tsao, J., Lewis, N. and Crabtree, G. (2006) *Solar FAQs*. US.

Victoria, M., Dom, C. and Ant, I. (2009) ‘Comparative analysis of different secondary optical elements for aspheric primary lenses’, *Optical Society of American (OSA)*, 17(8), pp. 6487–6492.

Welford, W. T. and Winston, R. (1978) *The Optics of Nonimaging Concentrators: Light and Solar Energy*. New York: Academic Press.

Winston, R., Miñano, J. C. and Benitez, P. G. (2005) *Nonimaging Optics*. US: Elsevier Inc.

Wong, C. *et al.* (2017) ‘Design optimization of ultra-high concentrator photovoltaic system using two-stage non-imaging solar concentrator Design optimization of ultra-high concentrator photovoltaic system using two-stage non-imaging solar concentrator’, *IOP Conference Series: Earth and Environmental Science*, 93.

Yew, T., Chong, K. and Lim, B. (2015) ‘Performance study of crossed compound parabolic concentrator as secondary optics in non-imaging dish

concentrator for the application of dense-array concentrator photovoltaic system', *Solar Energy*, 120, pp. 296–309. doi: 10.1016/j.solener.2015.07.026.

Yew, T. K. (2016) *Design and optical evaluation of secondary optics for optimizing electrical performance of dense-array concentrator photovoltaic system*. Universiti Tunku Abdul Rahman.

Yew, T. K., Chong, K. K. and Lim, B. H. (2015) 'Performance study of crossed compound parabolic concentrator as secondary optics in non-imaging dish concentrator for the application of dense-array concentrator photovoltaic system', *Solar Energy*, 120, pp. 296–309. doi: 10.1016/j.solener.2015.07.026.

Zheng, H. *et al.* (2014) 'Combination of a light funnel concentrator with a deflector for orientated sunlight transmission', *Energy Conversion and Management*, 88, pp. 785–793. doi: 10.1016/j.enconman.2014.09.004.

Zubi, G., Bernal-Agustín, J. L. and Fracastoro, G. V. (2009) 'High concentration photovoltaic systems applying III–V cells', *Renewable and Sustainable Energy Reviews*, 13(9), pp. 2645–2652.

PUBLICATIONS

Based on findings from this work, two paper has been published. One in International Conference on Sustainable Energy and Green Technology, and the other one in Applied Optics. The full published papers can be seen at the appendix D and E.

[1] P. S. Lee et al., “Optical and Electrical Performance Evaluation of the Crossed Compound Parabolic Concentrator Module for the Application of Ultra-High Concentrator Photovoltaic System,” IOP Conf. Ser. Earth Environ. Sci., vol. 268, no. 1, 2019, doi: 10.1088/1755-1315/268/1/012031.

[2] P.-S. Lee, C.-W. Wong, M.-H. Tan, and K.-K. Chong, “Comprehensive analysis on the assembly of a dielectric-filled crossed compound parabolic concentrator and a concentrator photovoltaic module,” Appl. Opt., vol. 59, no. 14, p. 4557, 2020, doi: 10.1364/ao.387965Algora, C. and Rey-Stolle (2012) *Next Generation of Photovoltaics*. Edited by A. B. C. L. A. M. V. A. L. López. Berlin: Springer.

Azur Space (2015) *Concentrator Triple Junction Solar Cell Cell Datasheet*.

Baig, H. *et al.* (2014) ‘Performance analysis of a dielectric based 3D building integrated concentrating photovoltaic system’, *Solar Energy*, 103, pp. 525–540. doi: 10.1016/j.solener.2014.03.002.

Baig, H., Sellami, N. and Mallick, T. K. (2015) ‘Trapping light escaping from the edges of the optical element in a Concentrating Photovoltaic system’, *Energy Conversion and Management*, 90, pp. 238–246. doi:

10.1016/j.enconman.2014.11.026.

Boeing Aerospace Co. (1987) *Light Funnel Concentrator Panel for Solar Power*.

Brewster and Sir David (1817) 'British Patent Specification No. 4136'.

Burgess, E. L. and Pritchard, D. A. (1978) 'Performance of a one kilowatt concentrator photovoltaic array utilizing active cooling', *Photovoltaic Specialists Conference, 13th*, pp. 1121–1124.

Chen, Y.-C., Chiang, H.-W. and Hsieh, W.-H. (2015) 'Design of the Secondary Optical Elements for Concentrated Photovoltaic Units with Fresnel Lenses', *Appl. Sci*, 5, pp. 770–786. doi: 10.3390/app5040770.

Chong, K. *et al.* (2017) 'Dense-array concentrator photovoltaic prototype using non-imaging dish concentrator and an array of cross compound parabolic concentrators'. doi: 10.1016/j.apenergy.2017.03.108.

Chong, K. K. *et al.* (2012) 'Solar concentrator assembly'. Malaysian Patent No. PI 2012002439.

Chong, K. K. *et al.* (2013) 'Solar concentrator assembly'. US Patent Application Publication US2013/0319506.

Chong, K. K., Yew, T. K. and Tan, M. H. (2015) 'Dense-array concentrator photovoltaic system utilising non-imaging dish concentrator and array-of crossed compound parabolic concentrators'. US Patent Application Publication US2015/0207455.

Cooper, T. *et al.* (2013) 'Performance of compound parabolic concentrators

with polygonal apertures’, *SOLAR ENERGY*, 95, pp. 308–318. doi:
10.1016/j.solener.2013.06.023.

Couny, F., Benabid, F. and Light, P. S. (2007) ‘Reduction of Fresnel back-reflection at splice interface between hollow core PCF and single-mode fiber’, *IEEE Photonics Technology Letters*, 19(13), pp. 1020–1022. doi:
10.1109/LPT.2007.898770.

Dai, G. *et al.* (2011) ‘Numerical investigation of the solar concentrating characteristics of 3D CPC and CPC-DC’, *Solar Energy*, 85(11), pp. 2833–2842. doi: 10.1016/j.solener.2011.08.022.

Dai, G. L. *et al.* (2011) ‘Numerical investigation of the solar concentrating characteristics of 3D CPC and CPC-DC’, *Solar Energy*, 85(11), pp. 2833–2842. doi: 10.1016/j.solener.2011.08.022.

El-yahyaoui, S. *et al.* (2019) ‘Indoor characterization of pyramid- and cone-type secondary optics’, *AIP Conference Proceedings*, 070003(August).

Ferrer-Rodriguez, J. P. *et al.* (2016) ‘Optical Design of a 4-Off-Axis-Unit Cassegrain Ultra- High CPV Module with Central Receiver’, *Optics Letters*, 41, pp. 3–6.

Fu, L., Leutz, R. and Annen, H. P. (2010) ‘Secondary optics for Fresnel lens solar concentrators’, *Nonimaging Optics: Efficient Design for Illumination and Solar Concentration VII*, 7785, p. 778509. doi: 10.1117/12.860438.

Gao, C. and Chen, F. (2020) ‘Model building and optical performance analysis on a novel designed compound parabolic concentrator’, *Energy Conversion and Management*, 209(February), p. 112619. doi:

10.1016/j.enconman.2020.112619.

Green, M. A. *et al.* (2015) ‘Solar cell efficiency tables (version 46)’, *Progress in Photovoltaics: Research and Applications*, (version 46), pp. 805–812. doi: 10.1002/pip.

Hernández, M. *et al.* (2008) ‘High-performance Köhler concentrators with uniform irradiance on solar cell’, *Nonimaging Optics and Efficient Illumination Systems V*, 7059, pp. 1–9. doi: 10.1117/12.794927.

Hoffschmidt, B. *et al.* (2012) ‘3.06 - High Concentration Solar Collectors’, *Comprehensive Renewable Energy*, 3, pp. 165–209.

James and W, L. (1989) ‘Use of imaging refractive secondaries in photovoltaic concentrators’, in *NASA STI/Recon Technical Report N*, p. 29833.

Kabir, E. *et al.* (2017) ‘Solar energy : Potential and future prospects’, *Renewable and Sustainable Energy Reviews*, 82, pp. 894–900. doi: 10.1016/j.rser.2017.09.094.

Kaiyan, H., Hongfei, Z. and Tao, T. (2011) ‘A novel multiple curved surfaces compound concentrator’, *Solar Energy*, 85(3), pp. 523–529. doi: 10.1016/j.solener.2010.12.019.

King, D. L. *et al.* (2000) ‘Photovoltaic module performance and durability following long-term field exposure’, *Progress in Photovoltaics: Research and Applications*, 8(2), pp. 241–256.

Kreske, K. (2002) ‘Optical design of a solar flux homogenizer for concentrator photovoltaics’, *Optical Society of American (OSA)*, 41(10), pp. 2053–2058.

Kussul, E. *et al.* (2008) 'Micro-facet solar concentrator', *International Journal of Sustainable Energy*, 27(June), pp. 61–71. doi: 10.1080/14786450802264851.

Languy, F. and Habraken, S. (2013) 'Nonimaging achromatic shaped Fresnel lenses for ultrahigh solar concentration', *Optical Society of America*, 38(10), pp. 1730–1732.

Lee, P. S. *et al.* (2019) 'Optical and Electrical Performance Evaluation of the Crossed Compound Parabolic Concentrator Module for the Application of Ultra- High Concentrator Photovoltaic System Optical and Electrical Performance Evaluation of the Crossed Compound Parabolic Concentrator', in *International Conference on Sustainable Energy and Green Technology 2018*. doi: 10.1088/1755-1315/268/1/012031.

Luque, A., Sala, G. and Ignacio Luque-Heredia (2006) 'Photovoltaic Concentration at the Onset of its Commercial Deployment', *Progress in Photovoltaics Research and Applications*, 14(5), pp. 413–428.

Mammo, E. D., Sellami, N. and Mallick, T. K. (2012) 'Performance analysis of a reflective 3D crossed compound parabolic concentrating photovoltaic system for building façade integration', *Progress in Photovoltaics: Research and Applications*, 21, pp. 1095–1103. doi: 10.1002/pip.

Newport Corporation (2011) *Technical Notes: Solar Simulator Standards – Definitions & Comparisons*. CA.

Pérez-Higueras, P. *et al.* (2015) 'Thin photovoltaic modules at ultra high concentration', *AIP -11th International Conference on Concentrator Photovoltaic Systems*, 130004(1679), p. 130004. doi: 10.1063/1.4931564.

Ries, H., Gordon, J. M. and Lasken, M. (1997) 'High-flux photovoltaic solar concentrators with kaleidoscope-based optical designs', *Solar Energy*, 60(1), pp. 11–16. doi: 10.1016/S0038-092X(96)00159-4.

Sahin, F. E. and Yilmaz, M. (2019) 'High Concentration Photovoltaics (HCPV) with Diffractive Secondary Optical Elements', *Photonics*, 6(2). doi: 10.3390/photonics6020068.

Sankawa, I. *et al.* (1986) 'Methods for reducing the fresnel reflection in an optical-fiber connector with index matching material', *Electronics and Communications in Japan (Part I: Communications)*, 69(1), pp. 94–102. doi: 10.1002/ecja.4410690111.

Schott Corp. (1993) *Specification Part A: Physical and chemical properties of B270 Superwite*.

Sellami, N. and Mallick, T. K. (2013) 'Optical efficiency study of PV Crossed Compound Parabolic Concentrator', *Applied Energy*, 102, pp. 868–876. doi: 10.1016/j.apenergy.2012.08.052.

Sellami, N., Mallick, T. K. and Mcneil, D. (2010) 'Optical performance modelling of an atypical 3-D Cross Compound Parabolic Photovoltaic Concentrator using ray trace technique', *Research Gate*, (May 2016). doi: 10.13140/2.1.3960.1927.

Shanks, K. *et al.* (2018) 'A >3000 suns high concentrator photovoltaic design based on multiple Fresnel lens primaries focusing to one central solar cell', *Solar Energy*, 169(November 2017), pp. 457–467. doi: 10.1016/j.solener.2018.05.016.

- Shanks, K., Senthilarasu, S. and Mallick, T. K. (2016) 'Optics for concentrating photovoltaics : Trends , limits and opportunities for materials and design', *Renewable and Sustainable Energy Reviews*, 60, pp. 394–407. doi: 10.1016/j.rser.2016.01.089.
- Solanki, C. S. *et al.* (2008) 'Enhanced heat dissipation of V-trough PV modules for better performance', *Solar Energy Materials and Solar Cells*, 92(12), pp. 1634–1638. doi: 10.1016/j.solmat.2008.07.022.
- Su, Y. *et al.* (2012) 'Radiance / Pmap simulation of a novel lens-walled compound parabolic concentrator (lens-walled CPC)', *Energy Procedia*, 14, pp. 572–577. doi: 10.1016/j.egypro.2011.12.977.
- Su, Y., Riffat, S. B. and Pei, G. (2012) 'Comparative study on annual solar energy collection of a novel lens-walled compound parabolic concentrator (lens-walled CPC)', *Sustainable Cities and Society*, 4, pp. 35–40. doi: 10.1016/j.scs.2012.05.001.
- Swanson, R. M. (2000) 'The promise of concentrators', *Progress in Photovoltaics: Research and Applications*, 8(1), pp. 93–111.
- Tang, R. and Liu, X. (2011) 'Optical performance and design optimization of V-trough concentrators for photovoltaic applications', *Solar Energy*, 85(9), pp. 2154–2166. doi: 10.1016/j.solener.2011.06.001.
- Tsao, J., Lewis, N. and Crabtree, G. (2006) *Solar FAQs*. US.
- Victoria, M., Dom, C. and Ant, I. (2009) 'Comparative analysis of different secondary optical elements for aspheric primary lenses', *Optical Society of American (OSA)*, 17(8), pp. 6487–6492.

- Welford, W. T. and Winston, R. (1978) *The Optics of Nonimaging Concentrators: Light and Solar Energy*. New York: Academic Press.
- Winston, R., Miñano, J. C. and Benitez, P. G. (2005) *Nonimaging Optics*. US: Elsevier Inc.
- Wong, C. *et al.* (2017) 'Design optimization of ultra-high concentrator photovoltaic system using two-stage non-imaging solar concentrator Design optimization of ultra-high concentrator photovoltaic system using two-stage non-imaging solar concentrator', *IOP Conference Series: Earth and Environmental Science*, 93.
- Yew, T., Chong, K. and Lim, B. (2015) 'Performance study of crossed compound parabolic concentrator as secondary optics in non-imaging dish concentrator for the application of dense-array concentrator photovoltaic system', *Solar Energy*, 120, pp. 296–309. doi: 10.1016/j.solener.2015.07.026.
- Yew, T. K. (2016) *Design and optical evaluation of secondary optics for optimizing electrical performance of dense-array concentrator photovoltaic system*. Universiti Tunku Abdul Rahman.
- Yew, T. K., Chong, K. K. and Lim, B. H. (2015) 'Performance study of crossed compound parabolic concentrator as secondary optics in non-imaging dish concentrator for the application of dense-array concentrator photovoltaic system', *Solar Energy*, 120, pp. 296–309. doi: 10.1016/j.solener.2015.07.026.
- Zheng, H. *et al.* (2014) 'Combination of a light funnel concentrator with a deflector for orientated sunlight transmission', *Energy Conversion and Management*, 88, pp. 785–793. doi: 10.1016/j.enconman.2014.09.004.

Zubi, G., Bernal-Agustín, J. L. and Fracastoro, G. V. (2009) 'High concentration photovoltaic systems applying III–V cells', *Renewable and Sustainable Energy Reviews*, 13(9), pp. 2645–2652.

*Note: Some data and figures in the above papers have been repeated in this thesis as the publications are from the same research described in this thesis and both papers are written by the author of this thesis.

APPENDIX A

B270 SCHOTT GLASS

SCHOTT DESAG

SCHOTT

Specification Physical and chemical properties	PCE - TKT B 270 Superwite		
<table><tr><td data-bbox="536 763 772 792">B 270 Superwite</td><td data-bbox="1129 763 1225 792">D 0092</td></tr></table> <p data-bbox="536 846 995 913">B 270 Superwite is a clear high transmission crown glass (modified soda-lime glass) available in form of sheets, optical rods, profiled rods and strips.</p> <p data-bbox="536 1503 1362 1599">The subsequent properties are based primarily upon the measuring results of the very latest standards and measuring methods, which are defined in corresponding "Measuring and Test Procedures". SCHOTT DESAG retains the right to change the data in keeping with the latest technical standards. Non-toleranced numerical values are reference values of an average production quality.</p> <p data-bbox="536 1630 1190 1653">Values marked with \emptyset do not apply to the type of glass or no values are available.</p> <p data-bbox="536 1682 1372 1704">Requirements deviating from these specifications must be defined in writing in a customer agreement.</p> <p data-bbox="536 1760 858 1783">Date of release: May 02, 00</p>		B 270 Superwite	D 0092
B 270 Superwite	D 0092		

Form 00506A

04.00/1

page: 1 to 14

Specification		PCE - TKT	
Physical and chemical properties		B 270 Superwite	
1.	Optical properties		
1.1	Refractive indices (20°C)		
	Pretreatment of samples	n_g	1.5341
	annealed at 40°C/h	n_F	1.5297
		n_F	1.5292
		n_e	1.5251 ± 0.001*
		n_d	1.5230
		n_D	1.5229
	* ± 0.0003 upon request	n_C	1.5207
		n_C	1.5203
	Further refractive indices in UV and IR (reference values)	see annex	
1.1.1	Abbe value	v_e	58.3 ± 0.6
		v_d	58.5
1.2	Transmittance data		
1.2.1	Spectral transmittance $\tau(\lambda)$		
1.2.1.1	$\tau(\lambda)$ - curve		
	Plot of spectral transmittance $\tau(\lambda)$ for		
	$d = 2.0$ mm und $d = 15$ mm ($\lambda = 280$ nm - 650 nm)	see annex	
	$d = 2.0$ mm und $d = 15$ mm ($\lambda = 280$ nm - 2000 nm)	see annex	
1.2.1.2	$\tau(\lambda)$ - individual values in %	see annex	
1.2.1.3	Edge wavelength ($d = 2.0$ mm)		
	Edge wavelength	λ_C ($\tau = 0.46$) in nm	312
	Solarization refer to 6.2		
	Additional data	λ_B ($\tau = 0.05$) in nm	294
		λ_P ($\tau = 0.85$) in nm	340
1.2.2	Luminous transmittance τ_v		
1.2.2.1	Luminous transmittance as a function of thickness		
		thickness in mm	τ_{vDES} in %
		2.0	91.7
		4.0	91.6
		15.0	91.0
			τ_{vA} in %
			91.7
			91.6
			91.0

Form 00506B

Specification		PCE - TKT	
Physical and chemical properties		B 270 Superwite	
1.2.3	Special transmittance values in % (d = 2.0 mm)		
1.2.3.1	UV - transmittance	τ_{UVA}	84
		τ_{UVB}	19
1.2.3.2	IR - transmittance	τ_A	92.5
1.2.3.3	Radiant transmittance	τ_e	91.4
1.3	Colour		
1.3.1	Visual evaluation	disregard	
1.3.2	Colorimetry (d = 2.0 mm)		
		D_{65} x	0.314
		y	0.332
	Chromaticity coordinates (colour locus) are referred to the named Standard Illuminant according to CIE 2°-observer	A x	0.448
		y	0.408
1.3.3			disregard
1.3.4	General colour rendering index R_a (d = 2.0 mm)		100

Form 005/06B

Specification		PCE - TKT	
Physical and chemical properties		B 270 Superwite	
2.	Thermal properties		
2.1	Viscosities and corresponding temperatures		
	Designation	Viscosity log η in dPas	Temperature ϑ in °C
	Strain point	14.5	511
	Annealing point	13.0	541
	Softening point	7.6	724
	Forming temperature	6.0	827
	Forming temperature	5.0	915
	Forming temperature	4.0	1033
2.2	Transformation temperature T_g in °C		533
2.3	Coefficient of thermal expansion α		
2.3.1	Coefficient of mean linear thermal expansion α in 10^{-8} K^{-1} for the indicated temperature range (static measurement)		
		α (20°C-300°C)	9.4
		α (20°C-200°C)	9.0
		α (20°C-100°C)	8.2
2.3.2	Coefficient of mean linear thermal expansion α in 10^{-8} K^{-1} for the indicated temperature range (dynamic measurement)		
		α (20°C-100°C)	7.8
		α (20°C-150°C)	8.4
		α (20°C-200°C)	8.8
		α (20°C-250°C)	9.1
		α (20°C-300°C)	9.4
		α (20°C-350°C)	9.6
		α (20°C-400°C)	9.8
		α (20°C-450°C)	10.0
		α (20°C-500°C)	10.3

Form 0050/6B

Specification		PCE - TKT B 270 Superwite	
Physical and chemical properties			
2.3.3	Coefficient of mean linear thermal expansion α in 10^{-8} K^{-1} for the mentioned temperature intervals (dynamic measurement)	see annex	
2.4	Fuseability Stress-free fusion with suitable SCHOTT DESAG lower segments is possible.		
2.5	Mean specific heat capacity c_p (20°C-100°C) in J/ (g·K)	0.86	
2.6	Thermal conductivity λ in W/ (m·K) for the indicated temperatures		
		$\vartheta = 24.5^\circ\text{C}$	0.92
		$\vartheta = 89^\circ\text{C}$	1.01
		$\vartheta = 127^\circ\text{C}$	1.08
		$\vartheta = 167^\circ\text{C}$	1.15
2.7	Specific thermal stress φ in N/ (mm ² ·K)	0.86	

Specification		PCE - TKT
Physical and chemical properties		B 270 Superwite
3.	Mechanical properties	
3.1	Density ρ in g/cm ³	2.55
3.2	Stress optical coefficient C in $1.02 \cdot 10^{-12}$ m ² /N	2.7
3.3	Breaking strength	
	Admissible value for the bending strength σ_{zu} of technically annealed glasses as calculation basis (air) in N/mm ²	30
	A higher mechanical strength can be realized by chemical toughening according to the ion exchange procedure (refer to annex 3.3.1) or by thermal toughening.	
3.3.1	Chemical toughening	
	Processing temperature ϑ in °C	420
	Processing time t in h	18
	Compressive stress D_s as birefringence in nm/cm	7200
	Penetration depth N_z up to neutral zone in μm	48
	Further information	see annex
3.3.2	Thermal toughening	
	Recommended minimum thickness d in mm for toughened safety glass for building purposes according to DIN 1249 T10 - 1990	4.0
3.4	Young's modulus E in kN/mm ²	71.5
3.5	Poisson's ratio μ	0.219
3.6	Torsion modulus G in kN/mm ²	29.3
3.7	Knoop hardness HK_{100}	542

Form 0050/6B

Specification		PCE - TKT	
Physical and chemical properties		B 270 Superwite	
4.	Chemical properties		
4.1	Hydrolytic resistance acc. to DIN ISO 719		
	Hydrolytic class	HGB 3	
	Equivalent of alkali (Na ₂ O) per gram of glass grains in µg/g	170	
4.2	Acid resistance acc. to DIN 12 116		
	Acid class	2	
	Half surface weight loss after 6 hours in mg/dm ²	1.4	
4.3	Alkali resistance acc. to DIN ISO 695		
	Class	A 2	
	Surface weight loss after 3 hours in mg/dm ²	140	
5.	Electrical properties		
5.1	Dielectric constant (Permittivity) ϵ_r at 1 MHz		7.0
5.2	Dissipation factor $\tan \delta$ bei 1 MHz		$30 \cdot 10^{-4}$
5.3	Electric volume resistivity ρ_D in $\Omega \cdot \text{cm}$ at the specified temperatures		
5.3.1	ρ_D for alternating current 50 Hz and 3 kHz		
	$\vartheta = 1260^\circ\text{C}$	10.2	
	$\vartheta = 1386^\circ\text{C}$	6.8	
5.3.2	ρ_D for direct current		
	$\vartheta = 250^\circ\text{C}$	10^9	
	$\vartheta = 350^\circ\text{C}$	$1.6 \cdot 10^7$	
	$\vartheta = 400^\circ\text{C}$	$2 \cdot 10^5$	
5.4	Temperature f_{k100} in $^\circ\text{C}$ for a specific electric volume resistivity of $10^8 \Omega \cdot \text{cm}$		301

Form 0050/6B

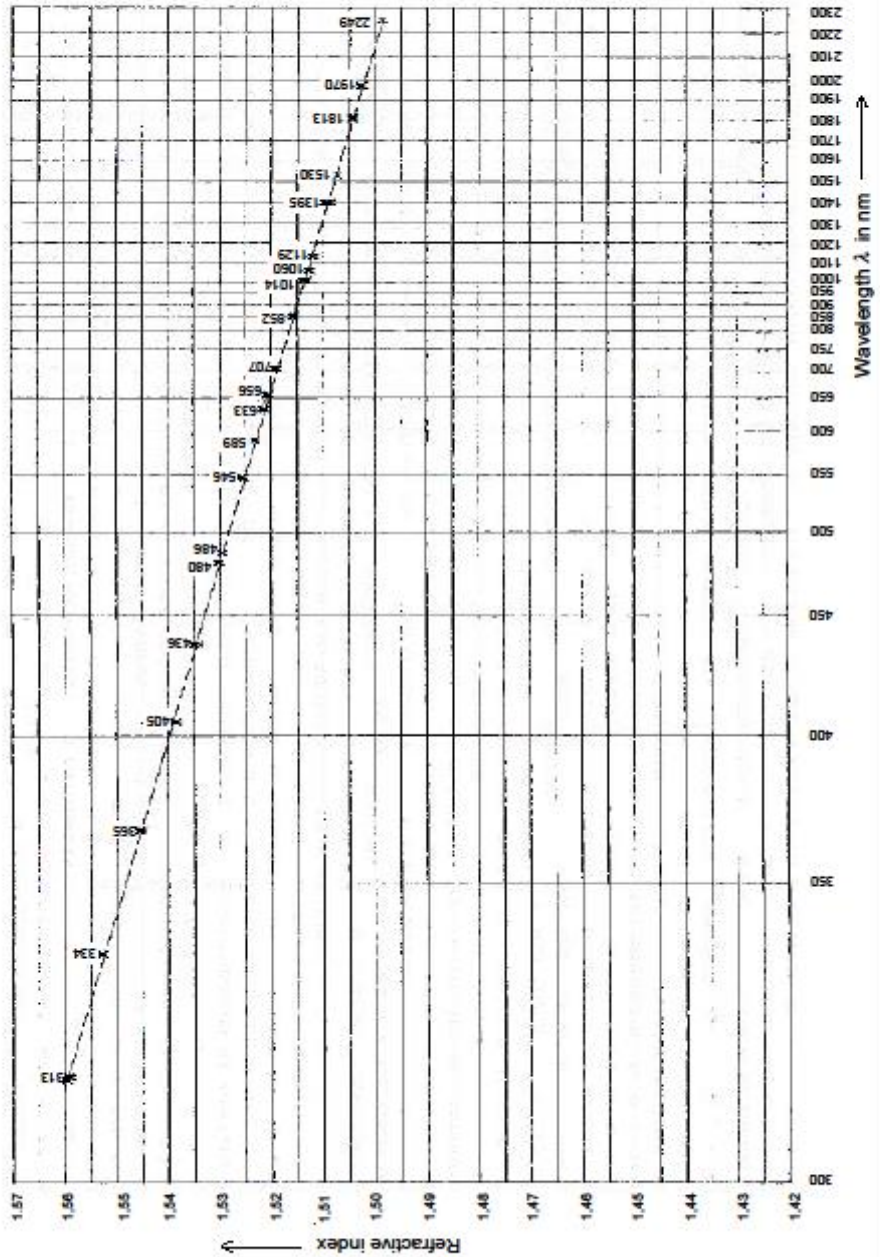
Specification		PCE - TKT
Physical and chemical properties		B 270 Superwite
6.	Other properties	
6.1	Lead equivalent in mm Pb at 15 mm glass thickness for X-rays	
	Voltage 50 kV/0.16 mm Cu total filtering	0.24
	Voltage 80 kV/0.16 mm Cu total filtering	0.32
	Voltage 110 kV/0.40 mm Cu total filtering	0.33
	Voltage 150 kV/0.70 mm Cu total filtering	0.27
	Measuring and Test Procedures	
	For X-radiation (constant voltage) the lead equivalent is defined by the total filtering specified in the table (refer also to DIN 6845). The exposed area has a diameter of 50 mm. The absorption of radiation in the sample piece is compared to lead absorbers of such a thickness that the same attenuation of the dose performance is reached in both cases. As detector, a scintillation dosimeter (scintillator 44 mm diameter, 15 mm height) is used. The measuring inaccuracy is ± 0.03 mm.	
6.2	Solarization	
	Shifting of the edge wavelength λ_c ($\tau = 0.46$) after UV-radiation in the direction of longer wavelength	$\Delta \lambda_c$ in nm
		2
	Measuring and Test Procedures	
	The sample will be irradiated with a UV - F 400 floodlamp. The irradiation time amounts to 7h; the distance between floodlamp and samplefastening is 14 cm.	
7.	Annex (diagrams, curves)	

Form 00 50/6B

Annex 1.1

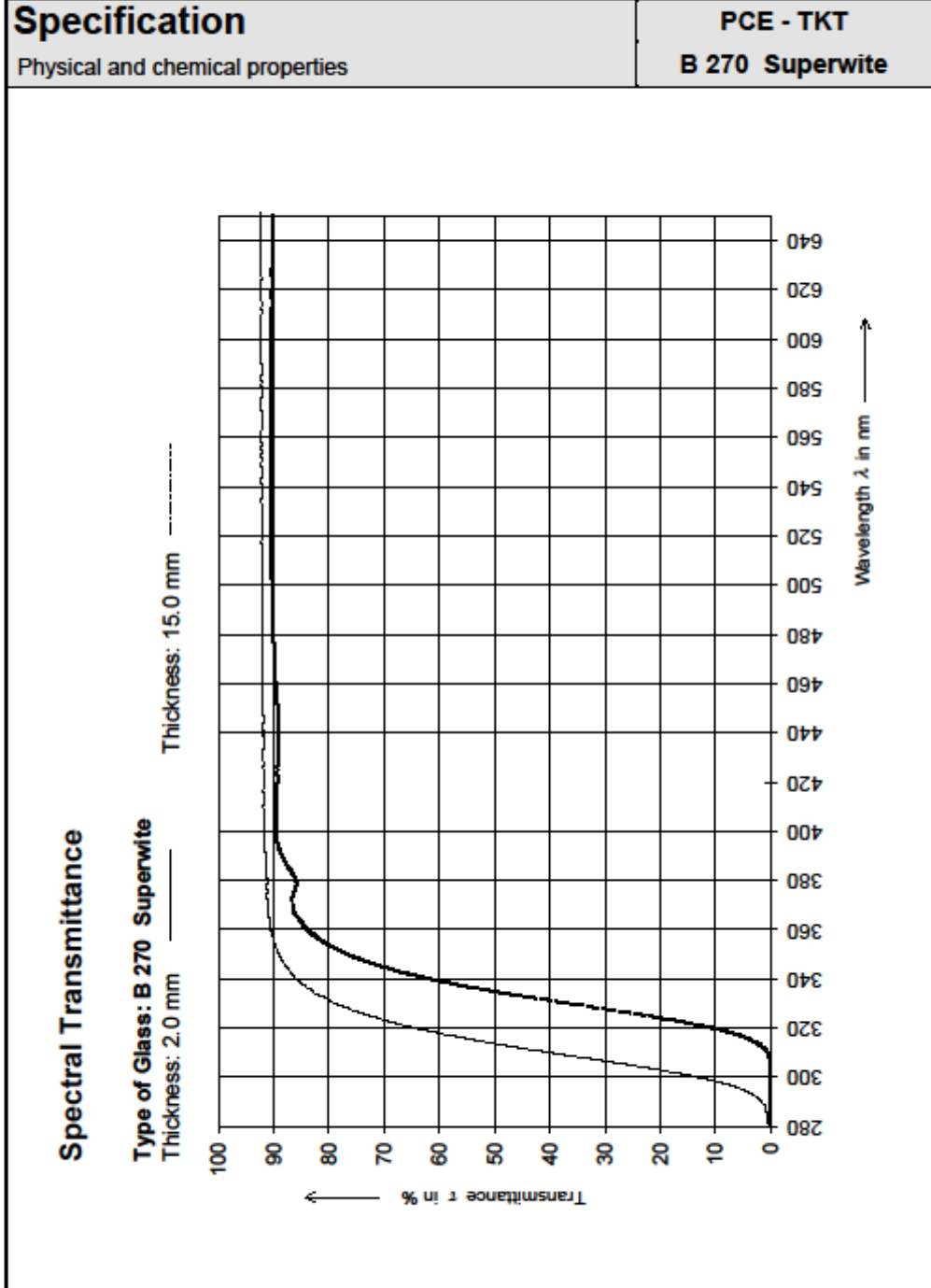
Specification	PCE - TKT
Physical and chemical properties	B 270 Superwite

Refractive indices of B 270 Superwite in relationship to the wavelength

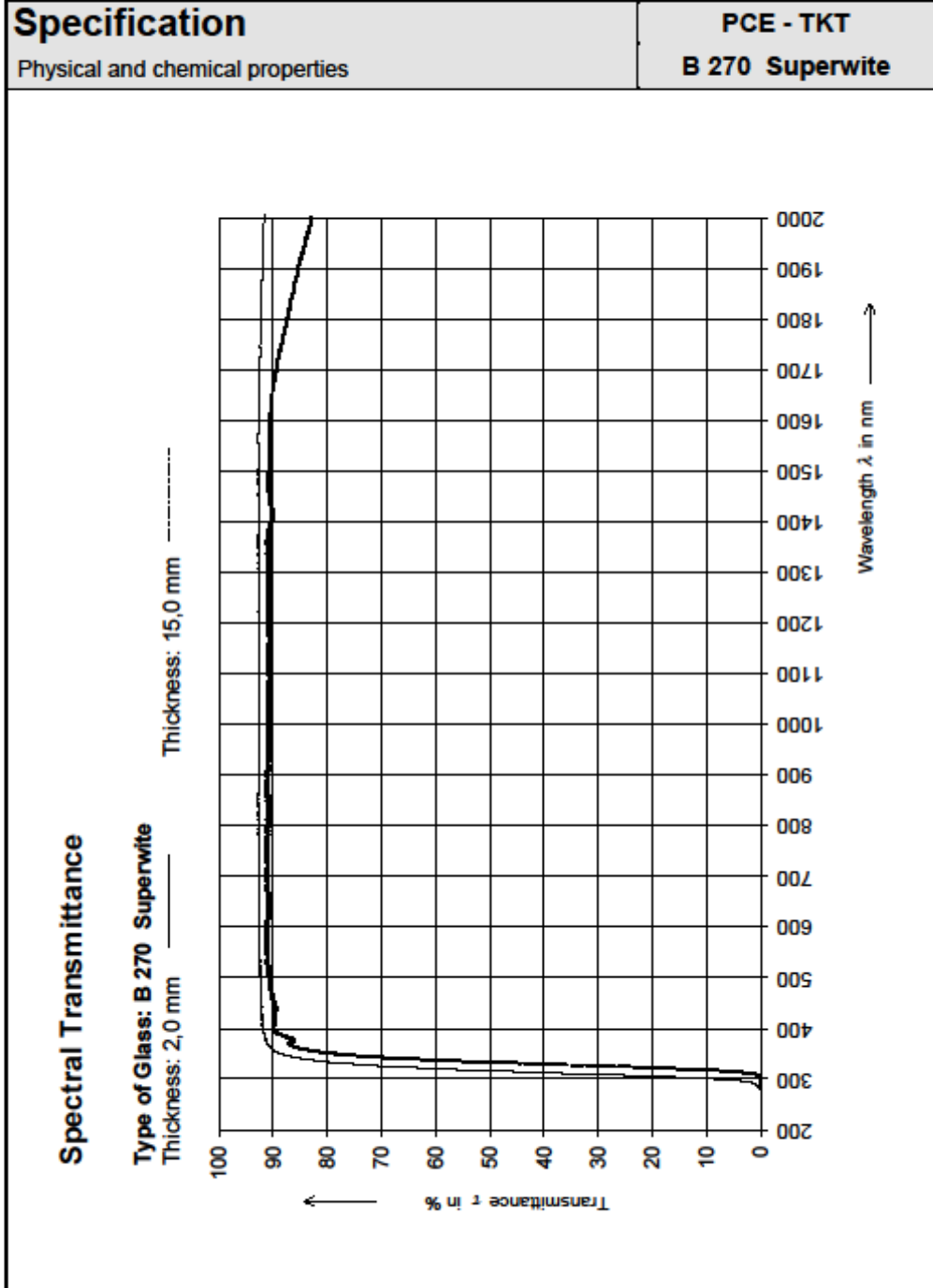


Form 0050/6B

Annex 1.2.1.1



Annex 1.2.1.1



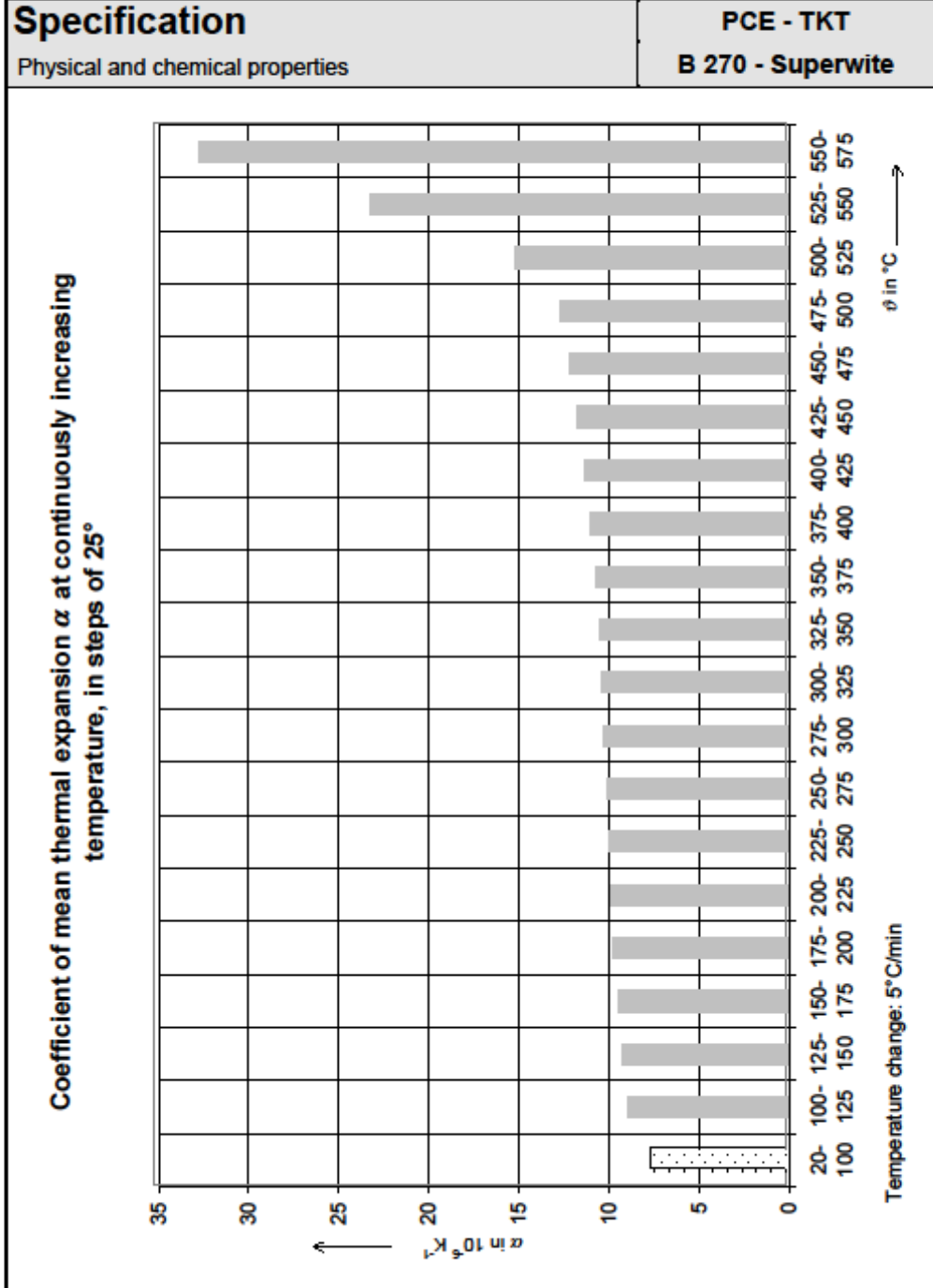
Form 0050/68

Annex 1.2.1.2

Specification		PCE - TKT B 270 Superwite													
Physical and chemical properties															
Spectral transmittance τ (λ) in % for the named thickness															
λ in nm	thickness in mm														
	1	2	3	4	5	6	7	8	9	10	15	20	25	30	
300	35.1	13.5	5.2	2.0	0.8	0.3	0.1	0.0	0.0	0.0					
310	60.0	39.6	26.1	17.2	11.4	7.5	4.9	3.3	2.2	1.4					
320	76.0	63.4	52.9	44.1	36.8	30.7	25.6	21.4	17.8	14.9	10.9	5.4	2.6	1.3	
330	84.2	77.8	71.8	66.3	61.3	56.6	52.3	48.3	44.6	41.2	34.6	25.0	18.1	13.1	
340	88.0	84.9	81.9	79.0	76.3	73.6	71.0	68.5	66.1	63.8	59.6	51.8	44.9	39.0	
350	89.8	88.4	87.1	85.7	84.4	83.1	81.8	80.6	79.3	78.1	75.1	70.4	65.9	61.8	
360	90.6	89.9	89.2	88.5	87.9	87.2	86.5	85.9	85.2	84.6	83.0	80.4	77.8	75.4	
370	90.8	90.4	89.9	89.4	89.0	88.5	88.0	87.6	87.1	86.7	85.6	83.8	82.0	80.3	
380	90.9	90.4	90.0	89.5	89.1	88.6	88.1	87.7	87.2	86.8	85.4	83.6	81.7	79.9	
390	91.2	91.0	90.7	90.5	90.3	90.1	89.9	89.7	89.5	89.2	88.6	87.7	86.8	85.9	
400	91.3	91.2	91.0	90.9	90.7	90.6	90.5	90.3	90.2	90.0	89.5	88.9	88.2	87.6	
410	91.3	91.2	91.1	91.0	90.8	90.7	90.6	90.4	90.3	90.2	89.7	89.1	88.5	87.9	
420	91.4	91.2	91.1	91.0	90.8	90.7	90.6	90.4	90.3	90.2	89.6	88.9	88.3	87.7	
430	91.4	91.2	91.1	91.0	90.8	90.7	90.6	90.4	90.3	90.2	89.4	88.8	88.1	87.4	
440	91.4	91.3	91.1	91.0	90.8	90.7	90.6	90.4	90.3	90.1	89.5	88.8	88.1	87.4	
450	91.4	91.3	91.2	91.1	90.9	90.8	90.7	90.5	90.4	90.3	89.7	89.1	88.5	87.9	
460	91.5	91.4	91.3	91.2	91.1	91.0	90.9	90.8	90.7	90.6	90.0	89.5	89.0	88.5	
470	91.5	91.4	91.4	91.3	91.2	91.1	91.0	90.9	90.8	90.8	90.3	89.9	89.4	89.0	
480	91.6	91.5	91.4	91.3	91.3	91.2	91.1	91.1	91.0	90.9	90.5	90.1	89.8	89.4	
490	91.6	91.5	91.5	91.4	91.4	91.3	91.2	91.2	91.1	91.1	90.8	90.5	90.2	89.9	
500	91.6	91.6	91.5	91.5	91.4	91.4	91.4	91.3	91.3	91.2	90.9	90.6	90.4	90.1	
510	91.6	91.6	91.5	91.5	91.4	91.4	91.4	91.3	91.3	91.2	90.9	90.7	90.4	90.2	
520	91.7	91.6	91.6	91.5	91.5	91.4	91.4	91.3	91.3	91.2	91.1	90.9	90.7	90.5	
530	91.7	91.6	91.6	91.6	91.5	91.5	91.5	91.4	91.4	91.4	91.2	91.0	90.8	90.6	
540	91.7	91.7	91.6	91.6	91.5	91.5	91.5	91.4	91.4	91.3	91.2	91.0	90.9	90.7	
550	91.7	91.7	91.6	91.6	91.5	91.5	91.5	91.4	91.4	91.3	91.2	91.0	90.9	90.7	
560	91.7	91.7	91.6	91.6	91.5	91.5	91.5	91.4	91.4	91.3	91.2	91.0	90.8	90.6	
570	91.7	91.7	91.6	91.6	91.5	91.5	91.5	91.4	91.4	91.3	91.2	91.0	90.8	90.6	
580	91.7	91.7	91.6	91.6	91.5	91.5	91.5	91.4	91.4	91.3	91.1	90.9	90.6	90.4	
590	91.7	91.7	91.6	91.6	91.5	91.5	91.5	91.4	91.4	91.3	91.0	90.8	90.5	90.3	
600	91.7	91.7	91.6	91.6	91.5	91.5	91.5	91.4	91.4	91.3	90.9	90.7	90.4	90.1	
610	91.7	91.7	91.6	91.5	91.5	91.4	91.3	91.3	91.2	91.1	90.9	90.6	90.3	90.0	
620	91.7	91.7	91.6	91.5	91.5	91.4	91.3	91.3	91.2	91.1	90.8	90.4	90.0	89.7	
630	91.8	91.7	91.6	91.5	91.5	91.4	91.3	91.3	91.2	91.1	90.7	90.3	90.0	89.6	
640	91.7	91.7	91.6	91.5	91.4	91.3	91.2	91.1	91.0	90.9	90.6	90.2	89.8	89.4	
650	91.7	91.7	91.6	91.5	91.4	91.3	91.2	91.1	91.0	90.9	90.6	90.2	89.8	89.4	
660	91.8	91.7	91.6	91.5	91.5	91.4	91.3	91.3	91.2	91.1	90.7	90.3	89.9	89.5	
670	91.8	91.7	91.6	91.6	91.5	91.4	91.3	91.2	91.2	91.1	90.7	90.3	90.0	89.6	
680	91.8	91.7	91.6	91.6	91.5	91.4	91.3	91.2	91.2	91.1	90.7	90.3	90.0	89.6	
690	91.8	91.7	91.6	91.6	91.5	91.4	91.3	91.2	91.2	91.1	90.8	90.4	90.1	89.7	
700	91.8	91.7	91.6	91.6	91.5	91.4	91.3	91.2	91.2	91.1	90.8	90.4	90.1	89.7	
710	91.8	91.7	91.6	91.6	91.5	91.4	91.3	91.2	91.2	91.1	90.8	90.4	90.1	89.7	
720	91.8	91.7	91.6	91.6	91.5	91.4	91.3	91.2	91.2	91.1	90.8	90.4	90.1	89.7	
730	91.8	91.8	91.7	91.6	91.6	91.5	91.4	91.4	91.3	91.2	90.8	90.4	90.1	89.7	
740	91.8	91.8	91.7	91.6	91.6	91.5	91.4	91.4	91.3	91.2	90.8	90.4	90.1	89.7	
750	91.8	91.8	91.7	91.6	91.6	91.5	91.4	91.4	91.3	91.2	90.8	90.4	90.1	89.7	
760	91.8	91.8	91.7	91.6	91.6	91.5	91.4	91.4	91.3	91.2	90.8	90.4	90.1	89.7	
770	91.8	91.8	91.7	91.6	91.6	91.5	91.4	91.4	91.3	91.2	90.8	90.4	90.0	89.6	
780	91.8	91.7	91.7	91.6	91.5	91.4	91.3	91.2	91.1	91.1	90.7	90.3	89.9	89.5	
790	91.9	91.8	91.7	91.6	91.6	91.5	91.4	91.4	91.3	91.2	90.7	90.2	89.8	89.4	
800	91.8	91.8	91.7	91.6	91.5	91.4	91.3	91.2	91.1	91.0	90.6	90.2	89.7	89.3	

Form 0050/6B

Annex 2.3.3



Form 0050/68B

Annex 3.3.1

Specification		PCE - TKT																	
Physical and chemical properties		B 270 Superwite																	
Chemical toughening parameter																			
Glass and chemical toughening parameters																			
Transformation temperature	°C	533																	
Glass thickness	mm	3																	
Processing time	h	18																	
Processing temperature	°C	420																	
Salt bath (* weight percentages)	KNO ₃ in % *	99.5																	
	SiO ₂ x H ₂ O in % *	0.5																	
Chemical toughening results *																			
Penetration depth	μm	48																	
Birefringence	nm/cm	7200																	
* measured across at a sample piece ground down to 0.3 mm ± 0.05 mm																			
Ball drop test acc. FDA	% failed	not carried out																	
Ball drop test acc. DIN	% failed	not carried out																	
<table border="1"> <caption>Approximate data points from the Birefringence vs. Processing Temperature graph</caption> <thead> <tr> <th>Processing temperature (°C)</th> <th>Birefringence (nm/cm)</th> </tr> </thead> <tbody> <tr><td>360</td><td>3500</td></tr> <tr><td>380</td><td>6000</td></tr> <tr><td>400</td><td>7200</td></tr> <tr><td>420</td><td>7500</td></tr> <tr><td>440</td><td>6500</td></tr> <tr><td>460</td><td>4500</td></tr> <tr><td>480</td><td>3000</td></tr> </tbody> </table>				Processing temperature (°C)	Birefringence (nm/cm)	360	3500	380	6000	400	7200	420	7500	440	6500	460	4500	480	3000
Processing temperature (°C)	Birefringence (nm/cm)																		
360	3500																		
380	6000																		
400	7200																		
420	7500																		
440	6500																		
460	4500																		
480	3000																		

Form 0050/68

APPENDIX B

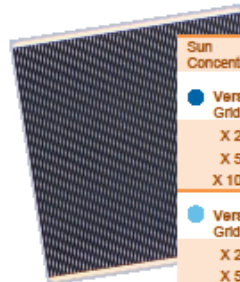
AZUR SPACE 3C44



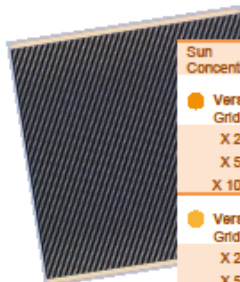
Concentrator Triple Junction Solar Cell
 Cell Type: 3C44 – 10 x 10mm²
 Application: Concentrating Photovoltaic (CPV) Modules



Typical Average Electrical Data



Sun Concentration	I _{sc} [A]	V _{oc} [V]	I _{MPP} [A]	V _{MPP} [V]	P _{MPP} [W _{MPP}]	FF [%]	D [%]
Version MC/Air Grid optimized for medium concentration + Antireflective Coating adapted to air							
X 250	3,85	3,06	3,77	2,80	10,59	89,9%	42,1
X 500	7,66	3,11	7,54	2,81	21,20	88,9%	42,0
X 1000	15,35	3,15	15,07	2,69	40,56	83,8%	40,3

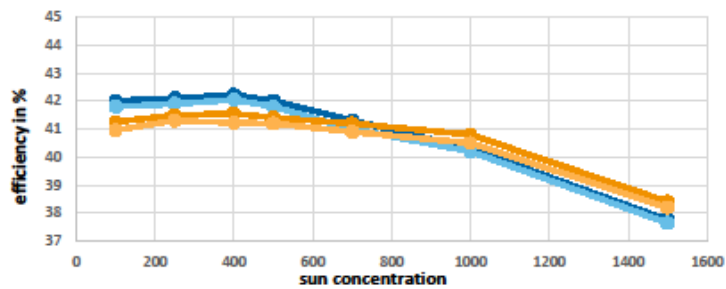


Version MC/Glass Grid optimized for medium concentration + Antireflective Coating adapted to glass							
X 250	3,82	3,07	3,76	2,80	10,55	89,9%	41,9
X 500	7,61	3,11	7,50	2,81	21,04	88,8%	41,8
X 1000	15,36	3,15	14,98	2,70	40,46	83,8%	40,2

Sun Concentration	I _{sc} [A]	V _{oc} [V]	I _{MPP} [A]	V _{MPP} [V]	P _{MPP} [W _{MPP}]	FF [%]	D [%]
Version HC/Air Grid optimized for high concentration + Antireflective Coating adapted to air							
X 250	3,76	3,06	3,68	2,83	10,44	90,7%	41,5
X 500	7,49	3,11	7,38	2,83	20,88	89,6%	41,4
X 1000	15,17	3,14	14,82	2,77	41,08	86,4%	40,8

Version HC/Glass Grid optimized for High concentration + Antireflective Coating adapted to glass							
X 250	3,75	3,06	3,68	2,82	10,39	90,5%	41,3
X 500	7,47	3,10	7,35	2,82	20,73	89,5%	41,2
X 1000	14,97	3,14	14,71	2,77	40,77	86,9%	40,5

Efficiency versus Sun Concentration



Measurement conditions: 1.5 AM_{1.5} – 1000 W/m² (ASTM G 173-03), T = 25 °C, designated measurement area = 100,51 mm²

Issue date: 2015-04-02
 Released for publication (level 1 of 5)
 HNR 0004355-00-00
 Page 1 of 4

Copyright © 2015 AZUR SPACE Solar Power GmbH

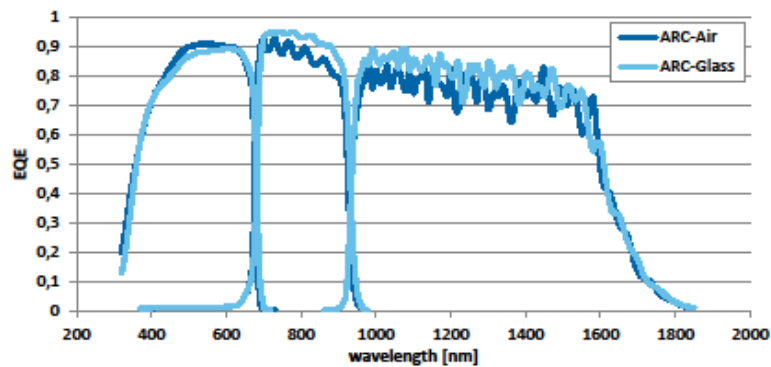
AZUR SPACE Solar Power GmbH
 Theresienstr. 2
 74072 Heilbronn
 phone: +49 7131 87 2803
 telefax: +49 7131 87 2727
 e-mail: info@azurspace.com
 website: www.azurspace.com



3C44

CPV

Spectral Response



Typical Temperature Coefficients

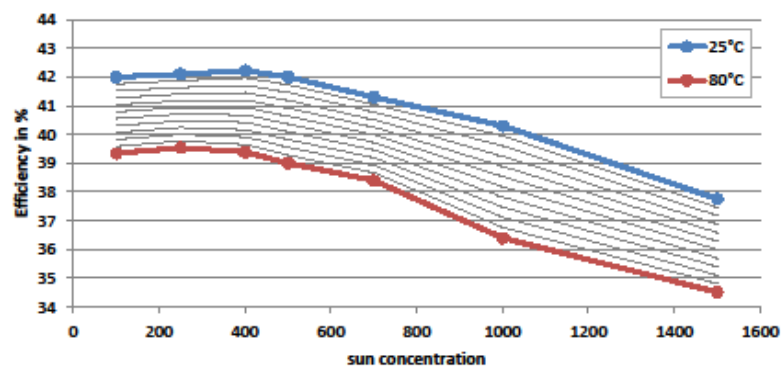
Temperature range (25 – 80 °C)

Parameter	$(\Delta I_{sc} / I_{sc}(25^\circ\text{C})) / \Delta T$	$(\Delta V_{oc} / V_{oc}(25^\circ\text{C})) / \Delta T$	$(\Delta P_{mp} / P_{mp}(25^\circ\text{C})) / \Delta T$	$(\Delta \eta / \eta(25^\circ\text{C})) / \Delta T$
Value	0,080%/K	-0,135%/K	-0,106%/K	-0,106%/K
Parameter	$\Delta I_{sc} / \Delta T$	$\Delta V_{oc} / \Delta T$	$\Delta P_{mp} / \Delta T$	$\Delta \eta / \Delta T$
Value	6,1 mA/K	-4,2 mV/K	-22,5 mW/K	-0,045%/K

Exemplary values measured with version MCI/Air, at 500 suns

Typical Performance over Temperature

Exemplary for version MCI/Air



Version Comparison

Opto Electrical Behaviour		Influence of Cell Dimension	
Antireflective Coating	Efficiency change on glass covered cells	Active Area	Typical efficiency (Version MCI/Air at 250 suns)
Version Air	-3,2 % _(typ)	3 x 3 mm	44,0 %
Version Glass	-0,4 % _(typ)	5,5 x 5,5 mm	42,9 %
		10 x 10 mm	42,1 %

Efficiency comparison at 500 suns

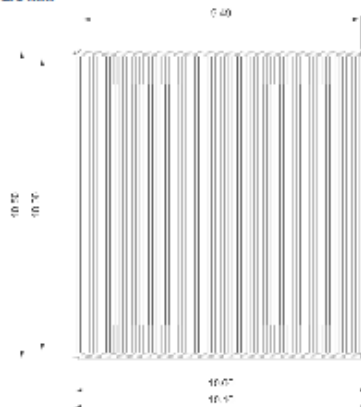


Design and Mechanical Data

Base Material	GaInP/GaInAs/Ge on Ge substrate
AR coating	TiO ₂ /AlO ₂
Chip size	10,1 mm x 10,5 mm = 106,05 mm ²
Active Cell Area	10,0 mm x 10,0 mm = 100 mm ²
Cell thickness	190 µm ± 20 µm
Polarity	N on P
Thickness of front contact	≥ 2,8 µm (finish is an Ag/Au alloy)
Thickness of back contact	≥ 2,8 µm (finish is an Ag/Au alloy)
Assembly methods	suitable for welding, soldering and bonding

Layout details

Drawing dimension are mm



Sample drawing shows version with HC-grid design; More details in drawing HNR 0003782 and HNR 0003783, available on request.



Storage and Operation Conditions Requirements

- Humidity protection is strongly recommended
- Storage in dry air or nitrogen atmosphere is requested
- As front side interconnector material we recommend gold or silver
- We recommend to use Sn98.5/Ag3.5-solder or another solder with saturated silver for rear side assembly
- A void free rear side assembly (heat sink) is requested to avoid hot spots
- The cell junction shall not exceed a maximum operation temperature of 110° C
- Secondary glass glue on the front side has to be flexible (prefer silicone glue or similar)

Additional Information

- Current values at specific operating voltage can be offered on customer request
- Explanation of ARC versions:
 - o AIR:

The antireflective coating on top of the solar cell is optimized for the interface to air. In this kind of application the light enters the solar cell directly from air. The indoor test measurement (flash test) will be done at air atmosphere.
 - o GLASS:

The antireflective coating on top of the solar cell is optimized for the interface to glass or similar (n≈1.43). At this kind of application the light enters the solar cell through a glass component or similar (e.g. secondary element, homogenizer element, cover glass). However, the indoor test measurement (flash test) will be done at air atmosphere without glass interface. Therefore the flash test results will underestimate the potential cell performance. The performance of a system with glass interfaces is expected to be higher using cells with ARC Glass than with ARC Air.
- Acceptance test rules for delivery lots:
 - o Minimum average efficiency = typical average value minus 2% (rel.)
 - o Minimum individual cell efficiency = typical average value minus 5% (rel.)

Order Information

Product Version	 wafer (not diced)	 diced wafer, mounted on a tape
 MC/Air	81244	81245
 MC/Glass	81246	81247
 HC/Air	81248	81249
 HC/Glass	81250	81251

APPENDIX C

REPORT AND CERTIFICATION OF ORIEL'S SOL1A™ CLASS ABB SOLAR SIMULATOR

11.1 NON UNIFORMITY REPORT

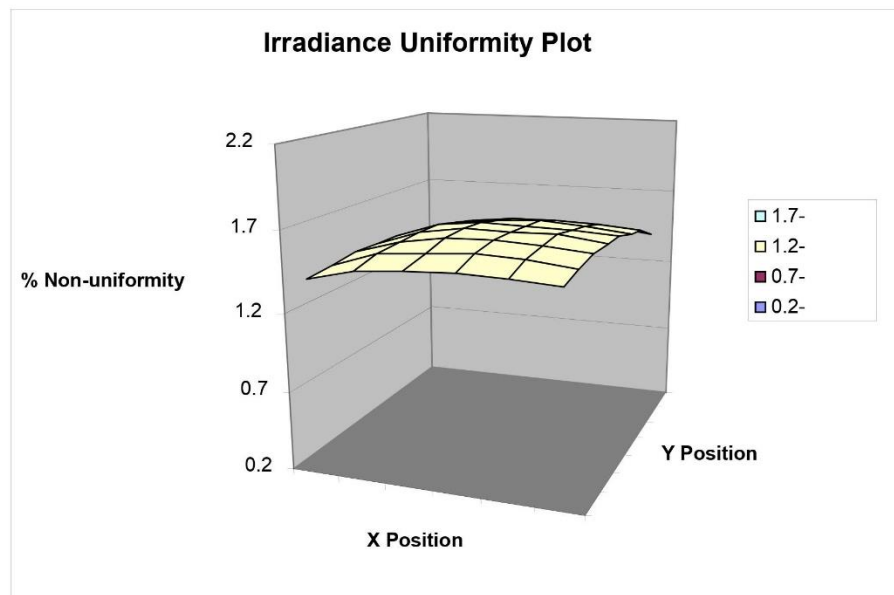
Performance validation procedure of Non-uniformity of irradiance:

1. IEC and ASTM non-uniformity of irradiance of Sol1A Model 94021A, Serial# 1005, lamp serial# RCO677 is 2.44%

The IEC and ASTM uniformity measurement data consists of 64 data points, where the designated test area was divided into 64 equally sized (by area) test positions (blocks). The uniformity detector size was divided by 64. A single detector was used for measurements covering 100% of the designated area and measurement positions were distributed uniformly over the designated test area.

2. JIS non-uniformity of irradiance of Sol1A Model 94021A, Serial# 1005, lamp serial# RCO677 is 2.06%

The JIS uniformity measurement data consists of 17 data points as required and mapped in JIS standard for measuring positional non-uniformity of irradiance, where a single square detector was used with size not exceeding 2 cm and 4% of effective irradiated plane.

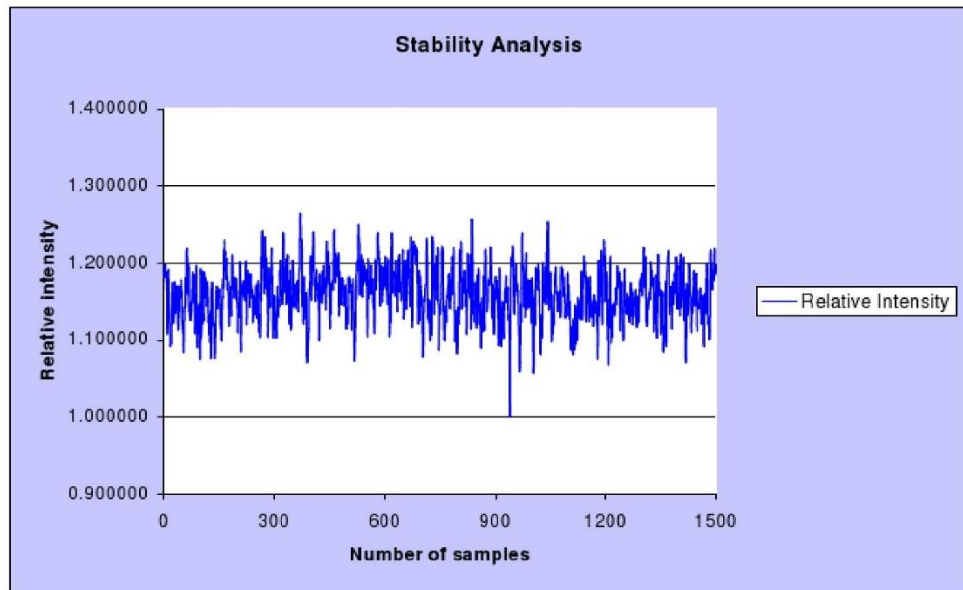


11.2 TEMPORAL INSTABILITY REPORT

Performance validation procedure of temporal instability of irradiance:

1. Temporal instability of irradiance of Sol1A Model 94021A, Serial# 1005, Lamp# RCC677

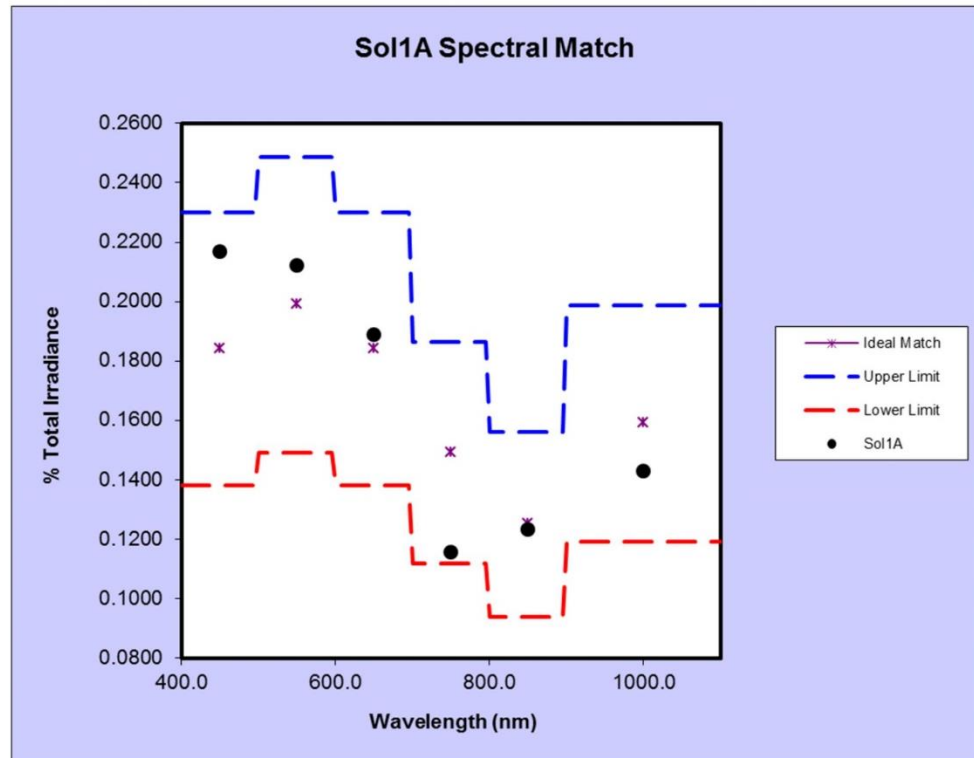
The temporal instability measurement data consists of 20 samples acquired over each time period in consideration. Data was acquired by placing a solar cell in the optical center of the lens at the model-specified height of reference plane where the measured irradiance was 1 SUN (+/- 0.05 SUN). Irradiance level was measured using a NREL-calibrated reference cell.



11.3 SPECTRAL MATCH REPORT

Performance validation of Spectral Match:

	400-500	500-600	600-700	700-800	800-900	900-1100	400-1100
Ideal Match%	18.40%	19.90%	18.40%	14.90%	12.50%	15.90%	100.00%
Upper Limit%	23.00%	24.88%	23.00%	18.63%	15.63%	19.88%	
Lower Limit%	13.80%	14.93%	13.80%	11.18%	9.38%	11.93%	
Sol1A%	21.69%	21.23%	18.88%	11.57%	12.32%	14.31%	



First printing 2010

© 2011 by Newport Corporation, Irvine, CA. All rights reserved.
No part of this manual may be reproduced or copied without the prior written approval of Newport Corporation.

This manual has been provided for information only and product specifications are subject to change without notice.
Any change will be reflected in future printings.

Newport Corporation 1791 Deere Avenue Irvine, CA, 92606 USA

APPENDIX D

PUBLICATION: OPTICAL AND ELECTRICAL PERFORMANCE EVALUATION OF CROSSED COMPOUND PARABOLIC CONCENTRATOR MODULE FOR THE APPLICATION OF ULTRA- HIGH CONCENTRATOR PHOTOVOLTAIC SYSTEM

IOP Conference Series: Earth and Environmental Science

PAPER • OPEN ACCESS

**Optical and Electrical Performance Evaluation of the Crossed
Compound Parabolic Concentrator Module for the Application of Ultra-
High Concentrator Photovoltaic System**

To cite this article: Pei-Shan Lee et al 2019 *IOP Conf. Ser.: Earth Environ. Sci.* **268** 012031

View the [article online](#) for updates and enhancements.



IOP ebooks[™]
Bringing you innovative digital publishing with leading voices
to create your essential collection of books in STEM research.
Start exploring the collection - download the first chapter of
every title for free.

This content was downloaded from IP address 121.123.29.24 on 09/07/2019 at 06:35

Optical and Electrical Performance Evaluation of the Crossed Compound Parabolic Concentrator Module for the Application of Ultra-High Concentrator Photovoltaic System

Pei-Shan Lee¹, Chee-Woon Wong^{1,*}, Tiong-Keat Yew², Ming-Hui Tan², Kok-Keong Chong¹, Woei-Chong Tan¹ and Boon-Han Lim¹

¹Lee Kong Chian Faculty of Engineering and Science, Universiti Tunku Abdul Rahman, Bandar Sungai Long, 43000 Kajang, Selangor, Malaysia

²Faculty of Engineering and Green Technology, Universiti Tunku Abdul Rahman, Jalan Universiti, Bandar Barat, 31900 Kampar, Perak, Malaysia

*Corresponding author's E-mail address: wewoon@utar.edu.my

Abstract. This paper presents the performance evaluation in terms of optical and electrical characteristics of the crossed compound parabolic concentrator (CCPC) module for the application of the ultra-high concentrator photovoltaic (UHCPV) system. The CCPC module is the integration of a dielectric-filled 3D CCPC lens and a multi-junction solar cell (MJSC) module. The optical efficiency of the refractive lens has been evaluated through the ray-tracing simulation technique by including all the possible optical losses at each component level, and the output current of the MJSC module has also been calculated in accordance with its spectral response to the wavelengths range from 300 nm to 1800 nm. The optical efficiency of CCPC lens itself is determined to be 69.33%. With reference to the output current of the MJSC module without a CCPC lens, an optical concentration ratio of 4.65 is observed in the simulated result. An indoor experiment has been performed to validate the simulated result, in which an effective optical concentration ratio of 4.57 has been obtained via laboratory measurement. The experimental result is matched well with the simulated result and it shows that the CCPC module has an effective optical efficiency of 76.17% as the geometrical concentration ratio of the CCPC lens is 6.00. The detailed study of CCPC module is good for optimizing the performance of the UHCPV system.

1. Introduction

In recent years, the introduction of multi-junction solar cells (MJSCs) with the proven optical-to-electrical efficiency of 46% has accelerated the research and development of concentrator photovoltaic (CPV) system. Due to the remarkable cost reductions in flat-plate photovoltaic (PV) modules, a CPV system with greatly improved solar concentration ratio (SCR) is indeed a significant strategy to be a highly competitive solution in the solar energy market. By boosting the CPV system to ultra-high concentration ratio, it can dramatically reduce the usage of high-cost solar cells by replacing with inexpensive optics as well as the leveled cost of solar electricity (LCSE). The higher the SCR, the higher the system output power. However, an effective way of solar energy harvesting can be challenging due to the chromatic aberration limits for single material mirrors/lenses. In respect to this issue, an earlier study suggested that by adding homogenizing lenses as secondary optics to the



Content from this work may be used under the terms of the [Creative Commons Attribution 3.0 licence](https://creativecommons.org/licenses/by/3.0/). Any further distribution of this work must maintain attribution to the author(s) and the title of the work, journal citation and DOI.
Published under licence by IOP Publishing Ltd

system, it is able to break through the boundaries and produce a SCR of more than 1000 suns [1]. Among all types of homogenizing optics, a 3D-CPC is said to be the most ideal as it works perfectly for all light incidences within the desired acceptance angle [2-3]. Thus, Wong et al. has proposed an ultra-high concentrator photovoltaic system using small-scale two-stage non-imaging solar concentrator. This system has the capability to produce an ultra-high SCR (>1000 suns) and a reasonably uniform solar illumination focused onto the MJSCs[4]. The proposed UHCPV system comprises of non-imaging dish concentrator (NIDC) as a primary optical element (POE) and crossed compound parabolic concentrator (CCPC) lens as a secondary optical element (SOE) [4].

The general features of CCPC lens has been discussed in the previous work [4-6], but a detailed performance evaluation on the lens has yet to be studied. In a CPV system, optics are the core components to determine the practicability of the system. A good understanding of the optical characteristics is the key to optimize the performance of a CPV system. Therefore, there is an interest to study the performance of CCPC lens in detailed. In this paper, the detailed characteristics of a CCPC module, a combination of a dielectric-filled 3D CCPC lens and a multi-junction solar cell (MJSC) module, is evaluated in terms of optical and electrical performance by considering several imperfection factors that were neglected in the previous study. The evaluation has been done through computational and experimental methods.

2. Overview of the CCPC Module

Figure 1 shows the illustrative diagram of the UHCPV system, which consists of NIDC and CCPC modules, proposed by Wong et. al [4]. As shown in Figure 1(b), the CCPC modules comprises of CCPC lenses and MJSC modules. Optical adhesive is used to bond the components together. Each receiver module is equipped with MJSC and a bypass diode. The MJSC consists of three layers of different materials connected in series, which is Indium Gallium Phosphide (InGaP), Indium Gallium Arsenide(InGaS) and Germanium(Ge), where each material responds to a different range of the solar spectral irradiance. Figure 1(c) shows the cross-sectional view of the CCPC lens, which possesses with entrance aperture, $2a$ and exit aperture, $2a'$ with the dimension of 24mm and 9.8mm respectively that result in geometrical concentration ratio (GCR) of 6.00. The dimension of the square-shaped exit aperture are designed to match with the dimension of Azur Space 3C44 MJSC used in the module, at which the cell aperture's dimension is 10 mm × 10 mm. The exit aperture of CCPC lens is slightly smaller than the solar cell to avoid low packing factor due to the less active area at the peripheral region of the cell. The angular half acceptance angle, θ_1 and length of the CCPC lens is 37.77° and 37.78mm respectively. The CCPC lens are made of Schott B270 Crown Glass due to its high transmissivity and affordable cost.

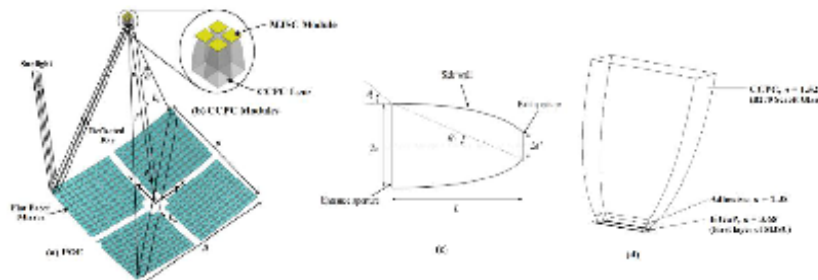


Figure 1. The 3-dimensional view of the proposed ultra-high concentrator photovoltaic (UHCPV) system. (a) Primary optical element (POE), non-imaging dish concentrator (NIDC) (b) Crossed compound parabolic concentrator (CCPC) modules, a combination of CCPC lenses and MJSC modules (c) Schematic diagram to show the dimension of the dielectric-filled CCPC lens (d) Refractive index, n of each component level of the CCPC module [4].

3. Performance evaluation of the CCPC Module

With the aid of an opto-mechanical software, Tracepro, a comprehensive optical characterization of CCPC lens has been carried out through the ray-tracing technique by considering all the possible optical losses at each component level, such as Fresnel reflection losses, materials' transmissivity - absorption, edge/corner leakage due to adhesive spillage, and the effect of anti-reflective coating. The Fresnel reflection loss occurs at the interface of two materials when there is any discontinuity of refractive index [7]. Figure 1(d) shows the refractive index, n of each component in the model. In this study, Fresnel losses occur thrice in total as there are four different mediums including air. To overcome the big gap between the n of Indium Gallium Phosphide (InGaP), which is the first layer of MJSC, and the engaged medium (glass or optical coupler), a bilayer of anti-reflective coating is deployed on the surface of the solar cell to minimize Fresnel reflection losses [8]. A summary of the evaluation process is illustrated in Figure 2.

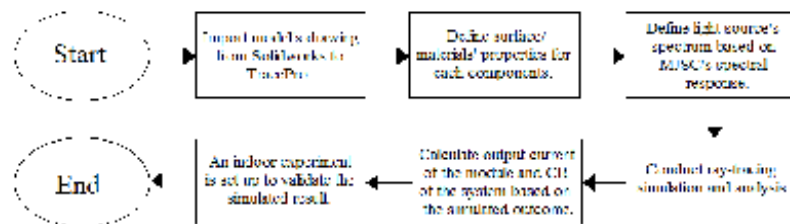


Figure 2. Flowchart to show a process of evaluating the optical and electrical performance of the CCPC module.

It is significant to define the surface and materials' properties data in the simulation. Defining any improper property data may result in inadequate accuracy. Most of the properties data used in the simulation are obtained from TracePro's built-in database while the information that is not included in the library such as absorption coefficient, α and extinction coefficient, k of Schott B270 Glass and Indium Gallium Phosphide (first layer of MJSC), the properties data are extracted from the datasheet as provided by the manufacturer. The wavelength of light source is set in a range of 300 nm – 1800 nm in accordance with the spectral response of MJSC. The ray-trace simulation began with a set of parallel light rays approaching the CCPC lens. Once the light rays reached the lens, the light rays undergone the process of reflection, refraction and scattering before reaching the exit aperture of the geometry via total internal reflection. The CCPC lens is bonded on the solar cell with the use of optical adhesive, and from the previous study [9], it is stated that the encapsulant spillage will lead to light leakage from the edge of the optical element. To consider the edge/corner leakage due to adhesive spillage, the simulation has been carried out by attaching a layer of adhesive in between CCPC lens and MJSC as shown in Figure 3. The t_{ad} represents the total thickness of the adhesive layer while t_{se} is the thickness of the adhesive spillage surrounding the bottom edge of CCPC lens. Both the aforementioned variables are the key parameters to predict the optical losses at the point in which the light rays are entering solar cell from the exit aperture of CCPC lens passing through the optical adhesive.



Figure 3. The adhesive layer is inserted into the model for simulation.

From the aspect of electrical performance, the output current generated from a CCPC module (or CCPC lens + MJSC module assembly) can be estimated from its spectral response to the light source. The output current of MJSC module with CCPC lens ($I_{CCPC+MJSC}$), output current of MJSC module without a CCPC lens (I_{MJSC}) and concentration ratio (CR) of CCPC module are determined as follows:

$$CR = \frac{I_{CCPC+MJSC}}{I_{MJSC}} = \frac{A_{active} \times \frac{q\lambda}{hc} \int \phi_{EQE}(\lambda) \cdot \phi_{Spec(CCPC+MJSC)}(\lambda) d\lambda}{A_{active} \times \frac{q\lambda}{hc} \int \phi_{EQE}(\lambda) \cdot \phi_{Spec(MJSC)}(\lambda) d\lambda} = \frac{\int \phi_{Spec(CCPC+MJSC)}(\lambda) d\lambda}{\int \phi_{Spec(MJSC)}(\lambda) d\lambda} \quad (1)$$

where A_{active} is the active area of MJSC, q represents the electric charge, c stands for the speed of light in vacuum, h is the Planck's constant, $\phi_{EQE}(\lambda)$ is the external quantum efficiency of each subcell in the MJSC in which it is represented in a function of wavelength, λ , $\phi_{Spec(CCPC+MJSC)}(\lambda)$ and $\phi_{Spec(MJSC)}(\lambda)$ are the spectral irradiance received by the MJSC module with and without a CCPC lens, respectively.

To validate the simulated result, an indoor experiment has been carried out by using the Oriol's SolIA™ Class ABB Solar Simulator. The spectrum of the light source is first measured using a spectrometer so that the value can be used to calculate the output current of the MJSC in the ray-tracing simulation. To ensure both MJSC module without a lens and CCPC module receive the same amount of incident light within the same acceptance angle, the entrance aperture is fixed at the same height with a fixed position. The outcome has been tabulated based on an average of five measurements, and this will be further discussed in the next section.

4. Result and discussion

The optical efficiency profile of CCPC module, the ratio of the light received by the MJSC to the light entering the entrance aperture of CCPC lens, as shown in Figure 4 depicts severe optical losses at each edge/corner of the exit aperture of CCPC lens. The optical efficiency at each particular point of the entrance aperture of CCPC lens has been obtained by using the simulation program and was presented in a heat map as shown in Figure 4(a). The real optical losses in the CCPC lens under direct normal irradiance can be observed with naked eyes (see Figure 4(b)). Due to the adhesive spillage, an obvious light can be seen from each edge/corner of the exit aperture of CCPC lens.

Table 1 shows the optical losses determined from the ray-tracing simulation. By defining the refractive index, n corresponding to different wavelengths, absorption coefficient, α and extinction coefficient, k of the surface/materials, the losses which took place at each component level of the CCPC module can be determined. The majority type of the losses is attributed by Fresnel reflection losses as the incident rays travelled through four different mediums (from air → glass → adhesive → MJSC). However, the greatest percentage among all the losses is recognized as the absorption loss of CCPC lens which is made from B270 Schott glass. This indicates that the material's absorption is the main cause of optical losses. However, it is unavoidable in the current stage as the geometry of the CCPC lens is designed to match with the dimension of the receiver. Yet, this can be a hint for future design work to reduce the system losses. In the simulation, t_{ad} is assumed as 1 mm and its refractive index, n is 1.38 at 550nm, which explains why the Fresnel losses from CCPC lens to the adhesive is relatively small due to their small difference in refractive index. The absorption of adhesive is neglected as the thickness is too small to affect the outcome. The overall percentage of each loss is calculated in terms of the input power received at the entrance of the CCPC lens. The optical efficiency of the CCPC module is 69.33% after excluding the total percentage losses.

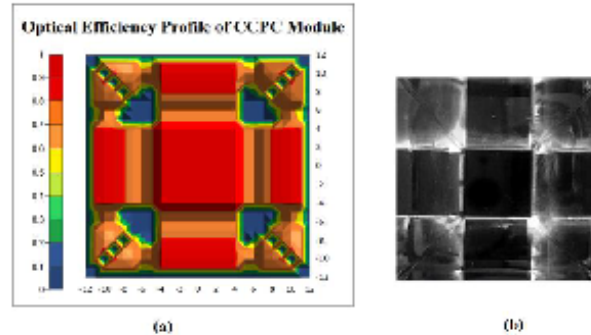


Figure 4. The optical efficiency profile of CCPC module indicates severe optical losses are incurred at the edge/corner under direct normal irradiance. (a) Simulation result. (b) Top view of actual CCPC module.

Table 1. The optical losses at each component level of the CCPC module.

Type of losses	Percentage (in term of input)
Fresnel Loss I – From air to CCPC	4.14%
Absorption Loss – CCPC lens (B270 Schott Glass)	11.46%
Edge/Corner Leakage	5.30%
Fresnel Loss II – From CCPC to adhesive	0.20%
Fresnel Loss III – From adhesive to MJSC	9.56%
Total losses	30.66%

On the other hand, Table 2 shows the outcome comparison between the simulated and experimental process. The simulated CR is calculated by comparing the output current of the CCPC module to the output current of the MJSC module alone as derived in equation (1). The spectrum of the light source used in the experiment is measured using a spectrometer, and the value obtained is substituted into equation (1) for output current calculation. The simulated result for the output current is slightly lower than the experimental result. There are two possible reasons which causes such outcome: (a) measurement distortion of the spectrometer, (b) the error in the current calculation due to the discrepancy in external quantum efficiency (EQE) of the MJSC provided in the datasheet. However, the result shows that both outcomes are tally to each other with a minor difference of 1.7% when normalized it to CR. From the result, it shows that the CCPC module (CCPC lens + MJSC module) has an overall effective efficiency of 76.17% (4.57 out of GCR of 6.00), which both optical and electrical losses are included with the consideration of current mismatch losses.

Table 2. The outcome comparison between the simulation and experiment.

Type of model	Calculated Current (I_{SC})	Measured Current (I_{SC})
CCPC lens + MJSC module	34.19mA	43.26mA
Only MJSC module	7.36mA	9.46mA
Concentration Ratio (CR)	4.65	4.57

In the previous work done by Chong et al. [6], a $CR_{measured}$ of 4.07 is obtained through an outdoor experiment setup. This result is below the expectation as compared to the outcome obtained from this paper. This might be caused by the inconsistent ambient condition applied to the two modules during the experiment. Therefore, the following step in this study is to conduct another outdoor experiment with a more precise setup with the consideration of the same amount of input incidence and acceptance angle for both models.

5. Conclusion

This paper has presented the investigation on the optical and electrical performance of the CCPC module for the application of UHCPV system for both simulation and experimental approach. By considering all the possible losses in the simulation, the CCPC lens has an optical efficiency of 69.33%. For the concentration ratio, the simulation result is 4.65 while the experimental result is 4.57. This indicates that the real CCPC module has an effective optical efficiency of 76.17% since the geometrical concentration ratio of the CCPC lens is 6.00. The absorption loss of CCPC lens and Fresnel reflection losses from the optical adhesive to MJSC interface are the major losses in the CCPC module. The comparison between the simulated and experimental results show a reliable accuracy of the ray-tracing technique used in this study, where two results are tally to each other with a minor difference of 1.7%. In a nutshell, the proposed work can provide a better understanding of optical and electrical properties of CCPC module, which are essential for optimizing the performance of UHCPV system. In future, the performance evaluation of the CCPC will be further studied by performing several tests for different angles of incident light in terms of both polarization and azimuth angle, with the integration of NIDC to determine the overall performance of the whole UHCPV system.

Acknowledgements

The authors would like to express their gratitude to the Ministry of Energy, Green Technology and Water (AAIBE Trust Fund with vote account 4356/001) and UTAR Research Fund with project number IPSR/RMC/UTARRRF/2017-C1/W03 (vote account 6200/W61) for their financial support. Besides, the authors would also like to thank Lambda Research Corporation for providing evaluation license of their optical solution product: TracePro.

References

- [1] Shanks K, Senthilarasu S and Mallick T K 2016 Optics for concentrating photovoltaics: trends, limits and opportunities for materials and design *Renew. Sustain. Energy Rev.* 60 394–407
- [2] Winston R, Minano J C, and Benitez P 2005 *Nonimaging Optics* (US: Elsevier Inc)
- [3] Sellami N and Mallick T K 2013 Optical efficiency study of PV crossed compound parabolic concentrator *Appl. Energy* 102 868–876
- [4] Wong C W, Yew T K, Chong K K, Tan W C, Tan M H, and Lim B H 2017 Design optimization of ultra-high concentrator photovoltaic system using two-stage non-imaging solar concentrator *IOP Conf. Ser. Earth Environ. Sci.* 93
- [5] Wong C W, Chong K K and Tan M H 2015 Performance optimization of dense-array concentrator photovoltaic system considering effects of circumsolar radiation and slope error *Opt. Soc. Am.* 23
- [6] Chong K K, Yew T K, Wong C W, Tan M H, and Tan W C 2017 Dense-array concentrator photovoltaic prototype using non-imaging dish concentrator and an array of cross compound parabolic concentrators *Appl. Energy* 204 898-911
- [7] Ilouno J, Awoji M and Akeredolu B J 2018 Investigation of optical return loss (back-reflection) in optical fiber transmission links *Int. J. Comput. Sci. Mob. Comput.* 7 61–69
- [8] García-Linares P, Dominguez C, Dellea O, Kämpfe T, Jourlin Y, Besson P, Weick C and Baudrit M 2015 Improving optical performance of concentrator cells by means of a deposited nanopattern layer *AIP Conf. Proc.* 1679
- [9] Baig H, Sellami N and Mallick T K 2015 Trapping light escaping from the edges of the optical element in a concentrating photovoltaic system *Energy Convers. Manag.* 90 238–246

PUBLICATION: COMPREHENSIVE ANALYSIS ON ASSEMBLY OF DIELECTRIC FILLED CROSSED COMPOUND PARABOLIC CONCENTRATOR AND CONCENTRATOR PHOTOVOLTAIC MODULE

Research Article

Vol. 59, No. 14 / 10 May 2020 / Applied Optics 1



Comprehensive analysis on assembly of dielectric filled crossed compound parabolic concentrator and concentrator photovoltaic module

PEI-SHAN LEE,¹ CHEE-WOON WONG,¹ MING-HUI TAN,² AND KOK-KEONG CHONG^{1,*}

¹Lee Kong Chian Faculty of Engineering and Science, Universiti Tunku Abdul Rahman, Bandar Sungai Long, 43000 Kajang, Selangor, Malaysia

²Faculty of Engineering and Green Technology, Universiti Tunku Abdul Rahman, Jalan Universiti Bandar Barat, 31900 Kampar, Malaysia

*Corresponding author: chongkk@utar.edu.my

Received 15 January 2020; revised 22 March 2020; accepted 2 April 2020; posted 2 April 2020 (Doc. ID 387965); published 0 MONTH 0000

A comprehensive analysis on assembly of dielectric-filled 3D crossed compound parabolic concentrator (CCPC) and concentrator photovoltaic (CPV) module is presented by embracing the consideration of spectral irradiance, incident angles, and breakdown optical losses. The theoretical modeling is supported by experimental validation to evaluate the optical efficiency of the CCPC-CPV module. From our analysis, Fresnel reflection loss of 11.27%, absorption loss of 11.59%, and other losses of 4.79% are obtained to reach the optical efficiency of 77.3% or equivalent solar concentration ratio (SCR) of 4.65 suns out of a geometrical concentration ratio (GCR) of 5.998 suns. Then, indoor and outdoor measurements prove the actual SCR of 4.57 and 4.48 suns, respectively. © 2020 Optical Society of America

<https://doi.org/10.1364/AO.387965>

1. INTRODUCTION

The overuse of the finite energy resources has become one of the most major concerns attributed to its inescapable depletion and with it being no longer available one day. To provide a safe environment and sustainable energy production for the future generation, the development of renewable energy resources is needed to minimize pollution. The photovoltaic system is one great alternative to complement and replace conservative resources in the future. According to the U.S. Department of Energy, the amount of solar power that reaches on Earth's surface every one and a half hours is actually more than sufficient for the worldwide consumption in a year [1]. That is to say that solar energy should be able to meet the energy demands for the entire world. However, the current technologies for harvesting this clean energy from Sun are still negligible [2].

Researchers around the world have been working for years to develop a reliable way to capture and to convert solar energy into usable electricity. The concentrator photovoltaic (CPV) system has been an emerging trend in the research and development of solar technologies after the introduction of high-performance multijunction solar cells (MJSCs), which have the proven conversion efficiency of 46% [3]. The MJSC is a combination of multiple series-connected layer semiconductor materials with different bandgaps tailored to maximize the absorption of a wide solar spectrum. MJSC plays an important role in the development of the high concentrator photovoltaic (HCPV) system as it can transform highly concentrated sunlight efficiently into

electrical energy under high operating temperature. With the advantage of using relatively cheaper optics such as mirrors and lenses, the sunlight can be focused at high solar concentration ratio (SCR) of more than 500 suns onto the receiver fitted out with MJSC. The utilization of concentrating optics reduces the usage of solar cells proportionally to the SCR and hence decreases the levelized cost of electricity (LCOE). The higher the SCR, the lower the LCOE [4]. Nevertheless, there are many challenges faced by the CPV systems that need to be improved in order to be more competitive.

One of the major challenges in the CPV system is chromatic aberration limits occurred in a single material lens. A previous investigation suggested that adding homogenizing lenses as secondary optics in a CPV system can break through the boundaries and produce an SCR of more than 1000 suns [5]. A number of researchers have proposed different types of secondary optical elements (SOEs) in their CPV system to achieve higher SCR with good optical performances. The SOEs are either refractive or reflective while some of the conventional concentrators are the compound parabolic concentrator (CPC), kaleidoscope, dome-shaped lens, etc. Chen and Chiang [6] evaluated three types of SOE coupled with a flat Fresnel lens, which include kaleidoscope with equal optical path design (KOD), kaleidoscope with a flattop surface (KFTS), and open-truncated tetrahedral pyramid with specular walls (SPs). An optimized KOD lens is found to be the best in exhibiting irradiance distribution on the solar cell among the three SOEs.

Nevertheless, the optical efficiency of KOD-type SOE drops significantly at an incidence angle of greater than 2° , which indicates the KOD-type SOE requires high tracking accuracy. Similarly, EL-yahyaoui *et al.* [7] investigated the performance of the two-stage optical concentrators consisting of PMMA Fresnel lens as the primary optical element (POE) with two types of SOEs including a pyramid lens and a cone lens made of fused silica. In their indoor experiment, the pyramid lens achieved higher optical efficiency of 73.7% as the SOE. The difference between simulation and experiment results is approximately 29%, but no justification is given. Sahin and Yilmaz [8] proposed a circular diffractive SOE instead of reflective or refractive optics. Despite the addition of the diffractive SOE increasing the optical efficiency of the CPV system by 6%, the real manufactured diffractive elements will come with discrete step and cause deviation from the ideal model proposed in the paper. Based on literature studies, secondary optics have solved one problem but have concurrently incurred another problem, especially increasing optical losses. Multiple stages of optical devices in a CPV system can lead to increasing optical losses as well as the reduction of the optical precision attributed to manufacturing and alignment errors [9]. All the above studies only revealed the overall optical efficiency of concentrating optics without detailed analyses on the optical losses. We should know the optical losses before the overall efficiency in order to optimize the system more effectively.

Among all types of homogenizing optics, a 2D CPC is the most ideal optical geometry as it should work perfectly to receive all sunrays being directed within the acceptance angle [10–12]. A rotational CPC can be obtained by revolving the linear CPC at its axis. However, the circular aperture of the rotational CPC can cause losses when interfacing with the squared-entry solar cell. Thus, a crossed compound parabolic concentrator (CCPC) with square aperture is introduced as the improved version of rotational CPC [10]. There are several studies on the optical characterization of CCPC as the SOE in a CPV system. Sellami *et al.* presented a MATLAB code to simulate the optical efficiency and flux distribution of an improved atypical 3D CCPC on the solar cell for different angles of incidences [13]. However, their study is only limited to angular performance in one direction by moving the light source unidirectional, and the result is not favorable to the CPV system because of producing a nonuniform illumination distribution at the exit aperture. Baig *et al.* [14] analyzed the optical loss in a 3D CCPC. Nevertheless, it is more focused on analyzing the optical loss caused by different thicknesses of optical adhesive and the study of trapping the light from escaping via the edge/corner of the exit aperture. In fact, the optical performance of a CCPC lens is also affected by many other factors, and thus a detailed analysis for all kinds of possible optical losses should be explored. Furthermore, we also introduced the CCPC lens as the SOE coupled to a nonimaging dish concentrator (NIDC) in an ultrahigh CPV system capable of producing a reasonably uniform solar illumination with maximum SCR of 1475 suns onto the MJSC module [15–17]. Unfortunately, all the aforementioned studies have not yet scrutinized into the breakdown analysis of all the optical losses incurred in the SOE of CPV system, which can provide fundamental guidance to optimize the overall performance of the

CPV system. In this paper, we would like to propose a comprehensive analysis with detailed methodology to study the optical losses of the CCPC-CPV module: an assembly of a dielectric-filled 3D CCPC lens and a MJSC module. The evaluation in both optical and electrical performance of the CCPC-CPV module is carried out in three phases—computational simulation, indoor practical validation, and an on-site performance test. In some studies on solar power system, the effect of the full solar spectrum has been neglected in which wavelength dependency of both refractive indices and absorptions is not considered in those works [6,18,19]. Last but not least, in our theoretical modeling, the light source is simulated based on AM1.5 spectral irradiance ranging from 300 to 1800 nm in accordance with the spectral response of MJSC as provided by the specification of the manufacturer.

2. OVERVIEW OF THE CCPC-CPV ASSEMBLY MODULE

Figures 1 (a) and 1 (b) show the cross-sectional view of the CCPC lens and 3D geometry of the CCPC-CPV assembly module being studied in this paper. The optical adhesive is used as the bonding material between the CCPC lens and a MJSC module equipped with a bypass diode. Most of the solar cells in the market including Azur Space 3C44 MJSC (used in this study) are fabricated in a square or rectangular shape. To ensure a good match with the dimension of the MJSC, the lens exit aperture must be designed in square with the size slightly smaller than that of the solar cell to avoid the concentrated sunlight fallen onto the peripheral region of the solar cell, which is a nonactive region comprising the built-in bus bars [16]. The specification of the CCPC lens is listed in Table 1, and the detailed design rule of the CCPC lens used in this work has been described in our previous work [16]. B270 Schott glass is chosen as the dielectric material for the CCPC lens due to its high transmissivity and affordable cost.

The internal structure of a MJSC consists of three $p-n$ junctions made of different semiconductor materials, indium gallium phosphide (InGaP) on top, followed by indium gallium arsenide (InGaAs), and lastly germanium (Ge). The external quantum efficiency (EQE) of the MJSC versus wavelength is provided in “Concentrator Triple Junction Solar Cell Cell Datasheet” by Azur Space [20]. Each $p-n$ junction material responds to a different range of the solar spectral irradiance in such a way that the three different III–V semiconductor materials can complement each other to cover the incident light with

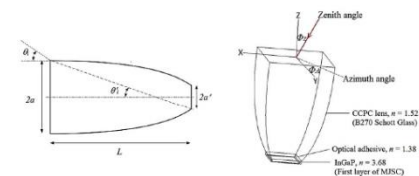


Fig. 1. (a) Cross-sectional view of the dielectric-filled CCPC lens; (b) 3D geometry of an assembly CCPC-CPV module with refractive indices, n , of each component.

Table 1. Specification of the Secondary Optics Element Used in CPV System

Secondary Optical Element (SOE):	Crossed Compound Parabolic Concentrator (CCPC) Lens
Dielectric material	B270 Schott glass
Dimension of the entrance aperture, $2a$	24 mm × 24 mm
Dimension of the exit aperture, $2a'$	9.8 mm × 9.8 mm
Length, L	37.78 mm
Geometrical concentration ratio (GCR)	5.998
Angular half acceptance angle, θ	37.77°
Optical constant of B270 Schott Glass @	300–1800 nm
Refractive index, n	1.50–1.56
Absorption coefficient, α	$2.81 \times 10^{-04} \text{ mm}^{-1} - 0.14 \text{ mm}^{-1}$
Extinction coefficient, k	$1.23 \times 10^{-08} - 3.59 \times 10^{-06}$
Internal transmittance, T_i	0–0.989
External transmittance, T_e	0–0.906

wavelength from 300 nm to 1800 nm, which is almost the full solar spectrum. Moreover, the MJSC is designed to generate high density of electrical power capable of accommodating high current and high operating temperature under highly concentrated sunlight as compared to that of the conventional silicon solar cells.

3. RESEARCH METHODOLOGY

The evaluation of the CCPC-CPV assembly module in both optical and electrical performance has been carried out through computational and experimental methods. The research methodology of theoretical modeling on the CCPC-CPV module with practical validation is presented systematically in a flow chart as depicted in Fig. 3.

A. Ray-Tracing Simulation

For a comprehensive assessment on the optical system, all the possible optical losses that occurred at each stage of the light transmission throughout the CCPC-CPV assembly

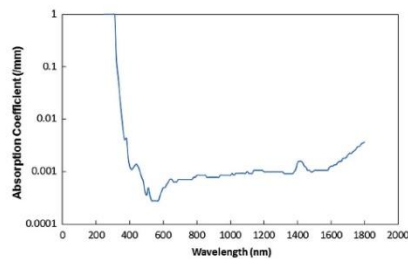


Fig. 2. Absorption coefficient of the B270 Schott Glass versus wavelength of incident light.

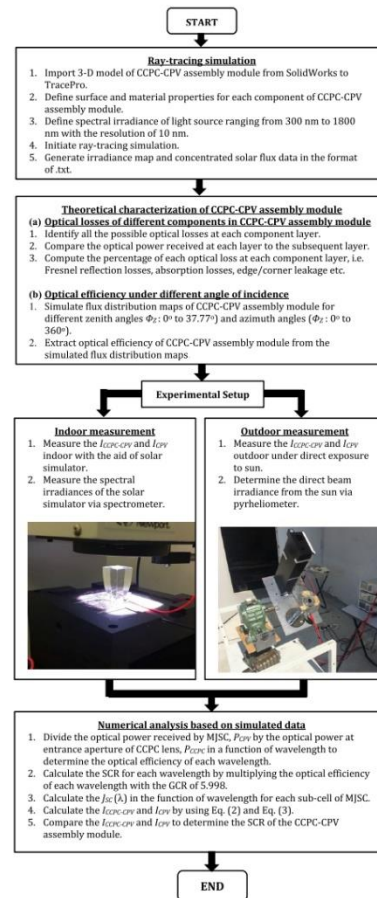


Fig. 3. Summary of the evaluation process of the CCPC-CPV assembly module.

module during operation are listed out in the theoretical modeling, which include Fresnel reflection loss, absorption loss, edge/corner leakage loss caused by the adhesive spillage, etc. The refractive indices, n , of all the elements in the CCPC-CPV assembly module are indicated in Fig. 1(b). Any discontinuity of refractive indices appearing in the interface of two materials can result in Fresnel reflection loss in which there are several elements in the CCPC-CPV assembly with significant variations in refractive indices [21]. In addition, a bilayer of antireflective

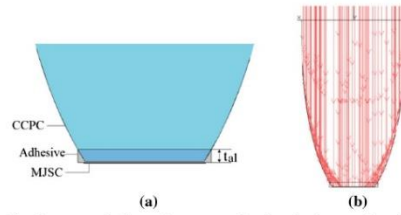


Fig. 4. Optical adhesive layer is considered in the theoretical modeling for the ray-tracing simulation: (a) a detailed view of the bottom part of the CCPC-CPV assembly module; (b) an example of ray-tracing simulation at an incident angle of 0 deg.

202 coating is applied on the top surface of the MJSC to minimize
203 the impact of the refractive index gap and hence to reduce
204 Fresnel reflection loss. The evaluation process is summarized
205 in Fig. 3. Defining appropriate values for the properties of all
206 the elements in the CCPC-CPV assembly module are critical
207 to ensure the accuracy of simulated results. Although most
208 of the material properties are available in the built-in library
209 database of TracePro, some of the information such as absorp-
210 tion coefficient α and extinction coefficient k are incomplete.
211 As a result, the properties of B270 Schott Glass were extracted
212 directly from the datasheet as provided by the manufacturer and
213 inserted into the TracePro property database [22]. The relation-
214 ship absorption coefficient α of the B270 Schott Glass versus
215 wavelength of incident light is plotted as shown in Figure 2.
216 Any wavelength before 320 nm is not able to pass through the
217 transparent material since the absorption coefficient is 1.

218 For the theoretical analyses of the CCPC-CPV assembly
219 module under real climate conditions by taking into consider-
220 ation the actual solar spectrum, the simulated light source is set
221 to have wavelengths ranging from 300 nm to 1800 nm with a
222 resolution of 10 nm in the TracePro, which corresponds to the
223 spectral response of the MJSC. The use of the full solar spectrum
224 is absolutely necessary in the ray-tracing simulation as each
225 wavelength reacts differently to different materials where the
226 refractive index varies with wavelength. To highlight the impor-
227 tance of using the full solar spectrum in the theoretical analysis,
228 a ray-tracing simulation using a single wavelength of 550 nm
229 has also been conducted for a comparison. The simulated data
230 is used to calculate the output current of the CPV cell without a
231 CCPC lens I_{CPV} and output current of CCPC-CPV assembly
232 module $I_{CCPC-CPV}$.

233 To bond the CCPC lens onto the MJSC, optical adhesive
234 with high transmittance is employed. Baig *et al.* [14] posited
235 that the encapsulated spillage surrounding the bottom side of
236 the lens can lead to light leakage from the edge of the optical
237 element in which the thickness of optical adhesive spillage
238 plays a vital role in justifying the optical losses. In the current
239 stage of this research, it is impossible to eliminate the spillage
240 of the optical adhesive completely. Hence, a layer of optical
241 adhesive is needed to be included in the ray-tracing simulation
242 as shown in Fig. 4. From Fig. 4(a), the thickness of the adhesive
243 spillage surrounding the bottom edge of CCPC lens t_{ad} is the key

244 parameter to affect the optical losses. In this simulation, the per-
245 formance of the CCPC-CPV assembly module has been tested
246 with the thickness of the optical adhesive adjusted to 1 mm,
247 2 mm, 3 mm, and 4 mm. An example of ray-tracing simulation
248 is shown in Fig. 4(b). With the light source placed normal to the
249 entrance aperture of the CCPC lens, tens of thousands of light
250 rays are traced through the total internal reflection, refraction,
251 and scattering phenomena inside the lens during the simulation.

B. Numerical Analysis

252 For the verification of the theoretical result, the spectral irra-
253 diance of the solar simulator is measured via the AVANTES
254 spectrometer during indoor measurement. The measured
255 spectral irradiance is then applied in the following numerical
256 analysis. First, the optical efficiency of each wavelength is com-
257 puted by comparing between the optical power received by the
258 CPV cell (P_{CPV}) and the optical power arrived at the entrance
259 aperture of the CCPC lens (P_{CCPC}) as shown in the following
260 equation:
261

$$\eta_{\text{optical}}(\lambda) = \frac{P_{CPV}}{P_{CCPC}} \times 100\%. \quad (1)$$

262 The optical efficiency in the function of wavelength,
263 $\eta_{\text{optical}}(\lambda)$, is then multiplied with the geometrical concen-
264 tration ratio (GCR) of the CCPC lens (5,998 suns) and divided
265 by 100% to obtain the spectral SCR, $C(\lambda)$, for each wavelength.
266 The equation of the output current of the CPV cell without
267 CCPC lens I_{CPV} has been derived in our previous work [23] and
268 can be simplified to

$$I_{CPV} = A_{\text{active}} \times \int \left(\frac{q\lambda}{hc} \right) \eta_{EQE}(\lambda) \cdot S_L(\lambda) d\lambda, \quad (2)$$

269 where A_{active} is the active area of MJSC; q represents the elec-
270 tronic charge; c stands for the speed of light in vacuum; h is the
271 Planck's constant; $\eta_{EQE}(\lambda)$ is the EQE of any $p-n$ junction
272 subcell in the MJSC, which is in a function of wavelength;
273 and $S_L(\lambda)$ is the spectral irradiance of the light source (solar
274 simulator or the Sun).

275 Based on Eq. (2), we calculate the output current for all the
276 three $p-n$ junctions of subcells in the MJSC. Since three sub-
277 cells are serial connected in the MJSC, the net output current
278 of the MJSC is capped by the lowest output current among
279 the three subcells. The following is the equation for the output
280 current of the CCPC-CPV assembly module:

$$I_{CCPC-CPV} = A_{\text{active}} \times \int C(\lambda) \cdot \left(\frac{q\lambda}{hc} \right) \eta_{EQE}(\lambda) \cdot S_L(\lambda) d\lambda. \quad (3)$$

281 The SCR of the CCPC-CPV assembly module can be deter-
282 mined through the following equation:

$$SCR = \frac{I_{CCPC-CPV}}{I_{CPV}}. \quad (4)$$

C. Experimental Setup

283 The simulation result has been validated with a series of indoor
284 and outdoor experiments. Optical adhesive has been used to
285

286 bond the CCPC lens and MJSC cell together. The surface of
 287 the MJSC has been cleaned before assembly to remove the dust.
 288 Then, an adequate amount of optical adhesive is applied on
 289 the MJSC surface, and then CCPC lens is placed on top of the
 290 optical adhesive. As the adhesive needs time to cure, the position
 291 between the CCPC lens and MJSC has been held with a jig to
 292 ensure they stay in position during curing process. An indoor
 293 experiment was conducted with the aid of Oriol's Sol1A™
 294 Class ABB solar simulator. The spectrum of the solar simula-
 295 tor was measured using the AVANTES spectrometer, and the
 296 measured spectral irradiance was then substituted into Eqs. (2)
 297 and (3) to calculate output currents for the CPV module only
 298 and the CCPC-CPV module, respectively. In this case, it can be
 299 safely assumed that both the indoor experiment and ray-tracing
 300 simulation were referred to the same spectral irradiance. The
 301 effective SCR of the CCPC-CPV assembly module can be
 302 obtained by comparing the output currents of two CPV mod-
 303 ules, in which one is with and the other is without CCPC lens.
 304 During the indoor experiment, the entrance aperture of both
 305 CPV and CCPC-CPV modules are fixed at the same height and
 306 placed in a fixed position to assure both of them receive the same
 307 amount of incident light within the same acceptance angle. The
 308 output currents are then measured using a multimeter, and the
 309 empirical results have been tabulated based on an average value
 310 of five measurements for each module.

311 The outdoor performance of the CCPC lens has been estab-
 312 lished under the actual working environment. In contrast to the
 313 laboratory test, the situation becomes more complicated for the
 314 outdoor experiment due to the variation of ambient conditions
 315 and direct exposure to the Sun. A tester box is designed for the
 316 purpose of outdoor measurement, where the design of the tester
 317 box was inspired by the working principle of the pyrheliometer
 318 to accommodate both the tracking error angle, α , of 0.1° and
 319 opening angle, β , of 2.5° as depicted in Fig. 5. It allows both
 320 CPV and CCPC-CPV modules to be exposed to the same
 321 amount of incident light by subtending to the same view angle,
 322 and the following are the relevant equations:

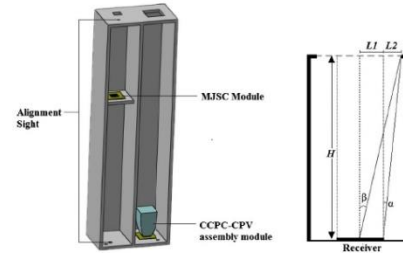
$$H = \frac{L1}{\tan \beta - \tan \alpha}, \quad (5)$$

323

$$L2 = H \tan \alpha, \quad (6)$$

324 where H represents the height between the entrance aperture
 325 of the receiver and the opening, α represents the tracking error
 326 angle, β represents the full view angle, $L1$ is the half-length of
 327 the receiver, and $L2$ is the gap distance between the opening and
 328 the edge of receiver.

329 The facing direction of the instrument was adjusted manu-
 330 ally. The holes of alignment sight were used as a reference for
 331 easy and precise optical alignment to ensure the instruments
 332 always face toward the Sun perpendicularly. The outer surface
 333 was sprayed with black coating to isolate it from the diffused
 334 light. A pyrheliometer was installed and aligned with the tester
 335 box to measure the direct beam irradiance from the Sun. With
 336 the outdoor experimental setup as illustrated in Fig. 3, the mea-
 337 surements were repeated for different days and periods of time
 338 so that more variations of data could be obtained for detailed
 339 analysis.



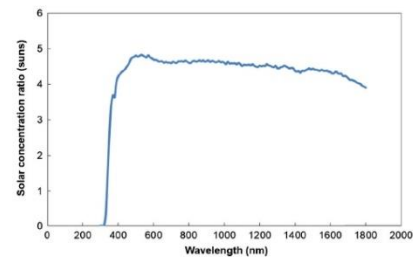
340 Fig. 5. Tester box/case is designed for outdoor measurement.
 341 (a) The illustrative 3D schematic diagram of the tester box/case.
 342 (b) The dimension of the tester box/case is designed according
 343 to Eqs. (5) and (6), and the receiver size of the MJSC module is
 344 $10 \text{ mm} \times 10 \text{ mm}$ (active area of the solar cell), while the receiver size
 345 of the CCPC-CPV assembly module is $24 \text{ mm} \times 24 \text{ mm}$ (entrance
 346 aperture of CCPC lens).

340 4. RESULTS AND DISCUSSION

341 A. Simulated Result

342 1. Comparison between Full Solar Spectrum and Single 343 Wavelength in Theoretical Modeling

344 In this paper, it is advocated that the full solar spectrum should
 345 be utilized in the theoretical modeling to emulate the actual con-
 346 dition of the solar spectral irradiance with wavelengths ranging
 347 from 300 nm to 1800 nm and the resolution of 10 nm . Based
 348 on the simulation result, the simulated SCR versus the wave-
 349 length of the light source has been plotted throughout the whole
 350 solar spectrum as depicted in Fig. 6. Starting from 300 nm , the
 351 SCR of the CCPC-CPV assembly module increases steeply
 352 upward and then remains at high SCR in the range of visible
 353 light (400 nm – 650 nm). Then, the SCR drops gradually when
 354 the wavelength of the solar spectrum further increases towards
 355 the range of the infrared region (650 nm – 1800 nm). It shows
 356 that the properties of all the materials behave differently subject
 357 to the wavelengths of the solar spectrum. From the simulation
 358 result, the peak of the SCR is 4.85 suns at the wavelength of



344 Fig. 6. Variation of solar concentration ratio for CCPC-CPV
 345 assembly module in the function of wavelength is simulated rang-
 346 ing from 300 nm to 1800 nm with a resolution of 10 nm correspond-
 347 ing to the full solar spectrum.

Table 2. Computed Short Circuit Current, I_{sc} for Each Subcell of MJSC

Subcell	Single Wavelength 550 nm		Full Solar Spectrum	
	CCPC-CPV Assembly		CCPC-CPV Assembly	
	Single Cell	Module	Single Cell	Module
InGaP	14.04 mA	67.32 mA	12.88 mA	59.66 mA
InGaAs	18.28 mA	87.63 mA	9.75 mA	45.29 mA
Ge	70.37 mA	337.41 mA	16.66 mA	75.04 mA

550 nm, and the average SCR of the full solar spectrum is 4.65 suns. Therefore, an overestimation of output power will happen if a single wavelength at 550 nm is applied in the simulation instead of the full solar spectrum.

The short circuit current I_{sc} generated from each subcell of the MJSC has been computed through Eqs. (2) and (3), and tabulated in Table 2. Since MJSC consisted of three subcells stacked in different layers connected in series, the actual output current follows the subcell with lowest current [24]. Based on Table 2, the I_{sc} will follow the current output of InGaP for the case of single wavelength, while the I_{sc} will follow the current output of InGaAs in the case of full solar spectrum.

2. Optical Behavior under Different Angles of Incidence

The optical characteristics of the CCPC-CPV module are studied under omnidirectional incident light with different angles of incidence relative the entrance aperture of the CCPC-CPV module. The angle of incidence is an important input to model CPV systems, and the Sun position relative to the CPV system can be expressed in two angular components: zenith angle and azimuth angle. From Fig. 1(b), the zenith angle Φ_Z is the angle between the Z axis and the incident ray, and azimuth angle Φ_A is the angle between the Y axis and projection of the incident ray (positive direction starting from the front view of the CPV module in the counterclockwise direction). As the half acceptance angle of the CCPC lens is 37.77° , the range of the zenith angle used in the ray-tracing simulation is between 0° and 37.77° , while the azimuth angle used in the ray-tracing simulation ranges from 0° to 360° .

From Fig. 4(b), more light rays are directed to the peripheral region as compared to that of the central region of the CPV cell when the light source is positioned perpendicularly relative to the CCPC-CPV module. It is because the light rays hitting on the dielectric-filled CCPC inner wall are totally internal reflected to the peripheral regions instead of the central region, especially the regions near to four corners. Figure 7 shows the simulated flux distribution map of concentrated sunlight on the active region of the MJSC for different incident angles in terms of zenith angle Φ_Z and azimuth angle Φ_A . The flux distribution map shifted to the left when the zenith angle increased from 0° to 20° at azimuth angle of zero, while the flux distribution map shifted diagonally to the top-left corner of the receiver when the azimuth angle increased from 15° to 45° at zenith angle of 20° . Figure 8 plots the simulated optical efficiency of the CCPC-CPV assembly module versus azimuth angle for different zenith angles 0° , 10° , 20° , 30° , 37.77° . The highest optical efficiency of 72% is obtained when light rays are at the normal incidence

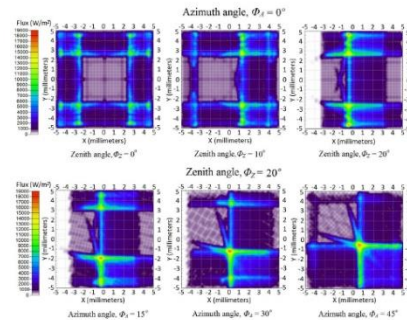


Fig. 7. Simulated flux distribution map on the MJSC receiver under different angles of incidence in terms of azimuth and zenith angles.

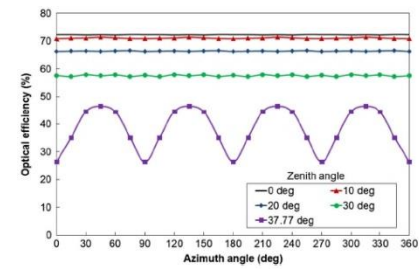


Fig. 8. Simulated optical efficiency of the CCPC-CPV assembly module versus azimuth angle for different zenith angles 0° , 10° , 20° , 30° , 37.77° .

with the angle $\Phi_Z = 0$. In 2D geometrical optics, all the light rays with incident angles less than half of the acceptance angle can be perfectly concentrated onto the active area of the MJSC. However, in 3D geometrical optics, the amount of concentrated solar flux on the MJSC receiver starts to decrease when the zenith angle increases from 10° (refer to Fig. 9) even though the zenith angle is still less than half of the acceptance angle because some skew rays may escape from the CCPC lens. The optical losses become more severe especially when the light rays with zenith angle have gone beyond 30° as they approach half of the acceptance angle. The optical efficiency drops significantly to below 0.5 after the zenith angle has reached 35° even though it is still less than the half acceptance angle of 37.77° .

The optical efficiency becomes sensitive to the variation of the azimuth angle when the zenith angle has approached 37.77° . The most optimized azimuth angles relative to the CCPC-CPV module are 45° , 135° , 225° , 315° , in which the most light rays are received by the CPV cell as compared to other azimuth angles and the rays are equally hit on two sidewalls simultaneously. It can be proven through the simulation result as

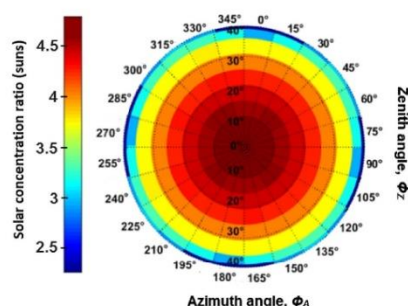


Fig. 9. Simulated distribution of solar concentration ratio for different angles of incidence: zenith angle and azimuth angle.

425 depicted in Fig. 8, where the optical efficiencies for the azimuth
 426 angles of 45°, 135°, 225°, and 315° are the highest among all
 427 azimuth angles. Figure 9 shows the overall simulated results of
 428 the distribution of SCRs for various zenith and azimuth angles.
 429 The highest SCR can be obtained when the zenith angle Φ_Z
 430 is lower than 10° and then the SCR gradually decreases as the
 431 zenith angle Φ_Z increases. Optical efficiency is not affected by
 432 the azimuth angle unless the zenith angle gets closer to the half
 433 angular acceptance angle of the CCPC lens, which is 37.77°.

434 3. Optical Efficiency Profile of CCPC-CPV Assembly Module

435 Figures 10(a) and 10(b) display a comparison of the simulated
 436 distribution profile of optical efficiency and a top view photo
 437 of the CCPC-CPV assembly module, respectively. The optical
 438 efficiency at each particular point on the entrance aperture is
 439 retrieved through the computational method and plotted as
 440 shown in Fig. 10(a). As a comparison, the actual optical losses
 441 under direct normal irradiance can also be observed with naked
 442 eyes as shown in Fig. 10(b). The blue region represents the area
 443 with the least optical power delivered to the receiver or, in other
 444 words, the region with the highest optical losses. Severe optical
 445 losses can be seen at four edges/corners of the exit aperture due
 446 to both optical adhesive spillage and skew rays, in which it can
 447 be seen as an obvious bright spot at each edge/corner of the
 448 lens.

449 Since the optical adhesive used for bonding between CCPC
 450 and CPV is unavoidable, four different thicknesses of the adhe-
 451 sive layer are modeled in the simulation to analyze the optical
 452 loss. Figure 11 shows how the thickness of the optical adhesive
 453 can affect the optical efficiency under different incident angles
 454 in which a greater thickness of the adhesive spillage can result
 455 in lower optical efficiency. For optimizing optical perform-
 456 ance, the thickness of the adhesive layer t_{a1} is fixed as 1 mm, and
 457 the thickness of the spillage surrounding the lens t_{a0} is set as
 458 0.9 mm because it is the best achievable adhesive thickness for
 459 the CCPC-CPV assembly module practically.

460 There are three major components made of different materi-
 461 als being integrated in the CCPC-CPV assembly module, which
 462 means the analysis of optical losses is complicated by requiring

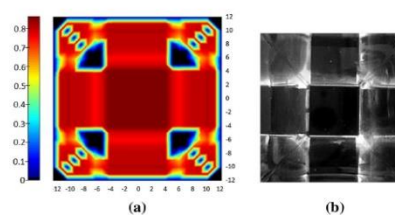


Fig. 10. Optical efficiency profile of CCPC-CPV assembly module indicates severe optical losses are incurred at the edge/corner under direct normal irradiance. (a) Computational result of 2D map optical efficiency profile. (b) Top view of actual photo taken on CCPC-CPV assembly module in which the optical efficiency profile can be observed with the naked eye.

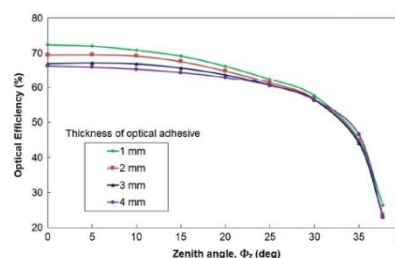


Fig. 11. Simulated optical efficiency of the CCPC-CPV assembly module versus different zenith angle Φ_Z at azimuth angle, $\Phi_A = 0$, for different thicknesses of adhesive layer t_{a1} .

463 more evidences. The optical losses of each component have
 464 been analyzed and presented in Table 3. The breakdown analysis
 465 of optical losses in each layer can be obtained by comparing
 466 the optical powers received by the corresponding layer and the
 467 subsequent layer. The Fresnel reflection losses can be predicted
 468 accurately by carefully defining the absorption coefficient α ,
 469 extinction coefficient k , and refractive index n in the function
 470 of wavelengths for each layer of the assembly. As expected,
 471 Fresnel reflection losses are one of the major optical losses in
 472 the CCPC-CPV module as the incident rays have to travel
 473 through four different mediums consecutively: air \rightarrow B270
 474 Schott glass (CCPC lens) \rightarrow optical adhesive \rightarrow MJSC. The
 475 Fresnel reflection loss I is 4.21% when light rays enter the CCPC
 476 lens. The Fresnel reflection loss II for light rays traveling from
 477 the CCPC lens to the optical adhesive is small, which is 0.52%
 478 as the refractive indices of both the CCPC lens and the optical
 479 adhesive are almost the same. Since the difference in refractive
 480 indices between optical adhesive and MJSC is relatively high,
 481 Fresnel reflection loss III for light rays traveling between the
 482 two mediums introduced a higher optical loss of 6.54%. Thus,
 483 the total Fresnel reflection loss is 11.27%. The absorption loss
 484 within the CCPC lens is obtained as 11.59% via performing
 485 ray-tracing simulation on the CCPC lens only. The absorption

Table 3. Optical Losses at Each Component Level of the CCPC-CPV Assembly Module

Type of Optical Losses	Percentage (in Term of Input)
Fresnel Loss I—air to CCPC lens	4.21%
Absorption Loss—CCPC lens	11.59%
Edge/Corner Leakage	1.48%
Optical loss caused by light escaping from optical adhesive	3.31%
Fresnel Loss II—CCPC lens to optical adhesive	0.52%
Fresnel Loss III—optical adhesive to MJSC	6.54%
Total optical losses	27.65%

loss is unavoidable in the current stage as the geometry of the CCPC lens is tailored to match with the dimension of the MJSC and substrate equipped with a bypass diode. Not much can be done on the CCPC lens to reduce the absorption loss unless we use the high transmission material, in which the cost of material will be the major concern. The absorption of optical adhesive can be neglected as the thickness is too small to affect the outcome. The percentage of each optical loss is calculated with respect to the input power entering the entrance aperture of the CCPC lens. The optical efficiency of the CCPC-CPV assembly module is 72.35% after considering the total optical losses as listed in Table 2. Since the optical efficiency of the CPV module alone (without CCPC lens) is 93.62% with only Fresnel reflection loss, the effective optical efficiency of the CCPC lens can be obtained as 77.30% via dividing the optical efficiency of the CCPC-CPV assembly module by the optical efficiency of the CPV module alone.

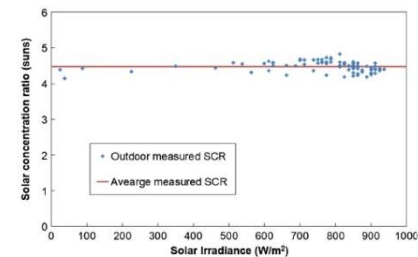
503 B. Experimental Result

504 A comparison of the outcome between the computational and
505 experimental methods is presented in Table 4. The simulated
506 SCR of 4.65 suns is determined by comparing the output
507 current of the CCPC-CPV assembly module with the output
508 current of the CPV module alone as shown in Eq. (4). The
509 resulted optical efficiency of the CCPC lens is 77.4%, which is
510 supported by the optical efficiency of 77.3% computed from the
511 breakdown analyses as in Table 2. From the indoor experiment,
512 a minor difference of 1.8% is shown between the simulated and
513 indoor measured SCRs. Overall, the effective optical efficiency
514 of the CCPC-CPV assembly module under a direct light source
515 with the full solar spectrum is 76.2%. For the case of simulation
516 based on a single wavelength, the difference between the indoor
517 measured result and simulated result is 4.8%. Once again, it
518 further consolidates our work that the ray-tracing simulation
519 utilizing the full solar spectrum can model the optical performance
520 more accurately as compared to that of single wavelength.

521
522 Furthermore, the evaluation of the CCPC-CPV assembly
523 module has taken a step forward with an outdoor measurement.
524 In this work, the outdoor experiment has been set up with
525 the consideration of the same amount of input incidence and
526 acceptance angle received by the MJSC and CCPC module
527 [17]. The results of outdoor measurement are tabulated based

Table 4. Outcome Comparison between the Simulation, Indoor, and Outdoor Experiment

	Simulated Result			
	Single Wavelength 550 nm	Full Solar Spectrum	Indoor Measured Result	Outdoor Measured Result
$I_{CCPC-CPV}$	67.32 mA	45.29 mA	43.26 mA	42.13 mA
I_{CPV}	14.04 mA	9.75 mA	9.46 mA	9.40 mA
Solar Concentration Ratio (SCR)	4.79 suns	4.65 suns	4.57 suns	4.48 suns
Optical Efficiency	79.9%	77.4%	76.2%	74.7%

**Fig. 12.** SCR of the CCPC-CPV assembly module versus solar irradiance for outdoor measurement.

528 on-site experiments for three days, where the SCR of the
529 CCPC-CPV assembly module under different solar irradiance
530 is plotted as depicted in Fig. 12. From the graph, the SCR of the
531 CCPC-CPV assembly module is found to be independent of
532 solar irradiance. The outdoor measured SCR varies in a range
533 from 4.15 to 4.83 suns with an average SCR of 4.48 suns and
534 relative standard deviation of 3.25%, which is equivalent to optical
535 efficiency of 74.7%. This variation of the outdoor measurement
536 can be caused by various external factors during on-site data
537 collection including the circumsolar effect, diffuse solar irradiance,
538 ambient temperature, humidity, weather condition, etc. From
539 Table 3, the simulated results from the theoretical modeling
540 have successfully been validated by both the indoor and outdoor
541 measurement results with deviations of between 1.8% and 3.8%
542 respectively.

543 5. CONCLUSION

544 Secondary optics have been widely deployed in CPV systems,
545 which not only can homogenize the concentrated solar flux
546 received by the solar cell but also tremendously increase the
547 SCR. In-depth understanding on secondary optics can assist
548 us in the optimization of the CPV system. To fully explore
549 this knowledge, a comprehensive analysis on the CCPC-CPV
550 module has been carried out via theoretical modeling and exper-
551 imental validation. A full range of the solar spectrum has been

552 applied in the numerical simulation of the CCPC-CPV module
 553 because the properties of each component in the CCPC-CPV
 554 module, including dielectric material, optical adhesive, and
 555 MJSC, are dependent on the wavelengths. In the theoretical
 556 modeling, a special methodology has been formulated to ana-
 557 lyze and to generate the breakdown of optical losses for each
 558 component of the CCPC-CPV assembly module. Since the half
 559 acceptance angle of the CCPC lens is designed as 37.77° based
 560 on 2D geometrical optics, 3D ray-tracing simulation has been
 561 conducted where some of light rays, especially skew rays, can
 562 escape from the CCPC lens even if the incident angle is less than
 563 37.77° . From the numerical simulation results, the effective
 564 optical efficiency of the CCPC lens has been determined as
 565 77.30% with the simulated SCR of 4.65 suns. The measured
 566 SCR under the solar simulator has been found as 4.57 suns,
 567 while the outdoor measured SCR varies in a range from 4.15
 568 to 4.83 suns with an average SCR of 4.48 suns. The simulated
 569 optical efficiency of the CCPC lens is 77.4, which is tallied with
 570 the resulted optical efficiency of 77.3% as obtained from the
 571 theoretical breakdown analysis of optical losses. Meanwhile, the
 572 outdoor measurement indicates that the CCPC-CPV assembly
 573 module can achieve an effective efficiency of 74.7% under the
 574 real working condition as the GCR of the CCPC lens is 5.998.
 575 For advanced theoretical analysis, the variations of the SCR of
 576 the CCPC-CPV module in the function of both wavelength
 577 and incident angles (zenith and azimuth angles) are also studied.
 578 Following that, the optical efficiency is also plotted in the func-
 579 tion of wavelength and incident angles. The optical efficiency
 580 is not affected by the azimuth angle unless the zenith angle gets
 581 closer to the half angular acceptance angle of the CCPC lens,
 582 which is 37.77° . In overall study, our proposed methodology
 583 with the ray-tracing technique has shown a highly reliable and
 584 promising accuracy in evaluating the assembly of secondary
 585 optics and the CPV module.

586 **Funding.** Ministry of Energy, Science, Technology,
 587 Environment and Climate Change (AAIBE Trust
 588 Fund) vote account 4356/001, UTAR Research Fund
 589 (IPSR/RMC/UTARRRF/2017-C1/W03) vote account
 590 6200/W61.

591 **Acknowledgment.** The authors would like to express
 592 their gratitude to the Ministry of Energy, Science, Technology,
 593 Environment and Climate Change and UTAR Research Fund
 594 for their financial support. Software support was provided by
 595 PD Solutions Pte Ltd.

596 **Disclosures.** The authors declare no conflicts of interest.

597 REFERENCES

- 598 1. J. Tsao, N. Lewis, and G. Crabtree, *Solar FAQs* (2006).
- 599 2. E. Kabir, P. Kumar, S. Kumar, A. A. Adelodun, and K. Kim, "Solar
 600 energy: potential and future prospects," *Renewable Sustainable
 601 Energy Rev.* **82**, 894–900 (2018).
- 602 3. M. A. Green, M. Yoshita, E. D. Dunlop, D. H. Levi, and A. W. Y. H.
 603 Baillie, "Solar cell efficiency tables (version 54)," *Prog. Photovoltaics*
 604 **27**, 565–575 (2019).

- 605 4. C. Algora and C. Rey-Stolle, *Next Generation of Photovoltaics*
 606 (Springer, 2012).
- 607 5. K. Shanks, S. Senthilrasu, and T. K. Mallick, "Optics for concentrat-
 608 ing photovoltaics: trends, limits and opportunities for materials and
 609 design," *Renewable Sustainable Energy Rev.* **60**, 394–407 (2016).
- 610 6. Y.-C. Chen, H.-W. Chiang, and W.-H. Hsieh, "Design of the secondary
 611 optical elements for concentrated photovoltaic units with Fresnel
 612 lenses," *Appl. Sci.* **5**, 770–786 (2015).
- 613 7. S. El-yahyaoui, A. Ahalouf, S. El Himer, and A. Mechaqrane, "Indoor
 614 characterization of pyramid- and cone-type secondary optics," *AIP
 615 Conf. Proc.* **2149**, 70003 (2019).
- 616 8. F. E. Sahin and M. Yilmaz, "High concentration photovoltaics (HCPV) **4**
 617 with diffractive secondary optical elements," *Photonics* (2019), Vol. **6**,
 618 p. 68.
- 619 9. F. Languy and S. Habraken, "Nonimaging achromatic shaped Fresnel
 620 lenses for ultrahigh solar concentration," *Opt. Lett.* **38**, 1730–1732
 621 (2013).
- 622 10. N. Sellami and T. K. Mallick, "Optical efficiency study of PV crossed
 623 compound parabolic concentrator," *Appl. Energy* **102**, 868–876
 624 (2013).
- 625 11. R. Winston, J. C. Minano, and P. Benitez, *Nonimaging Optics*
 626 (Elsevier, 2005).
- 627 12. C. Algora and I. Rey-Stolle, *Handbook of Concentrator Photovoltaic
 628 Technology* (Wiley, 2016).
- 629 13. N. Sellami, T. K. Mallick, and D. Mcneil, "Optical performance mod- **5**
 630 elling of an atypical 3-D cross compound parabolic photovoltaic con-
 631 centiator using ray trace technique," in *Res. Gate* (2010).
- 632 14. H. Baig, N. Sellami, and T. K. Mallick, "Trapping light escaping from
 633 the edges of the optical element in a concentrating photovoltaic sys-
 634 tem," *Energy Convers. Manage.* **90**, 238–246 (2015).
- 635 15. C. Wong, T. Yew, K. Chong, W. Tan, M. Tan, and B. Lim, "Design
 636 optimization of ultra-high concentrator photovoltaic system using
 637 two-stage non-imaging solar concentrator Design optimization of
 638 ultra-high concentrator photovoltaic system using two-stage non-
 639 imaging solar concentrator," in *IOP Conf. Ser. Earth Environ. Sci.*
 640 (2017), Vol. **93**, paper 012012.
- 641 16. T. Yew, K. Chong, and B. Lim, "Performance study of crossed com-
 642 pound parabolic concentrator as secondary optics in non-imaging
 643 dish concentrator for the application of dense-array concentrator
 644 photovoltaic system," *Sol. Energy* **120**, 296–309 (2015).
- 645 17. K. Chong, T. Yew, C. Wong, M. Tan, and W. Tan, "Dense-array con-
 646 centrator photovoltaic prototype using non-imaging dish concentra-
 647 tor and an array of cross compound parabolic concentrators," *Appl.
 648 Energy* **204**, 898–911 (2017).
- 649 18. J. C. Miñano, P. Benitez, P. Zamora, M. Buljan, R. Mohedano, and A.
 650 Santamaría, "Free-form optics for Fresnel-lens-based photovoltaic
 651 concentrators," *Opt. Express* **21**, A494–A502 (2013).
- 652 19. L. Fu, R. Leutz, and H. P. Annen, "Secondary optics for Fresnel lens
 653 solar concentrators," *Proc. SPIE* **7785**, 778509 (2010).
- 654 20. Azur Space, *Concentrator Triple Junction Solar Cell Cell Datasheet* **6**
 655 (2015).
- 656 21. I. Sankawa, T. Satake, N. Kashima, and S. Nagasawa, "Methods for
 657 reducing the fresnel reflection in an optical-fiber connector with index
 658 matching material," *Electron. Comm. Jpn. Pt. 1* **69**, 94–102 (1986).
- 659 22. S. Corp, *Specification Part A: Physical and Chemical Properties of
 660 B270 Superwhite* (1993).
- 661 23. P. S. Lee, C. W. Wong, T. K. Yew, and M. H. Tan, "Optical and elec- **7**
 662 trical performance evaluation of the crossed compound parabolic
 663 concentrator module for the application of ultra- high concentrator
 664 photovoltaic system optical and electrical performance evaluation
 665 of the crossed compound parabolic concent," in *International
 666 Conference on Sustainable Energy and Green Technology 2018*
 667 (2019), Vol. **268**.
- 668 24. G. Peharz, G. Siefert, and A. W. Bett, "A simple method for quantify-
 669 ing spectral impacts on multi-junction solar cells," *Sol. Energy* **83**,
 670 1588–1598 (2009).

Queries

1. AU: Please note that the figures must be cited in sequential order. Please provide us the correct citation order.
2. AU: The funding information for this article has been generated using the information you provided to OSA at the time of article submission. Please check it carefully. If any information needs to be corrected or added, please provide the full name of the funding organization/institution as provided in the CrossRef Open Funder Registry (<https://search.crossref.org/funding>).
3. AU: Please provide more information for Ref. [1], i.e., url.
4. AU: Is a full page range available for Ref. [8]?
5. AU: Please provide more information for Ref. [13], i.e., volume/page numbers, conference title.
6. AU: Please provide more information for Refs. [20,22], i.e., url, report number.
7. AU: Please provide a chapter/section number or page range for Ref. [23].